Two-dimensional Layered Materials-based Energy-efficient Optoelectronic Memories: A Leap Towards Bionic Vision

Aarti Dahiya[1], Parthasarathi Pal[2], Shalu Rani[1], Mohit Kumar Gautam[3], Roshni Shateesh Babu[3], Ioannis Zeimpekis[3,4,5], Dimitra G. Georgiadou[3,4,5*], and Sanjay Kumar[2*]

[1]Department of Electronics Engineering, Indian Institute of Technology (ISM) Dhanbad, Jharkhand, India.
[2]Department of Electrical Engineering, Indian Institute of Technology Patna, Bihar, India.
[3]School of Electronics and Computer Science, University of Southampton, Southampton, United Kingdom.
[4]Centre for Neuromorphic Technologies (CeNT), University of Southampton, University Road SO17 1BJ, Southampton, United Kingdom.
[5]Optoelectronics Research Centre, University of Southampton, Southampton, United Kingdom.

[*]Corresponding authors: sanjaysihag91@gmail.com (S. Kumar); D.Georgiadou@soton.ac.uk (D. G. Georgiadou)

Abstract: Optoelectronic memories have gained remarkable attention owing to their inherent capability of manipulating charge carriers under the influence of both electrical and light stimuli. The emerging optoelectronic neuromorphic devices can be used in diverse applications, including logical data processing, confidential information recording, and next-generation bionic visual systems. Photosensitive materials are foundational to many technologies, including solar cells, sensors, thin-film transistors, and light-emitting diodes. Recently, two-dimensional (2D) photosensitive materials have found application in bionic visual hardware based on optoelectronic synaptic memristor and memtransistor devices. The synthesis and growth of optoelectronic memories driven by 2D photosensitive materials have opened new horizons in the field of bionic visual systems due to their diverse optical properties, atomic scalability, and ultrafast charge carrier dynamics. This review highlights the recent developments in bionic visual hardware based on optoelectronic synaptic memristive devices and memtransistors, wherein various 2D photosensitive materials and device structures have been utilised. We first summarise the limitations of traditional computing, highlight the key advantages of this novel computing paradigm, and discuss the fundamentals of bio-vision formation. Next, we comprehensively review the various device structures and operating mechanisms of optoelectronic memristive and memtransistor architectures. The recent developments in optoelectronic synaptic devices by incorporating various 2D photosensitive materials and their application in the field of bionic visual perception are also discussed. Finally, we outline the current drawbacks and challenges of optoelectronic neuromorphic devices and the future perspective of bionic visual hardware on real system realisation.

***Keywords*:** 2D Materials; Energy-efficient, Optoelectronic memories; memristor; memtransistor; Neuromorphic computation; bionic visual hardware

Introduction

The traditional von Neumann architecture consists of the central processing unit (CPU), memory, and input/output (I/O) subsystem to execute a series of instructions [1]. Therefore, data needs to be extracted from the memory and transferred to the processing unit for computation. After computation, the result needs to be transferred back to the memory via supporting circuitry. Due to this two-way transfer process, the energy consumption and processing time of the system significantly increase, and the data transfer efficiency is limited. This is known as the von Neumann bottleneck [2]. In addition, Moore's law is expected to reach its limits in the next few years. Scaling down the chip size toward the atomic dimensions poses limitations to the physical operation of the devices [3]. In the biological brain, neurons and synapses are co-located within the same highly interconnected neural network, wherein each neuron is connected to approximately 10^4 other neurons. Such architecture offers data processing and memory functionality through synaptic excitation and neuron firing, which share the same location within the brain, leading to low power consumption [4]. Therefore, brain-inspired or widely known as neuromorphic computing is expected to surpass the current technical bottleneck and can deal with large-scale data processing [3,5].

Traditional memory devices and complementary metal-oxide-semiconductor (CMOS) processes have dominated computing. However, their high computational demands hinder implementation in dynamic, learning-driven tasks [6]. Neuromorphic computing holds great potential to surpass the limitations of traditional von Neumann computing in terms of speed and energy efficiency [7-8]. This emerging computing technology facilitates local data storage and parallel computing, unlocking its potential for diverse applications, such as robotics, cybersecurity, autonomous vehicles, pattern recognition in healthcare, and edge artificial intelligence (AI) computing [9].

Neuromorphic computing aims to emulate the connectivity of the brain, where the communication between two neurons is dependent on the strength of their synapses, and they are further linked to other neurons, forming in this way a neural network for volumetric conversation. The volumetric conversation of the synapse is not static. The ability to change synaptic weight is termed synaptic plasticity, which is a key mechanism pursued by the biological brain during learning and forgetting processes [10]. The synaptic weight can be weakened or strengthened, processes termed as depression and potentiation, respectively [11]. Depending on whether these changes in synaptic strength are temporary or more permanent, short-term synaptic plasticity and long-term synaptic plasticity are defined [12].

Memristors are two-terminal devices able to realise such characteristics, wherein the resistance changes (equivalent to synaptic weight) correspond to the electrical current passing through them. In

1971, Prof. Leon Chua was the first to propose the theoretical concept of the memristive device having memory characteristics wherein the working states are accountable to the operation history [13]. It took over 35 years for the first memristor to be experimentally realised in 2008 by Strukov *et al.* [14] in HP labs by implementing a sandwich structure of $Pt/TiO_{2-x}/Pt$. In memristive devices, the conductive filament (CF) formation occurs when an externally applied electric field drives ions (e.g., oxygen vacancies or metal cations) to migrate through the insulating (or switching) layer. These ions accumulate and create a localised CF between the electrodes, switching the device from high resistance (HRS) to low resistance (LRS) and vice versa under dissolution of the CF. Currently, the memristor represents a tractable candidate for memory and neuromorphic computing, yet cycle-to-cycle (C2C) and device-to-device (D2D) variability hinders its wider adoption in the CMOS industry [15]. Recent studies suggested that the root of C2C variability is attributed to the change in the distance between the electrode and the tip of the broken conductive filament (CF) during the reset process [16]. For large-area devices, the stochasticity of CF formation through percolation processes increases with the number of cycles, which is associated with various shapes, sizes, and quantities of CFs [16]. In addition, sneak current is inevitable for large matrix sizes, which can be avoided by using a selector, such as transistors or diodes [17]. To overcome these challenges, research efforts have focused on designing gate-tunable memristors that seamlessly integrate the properties of memristors and transistors, known as memtransistors [18]. Memtransistors, namely three-terminal devices endowed with characteristics of memristors comprising an inherent selector (in this case a transistor), have emerged as potential candidates for neuromorphic computing systems.

In the context of material space, numerous materials, such as carbon nanotubes, organics, metal oxides, halide perovskites, 2D, and ferroelectric materials, have been extensively explored for memristive and memtransistor devices [19-23]. Among them, 2D layered materials have gained much attention due to their unique physical and chemical properties, viz. quantum confinement effects, direct band gap with energies spanning from visible to infra-red part of the spectrum, strong light-matter interaction, strong excitonic effect, high carrier mobility, and strong spin-orbit coupling, and have been successfully employed in energy-efficient memristive devices [24-26]. The layered structure and inherent defects permit the memristor device fabrication with a thin switching layer that confines the stochastic processes occurring during switching [15-16]. Moreover, the photosensitivity of 2D materials offers significant potential to fabricate bionic visual perception devices that efficiently mimic the functionalities of the human retina cells [27].

The visual perception system is pivotal for capturing and learning information from the peripheral environment [10]. Therefore, replicating a visual perception system with retina-like devices with

efficient signal processing is a promising direction to design an artificial vision system [28-32]. Recently, 2D transition metal dichalcogenide (TMDCs)-based logic circuits have been successfully developed as an artificial vision unit to emulate crucial retinal functions, realizing the fundamental processes of visual perception [33]. These circuits unveil the potential to convert continuous light signals into electrical signals, which are transmitted to the optical nerve system for further processing [33]. Furthermore, memristive and memtransistor devices successfully emulate retina-like features and hold remarkable potential in neuromorphic functions, such as memory, learning, and pattern recognition in artificial intelligence applications [34-37].

The main objective of this comprehensive review is centred on the various 2D materials-based memristive and memtransistor devices for developing advanced memory device technologies and visual bionic applications. The review article commences with the introduction of the basic principle of biological vision. It is followed by a brief introduction to neural behaviour terminologies, such as short-term and long-term plasticity (STP and LTP), paired-pulse facilitation (PPF) and paired-pulse depression (PPD), and spike-timing-dependent plasticity (STDP). A summary of the artificial synapses is discussed in the upcoming section. The next section delves into different device structures and the working mechanism of 2D material-based memristive devices, along with their prospects and hurdles. The latter section deals with the advancement in the field of 2D materials-based memtransistor devices. Lastly, the potential of 2D photosensitive materials to facilitate and support the widespread adoption of bionic vision applications, along with the key challenges and future direction in this area, is being discussed. A timeline of the main developments in 2D materials-based optoelectronic memristive and memtransistor devices [38-57] is shown in **Fig. 1.**

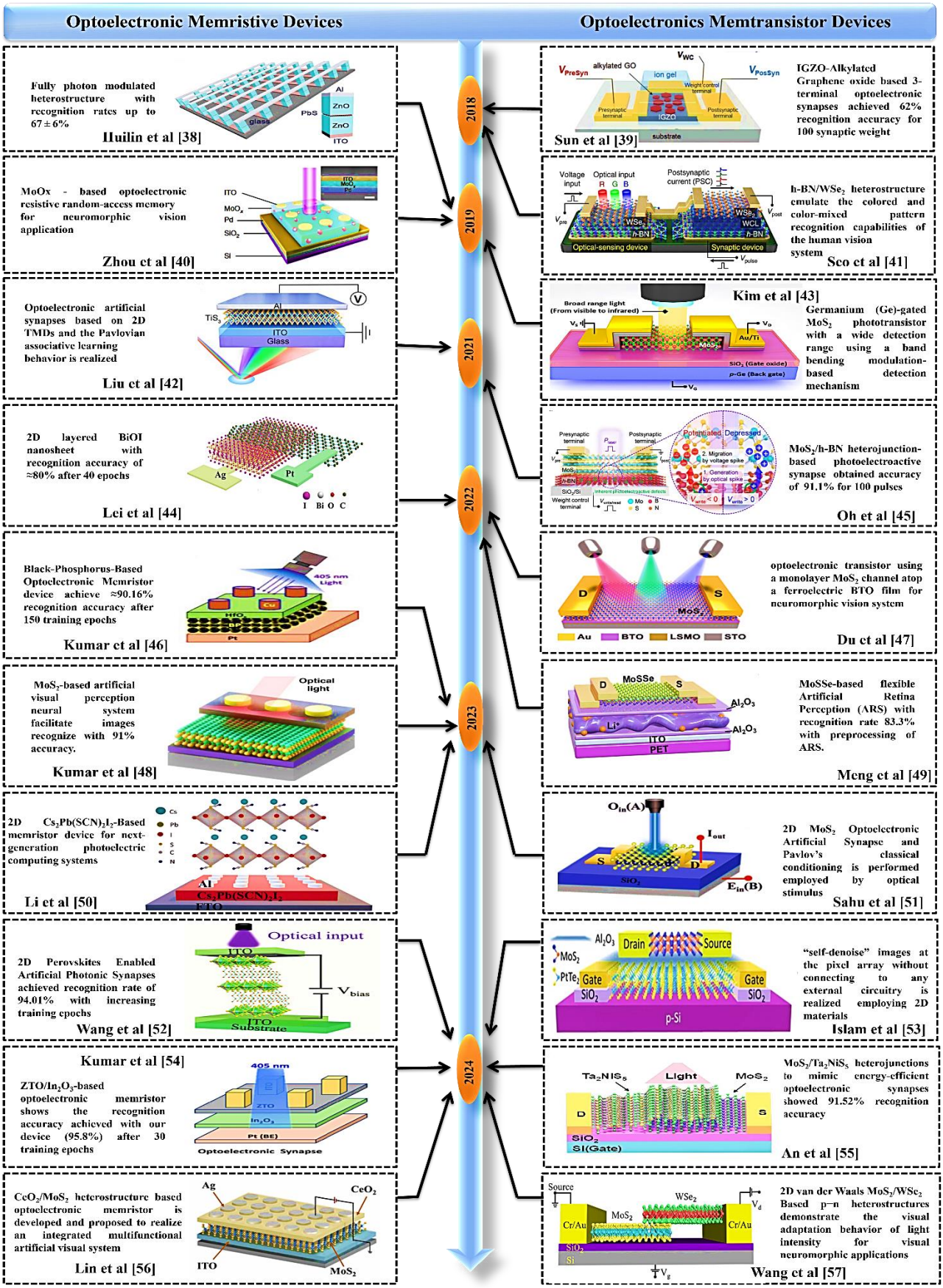

Fig. 1: A timeline of the development of 2D materials-based optoelectronic memristive and memtransistor devices [38-57]. Reproduced or adapted with permission from Ref. [38] Copyright [2019] [Elsevier], Reproduced or adapted with

permission from Ref. [39] Copyright [2018] [Wiley], Reproduced or adapted with permission from Ref. [40] Copyright [2019] [Springer Nature], Reprinted with permission under a Creative Commons CC-BY license from Ref. [41] Copyright [2018] [Springer Nature], Reproduced or adapted with permission from Ref. [42] Copyright [2021] [American Chemical Society], Reproduced or adapted with permission from Ref. [43] Copyright [2019] [American Chemical Society], Reproduced or adapted with permission from Ref. [44] Copyright [2022] [Wiley], Reprinted with permission under a Creative Commons CC-BY license from Ref. [45] Copyright [2021] [Springer Nature], Reprinted with permission under a Creative Commons CC-BY license from Ref. [46] Copyright [2023] [Wiley], Reproduced or adapted with permission from Ref. [47] Copyright [2022] [Elsevier], Reprinted with permission under a Creative Commons CC-BY license from Ref. [48] Copyright [2023] [Springer Nature], Reproduced or adapted with permission from Ref. [49] Copyright [2022 [American Chemical Society], Reproduced or adapted with permission from Ref. [50] Copyright [2023] [Elsevier], Reproduced or adapted with permission from Ref. [51] Copyright [2023] [Wiley], Reprinted with permission under a Creative Commons CC-BY license from Ref. [52] Copyright [2024] [Wiley], Reprinted with permission under a Creative Commons CC-BY license from Ref. [53] Copyright [2021] [Springer Nature], Reprinted with permission under a Creative Commons CC-BY-NC license from Ref. [54] Copyright [2024] [Elsevier], Reproduced or adapted with permission from Ref. [55] Copyright [2024] [Wiley], Reproduced or adapted with permission from Ref. [56] Copyright [2024] [Elsevier], Reproduced or adapted with permission from Ref. [57] Copyright [2024] [American Chemical Society].

Principles of Biological Vision

The light absorption processes in the human eye are vital to understand the working mechanism of the bionic eye. The light travels through the cornea, iris, and lens, which allows the light to focus on the photosensitive retina. Retinal cells contain photoreceptors, namely, rods and cones, that convert light into electrical nerve signals via photochemical reactions, stimulating the retinal ganglion cells [58]. The eye comprises 120 million rods, which are sensitive to dim light, and 6 million cones that promote colour vision in bright light [59-60]. The schematic representation of the biological vision concept is shown in **Fig. 2**.

The visual system consists of synapses and neural connections that, as a whole, form a neural network. The biological vision system mainly works in two counterparts that are connected through the optic nerve [61]. First, the information is received and pre-processed by the retina. The cone and rod cells, which are also known as photoreceptor neurons in the retina, convert incident light signals into neuroelectrical signals, and these pre-processed signals are further transmitted through the optic nerve to the brain [62-63]. Finally, these signals are processed by the visual centres of the cerebral cortex to perform the recognition and memory functionalities. This is a complete visualisation of an image that one can see in the outside environment. In a nutshell, the information transmission in the visual formation process is executed by the rapid release and reception of neurotransmitters in the synapses, which facilitate real-time imaging of the brain from the outside world.

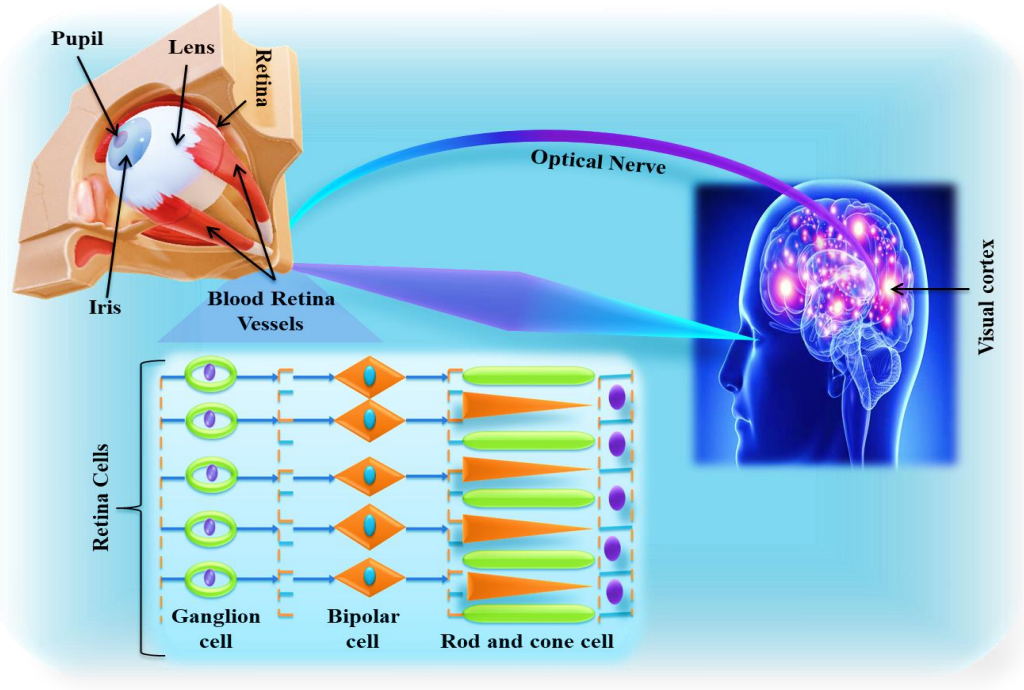

Fig. 2: Schematic representation of the principle of biological vision.

Working Principles of Neural Functions

The electrical signal, known as an action potential, propagates between two neurons. It is initially generated by the presynaptic neuron and travels down the axon to the presynaptic membrane, which releases neurotransmitters. These neurotransmitters recognise and bind to ionotropic receptors, causing either excitatory or inhibitory changes in the postsynaptic membrane potential. When the potential in the post-synaptic neuron exceeds a certain threshold, an action potential is generated by the post-synaptic neuron. The generated action potential activates excitatory/inhibitory post-synaptic currents (EPSC/IPSC), which enable the complete signal processing between the two neurons [64-72]. Neural plasticity refers to the ability to change the properties of synapses, which contributes to the learning and memory function in the biological brain. Neural plasticity includes synaptic plasticity and non-synaptic plasticity [73-74]. The non-synaptic plasticity defines changes in the intrinsic excitability of a neuron, wherein synaptic connections are not involved. It can arise from modifications in the neuron's ion channel activity, membrane properties, or excitability thresholds, and regulates how easily the neuron fires action potentials, independent of synaptic strength.

The Hebbian learning rules [75] describe the change in the synaptic weight or strength of synaptic connections between two interconnected neurons when the firing of action potentials occurs in a synchronised manner. The efficiency of the information transmission between two neurons is a function of synaptic plasticity [76]. Based on the length of retaining a memory, synaptic plasticity can

be classified into two types, namely: short-term and long-term plasticity [77-78]. The short-term plasticity often lasts for only a few seconds to minutes after stimulation, followed by a gradual return to the initial state. The synaptic weight change comprises short-term potentiation (STP) and short-term depression (STD) [79]. The STP/D has two important synaptic functions, namely: paired-pulse facilitation (PPF) and paired-pulse depression (PPD). When the two consecutive action potentials act on the synapses, the second potential generates a stronger response than the prior potential; this phenomenon is known as PPF, and the opposite is known as PPD [80]. The long-term plasticity is another synaptic plasticity that is meticulously associated with biological learning and memory functions, wherein the synaptic weight can be maintained for several hours to a week or even longer after stimulation, and it can also be divided into long-term potentiation (LTP) and long-term depression (LTD) [81]. The LTP and LTD correspond to the persistent augmentation and decrement in synaptic strength. STP can be converted into LTP under certain conditions, including high-frequency stimulation, duration, and repetition of stimulation, and controlled ionic motion. Additionally, many other forms of synaptic behaviours, including spike-timing-dependent plasticity (STDP), spike-rate-dependent plasticity (SRDP), supervised and unsupervised learning, and associative learning, are also crucial for information processing [81]. Inspired by the biological visual system, optoelectronic memristive devices mimicking these synaptic functions are utilised to develop artificial visual systems with neuromorphic computing abilities.

Artificial Synapses

The biological synapses are the basic building blocks of neural networks to achieve information transmission and memory functions. The attempt to emulate the function of biological synapses has given rise to the development of new electronic device concepts. The artificial synapses utilise the change in the conductance or resistance akin to synaptic weight change. Over the last decade, various materials (e.g., resistive, magnetic, phase change, and ferroelectric materials) and device structures (e.g., two-terminal memristive devices and three-terminal memtransistors) have been explored, which offered new insights into the development of artificial synapses [78-80]. Memristive devices were the first devices to realise artificial synapses, wherein the resistance changes correspond to the amount of electrical current passing through the device. It can switch between two distinct states, with long retention of each state, showing non-volatile behaviour. These characteristics of memristive devices are used to achieve synaptic plasticity by applying specific electrical stimuli.

After Chua [13] introduced the theoretical concept of the memristor in 1971, in the early 2000s, Hasegawa *et al* [82] and Terabe *et al* [83] demonstrated a two-terminal atomic switch, in which a solid-state electrochemical reaction occurred to regulate the formation and rupture of metallic atom bridges

positioned between two electrodes. Interestingly, the conductance is dictated by the history of input stimuli and exhibits two distinct conducting states, mimicking synaptic weight update in biological synaptic memory function. In these fabricated devices, a spontaneous decline of conductance was observed after a weak input signal, similar to short-term plasticity, was applied, followed by another long stable conductance state, resembling long-term plasticity. In 2003, Sakamoto *et al*. [84] proposed a nanoscale switch, in which a copper sulfide semiconductor (Cu_2S) was sandwiched between copper film and a top electrode consisting of Au/Pt/Ti. The conducting path between the electrodes was formed and disrupted under the application of the positive and negative voltages to the Au/Pt/Ti electrode, respectively. The generated conductance changes due to this repeated switching exhibit memory characteristics.

The first 'memristor' word was realized in 2008 by Stanley Williams *et al.,* who experimentally designed a device by implementing a sandwich structure of $Pt/TiO_{2-x}/Pt$ [14]. A memristor is a two-terminal device structure similar to a capacitor. The electrodes of the memristor can be mapped to pre-synaptic neurons and post-synaptic neurons. The electrical pulse stimuli are applied to memristors to generate the signal of pre-synaptic neurons. The synaptic weight can be represented as the conductive state, which can be modulated by varying the amplitude, pulse duration, and frequency. Furthermore, optical stimuli or combined electrical-optical stimuli are used to update the conductive state, which are known as optoelectronic memristive devices. Two-terminal memristive devices, are closely resemble biological synapses, are the most common configuration, but three-terminal memtransistor configurations are also adopted to emulate the synaptic functionality [64]. In the following section, various 2D material-based memristive and memtransistor devices for bio-vision applications are discussed.

2D Materials

2D layered materials belong to a family of materials in which atoms form the chemical structure are held together by strong in-plane chemical bonds and relatively weak out-of-plane van der Waals (vdW) interactions [85]. The rapid advancement in 2D materials synthesis techniques has gained considerable attention in micro/nanoelectronic devices and emerged as a versatile platform in the field of memory devices. Atomically thin layered films offer a substantial advantage for scalability, enabling high-density integration in memory devices [86]. Due to the atomic-level thickness, the quantum confinement comes into existence along the out-of-plane direction, resulting in excellent optical and electronic properties [87-88]. A monolayer of 2D materials can be obtained by mechanical exfoliation from their bulk, resulting in a naturally passivated film without dangling bonds, leading to low power consumption in memristive devices [89-90]. The atomic thickness of 2D materials permits the precise

gate voltage control and limits the short channel effect in the memtransistor devices [91-93]. The ability to stack different 2D materials in van der Waals heterostructures limits the challenges associated with lattice matching and fabrication constraints [94-95]. Furthermore, the CMOS compatibility allows the straightforward synthesis and integration of 2D materials onto diverse substrates [87]. Each 2D material owns distinguished optical and electrical properties which are functions of its crystal structure, chemical composition, and thickness [87].

The two-dimensional (2D) van der Waals (vdW) layered materials, including graphene oxide (GO), black phosphorus (BP), and transition metal dichalcogenides (TMDCs), have recently garnered significant attention in neuromorphic computing [96-99]. Among these, graphene oxide is an emerging material with exceptional potential for device downscaling and excellent compatibility with silicon technology, owing to its atomically thin structure and weak vdW interactions between layers [100-101]. Moreover, the bandgap of GO can be effectively tuned by modifying the surface functional groups, enabling better control over its electrical properties [102]. As a result, GO-based devices can emulate various synaptic functionalities, such as EPSC, PPF, STP, LTP, and STDP, thereby opening new avenues in neuromorphic computing [103-105]. Similarly, black phosphorus (BP) exhibits a direct bandgap, a broad light absorption range, and high carrier mobility, making it a promising candidate for optoelectronic memristors and neuromorphic computing applications [106]. Transition metal dichalcogenides (TMDCs), generally represented by the formula MX_2, consist of a transition metal (M) from groups IV to VIII and a chalcogen atom (X = S, Se, or Te) [107-109].

Common transition metals include those from groups IVB (titanium (Ti), zirconium (Zr), hafnium (Hf)), VB (vanadium (V) niobium (Nb), tantalum (Ta)), VIB (molybdenum (Mo), tungsten (W)), VIIB (technetium (Tc), rhenium (Re)), and VIIIB (palladium (Pd), platinum (Pt)) [110] are also have great potential in the neuromorphic computing. The 2D materials have a diverse bandgap from ~0 eV to ~5.6 eV, corresponding to graphene and h-BN, respectively. Therefore, the 2D materials have a large operating wavelength ranging from ultraviolet to far infrared wavelength [111]. Owing to their unique electronic and optical properties, 2D TMDCs hold great promise for the fabrication of bionic visual perception devices that efficiently mimic the functionalities of human retinal cells [112-114]. Moreover, TMDCs-based logic circuits have been successfully developed as a vision unit to emulate crucial retinal functions, realizing the fundamental processes of visual perception. These circuits unveil the potential to convert continuous light signals into electrical signals, which are transmitted to the optical nerve system for further processing [115]. In the memristive devices, a 2D materials-based functional layer is sandwiched between the two conductive electrodes, and the resistance of this functional layer is switched between high resistive states (HRS) to low resistive states (LRS) and vice

versa, which can be achieved by various working mechanisms, including trapping effects, ion-vacancy migration, phase change, and ferroelectric polarisation [116-119].

In the 2D optoelectronic memristors, mainly two switching mechanisms have been proposed. The first is associated with the valence change mechanism (VCM), wherein light generates charge carriers that change the oxidation state of the dielectric material, leading to a change in the resistance states [40]. The second is associated with the electrochemical metallization (ECM) mechanism, in which active materials (Ag, Cu) are used as metal electrodes [43, 45, 47]. The ECM mechanism is dominated by the migration of metal ions inside the switching layer under the optical stimuli, which leads to the formation and rupture of a conductive filament. The switching behaviour strongly depends on the material properties, electrode type, and device structure. In summary, understanding how the optical stimuli interact with 2D materials is crucial for designing efficient 2D optoelectronic memristors for neuromorphic and bionic vision applications. In the following section, the details description of various 2D materials incorporated in the visual perception is demonstrated, and their working mechanism and observed characteristics are discussed in detail.

2D Material-based Memristive Devices

The core idea is to develop optogenetics-inspired optoelectronic synapses, which employ synergistic electrical and optical stimulation to alter the initial conductivity and induce neuromorphic computing capabilities [118]. Zhou *et al* [120] developed a WS_2-doped silk fibroin (SF)-based negative photoelectric memristor that exhibits self-adaptive resistance under optical stimulation, enabling the integration of sensing, computing, and control functions. **Fig. 3(a)** shows a schematic of the human visual system (top) and the Ag/SF@WS_2/ITO memristive device (bottom). The SF is a biologically derived material that exhibits photosensitivity in the ultraviolet range. To further extend the photoresponsivity into the visible range, WS_2 is used as a dopant [121-122]. The device demonstrates bipolar switching behavior under light intensities of 0, 4.6, 6.0, and 12.7 W/m², as shown in **Fig. 3(b)**. Additionally, it successfully emulated the STP and STD under both dark and illuminated conditions (Wavelength = 620 nm), as shown in **Fig. 3(c-d)**. Zhou *et al* [120] also explored the automatic braking system with the fabricated devices in which vehicle running and braking are controlled by a red traffic light. The animation of this process is illustrated in **Fig. 3(e)**. The integrated system consists of a memristor, microcontroller unit (MCU), resistor, capacitor, and motor, as illustrated in **Fig. 3(f)**. The MCU performs analog-to-digital signal conversion and manages power. The SF@WS_2 memristor modulates its resistance upon sensing red light, thereby adjusting the overall circuit resistance. The capacitor suppresses motor-induced voltage spikes for smoother control, while the motor regulates the car's motion based on MCU output signals. The running and braking behavior under a red light is

shown in **Fig. 3(g)**. Initially, the car is in motion **(Fig. 3(g(i)))**. Upon exposure to red light, the car slows and stops within 3.9 s **(Fig. 3(g(ii)))**. Once the light is removed, the car restarts within 4.0 s **(Fig. 3(g(iii)))**. However, in this developed system, the response time of the memristive device is a critical factor that needs to be improved further. Additionally, multiwavelength response can also be a positive factor to enhance the overall adaptability of the developed system.

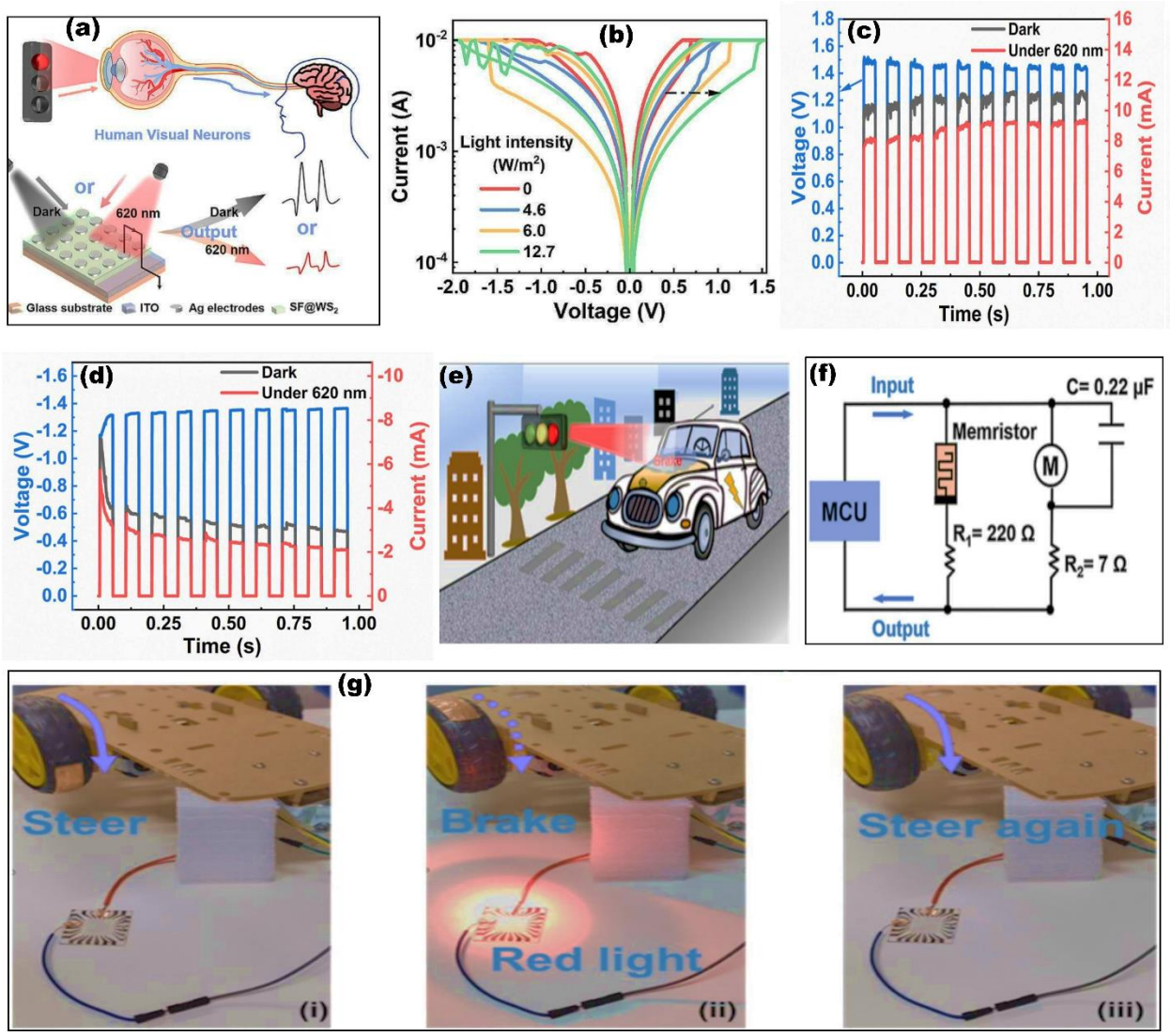

Fig. 3: (a) A schematic illustration of the Ag/SF@WS_2/ITO memristive device and the visual system, (b) Switching characteristic under the optical stimuli with the light intensity of 0, 4.6, 6.0, and 12.7 W/m^2. Stimulation under combined optical and electrical stimuli to measure (c) STP, (d) STD, (e) the animation of SF@WS_2 memristor-based autobrake system, (f) Schematic representation of circuit diagram used in the autobrake system using memristor, and (g) The running and braking processes of the car under red light. Reproduced or adapted with permission from Ref. [120] Copyright [2025] [Elsevier].

Fig. 4(a) shows the typical illustration of the biological neuron system in the human brain (left) and artificial vdw optoelectronic synapses (right), which describe the response of biological neuronal cells to optical stimuli. The optical stimulation triggered the Ca^{2+} and Na^{2+} ion channels, enabling better control over ion influx through the membrane channel. Similarly, the optogenetic-inspired artificial

synapses can be applied to modulate synaptic plasticity using optical stimuli. Many artificial optoelectronic synaptic devices operate on the persistent photoconductivity (PPC) effect, wherein light-induced conductivity persists for a long time even after removing the light stimulus [123-124]. Two strategies are proposed to introduce this PPC effect. The first strategy employs a heterojunction comprising wide/narrow bandgap materials that accumulate the photoinduced electrons or holes at the interface and induce a potential barrier across the interface due to the band bending [124]. The incident light signal is responsible for the increment of photo carriers, which change the potential distribution across the interface, enabling control over channel conductivity. The second strategy utilises the inherently photosensitive nature of the 2D material by trapping the photoexcited electron at a defect state, which promotes a strong electron-phonon coupling and impedes the capture of photocarrier. These large lattice relaxation (LLR) effects facilitate the emulation of the synaptic weight without forming complex heterojunction structures [125-127].

Seo *et al*. [127] developed optoelectronic synapses based on 2D vdW layered rhenium disulfide (ReS_2), which exhibit intrinsic photosensitivity and memory characteristics resulting from the PPC effect. The structural comparison of biological synapses with artificial vdW optoelectronic synaptic devices is shown in **Fig. 4(b)**. In addition, ReS_2 has weak interlayer coupling energy (0.19 meV $atom^{-1}$) [128-129], providing a dangling bond-free surface of 2D vdW layered materials. The DFT calculations revealed that the high PPC in ReS_2 can be attributed to the large lattice relaxation (LLR) model, which originates from the distinctive atomic structure of ReS_2. As seen in **Fig. 4(c)**, it is clear that ReS_2 crystallises in a distorted phase, forming a ribbon-like zigzag structure of Re atoms due to Peierls distortion. Furthermore, the formation energy is also calculated for rhenium (Re) and sulfur (S) vacancy defects in S-rich and S-poor films, and the findings are consistent with the X-ray Photoelectron Spectroscopy (XPS) results. As shown in **Fig. 4(d)**, the results revealed that the S vacancy has a low formation energy of 1.20 eV for S-poor and 2.05 eV for S-rich conditions. In addition, the DOS calculations of the Vs_1 ReS_2 model showed shallow bonding and antibonding states, and the latter are presented within the conduction band minimum (CBM). Hence, the shallow donor state corresponding to Vs_1 is the reason behind the existence of PPC in the ReS_2. Next, the density of states (DOS) is calculated after upgrading one electron from the filled bonding state to the empty antibonding state, as shown in the bottom panel of **Fig. 4(e)**. Upon excitation, the defect level existing above the CBM falls into the gap, resulting in the LLR model for PPC.

The photosensitive synaptic dynamics were also investigated for this device, and a significant 117% increase in conductance (ΔG) is observed when an optical spike having an energy of 1.89 eV, amplitude of 5 mW cm^{-2}, and duration of 50 ms was applied, demonstrating EPSC characteristics (see

Fig. 4(f)). For PPF, two consecutive optical spikes were applied to the ReS_2 photosensitive layer with a time interval Δt. The device exhibited Δt-dependent facilitation behavior, analogous to biological synapses. As shown in **Fig. 4(g)**, the PPF ratio is reduced from 132% to 112% as the Δt increases from 5 s to 30 s. Furthermore, the realisation of the ReS_2 vdW optoelectronic synapse device in the hardware neural network (HW-NNs) via training and inference tasks concerning the Canadian Institute for Advanced Research-10 (CIFAR-10) dataset is investigated.

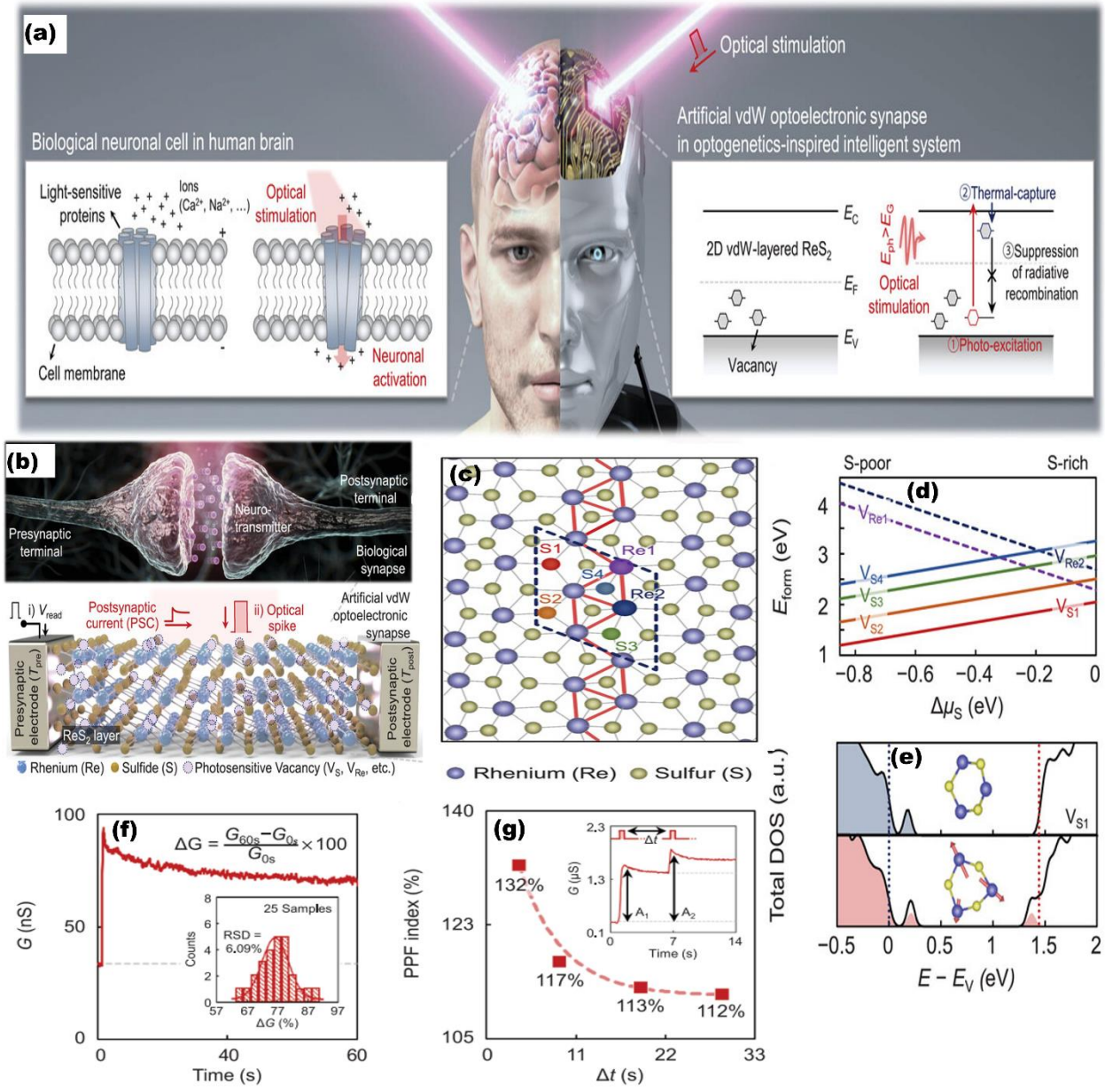

Fig. 4. Optogenetics-inspired vdW optoelectronic synapses: (a) Illustration of biological neurons in the human brain (left) and artificial vdw optoelectronic synapses (right) describing the response of biological neuronal cells to optical stimuli. (b) Structural comparison of a biological synapse with an artificial vdW optoelectronic synapse device. (c) Top view of distorted 1T phase of ReS_2 along with vacancy position used in DFT calculation. (d) Defect formation energies as a function of Sulfur (S) chemical potential (μs). (e) DOS of Vs_1 before and after promoting one electron from the filled bonding to the unfilled antibonding states. The shaded part depicts the electron positioning, and the inset displays the atomic structure. (f) Post-synaptic conductance upon applying an optical pulse of 5 mW cm^{-2} with 50 ms duration. The inset shows the

conductance distribution for the 25 vdW optoelectronic synapse devices. (g) The PPF as a function of pulse interval (Δt) showing STP characteristics. Reproduced or adapted with permission from Ref. [127] Copyright [2021] [Wiley].

Fig. 5(a) depicts the working mechanism of the vdW optoelectronic synapse device with optically and electrically weighted update (top) and electrically modulated weight update/reading. As shown in **Fig. 5(b)**, the synaptic weight is potentiated by applying the electrical spike to the pre-synaptic electrode and the optical pulse to the active layer simultaneously. Upon applying an electrical spike of -5 V or +5 V, the conductance is depressed up to -7.2% or persists +0.3%, suggesting the refreshing and reading dynamics, respectively. Furthermore, the ΔG_{read} was observed to increase from 0.07 to 0.85%, while the $\Delta G_{refresh}$ showed a decrease from -3.41 to -15.5% as a function of the amplitude of the electrical spike. The LTP characteristics for 200 cycles (see **Fig. 5(c-d)**) showed the weight updating and refreshing dynamics. Lastly, the practicability of the vdW optoelectronic synapse device for the HW-NNs using CIFAR-10 dataset recognition tasks is demonstrated. **Fig. 5(e)** shows the CIFAR-10 dataset with 8 8-layered convolutional neural networks (CNNs) consisting of vdW optoelectronic synapse devices designed via the DNN+NeuroSim integrated benchmarking framework. The HW-NN structure composed of vdW optoelectronic synapse devices is shown in **Fig. 5(f)**. The conductance associated with the recognition task is explained by the difference between the conductance states of two equivalent vdW optoelectronic synaptic devices ($G_T = G_P - G_D$). The circuit diagram of HW-NN and optical microscope (OM) image of vdW optoelectronic synapse depicts an increase and decrease in conductance comprising G_P and G_D as shown in **Fig. 5(g)**. From **Fig. 5(h)**, the results confirm a recognition rate of 89.4 %, 89.2 %, and 89.3 % under flat conditions, after bending, and flat conditions after bending 1,000 times, respectively. These findings suggest that the flexible vdW optoelectronic synapse-based neural network can operate reliably in a mechanically challenging environment and support remote training by optical stimulation. Although this work showed remarkable synaptic behaviour, several challenges need to be addressed. The endurance for only 200 LTP cycles is insufficient for practical neuromorphic applications. Furthermore, the device exhibits flexibility with tolerance up to 1000 bending cycles; this durability remains limited compared to the requirements for commercial flexible electronics.

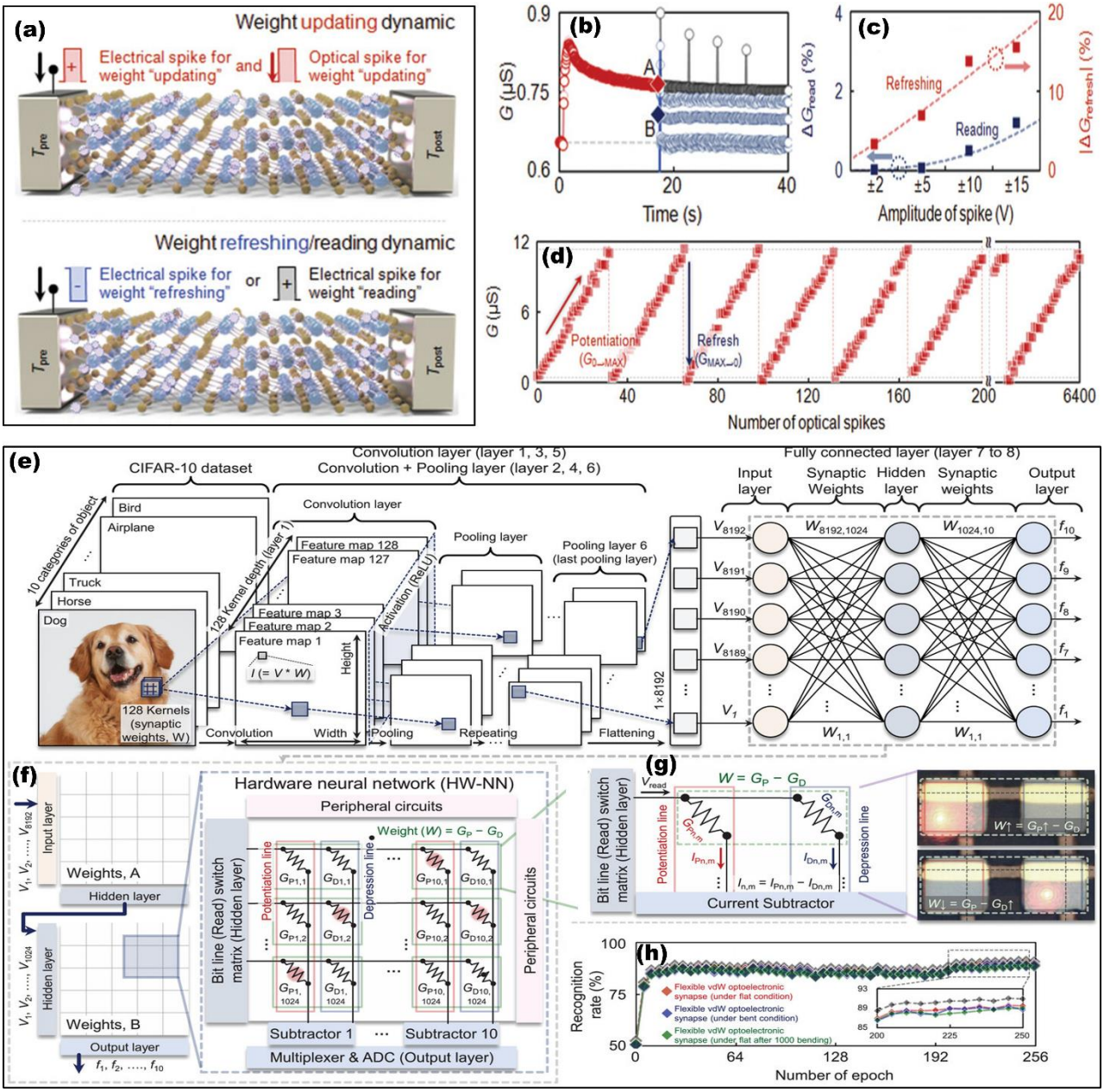

Fig. 5. (a) The schematic representation of the working mechanism of the vdW optoelectronic synapse device with optically and electrically weight updation (top) and electrically modulated weight updation/reading, (b) Conductance response corresponds to the weight refreshing (black line) and reading electrical spike (indigo line), (c) Change in conductance as a function of electrical pulse amplitude, (d) LTP cycles showing the weight updating and refreshing dynamics, (e) CIFAR-10 dataset with CNN consisting convolution, pooling and fully connected layers, (f) The representation of neural network consisting vdW optoelectronic synapse devices for the fully connected CNN layer, (g) Circuit diagram of HW-NN and OM image of vdW optoelectronic synapses depicting increment and decrement in conductance comprising GP and GD, (h) Recognition rate for the CIFAR-10 dataset. Reproduced or adapted with permission from Ref. [127] Copyright [2021] [Wiley].

Later, Liu *et al*. [42] demonstrated a 2D transition-metal tri-chalcogenides (TMTCs) titanium trisulfide (TiS_3) based optoelectronic memristive device with a sandwich-like structure Al/TiS_3/ITO, wherein TiS_3 is a photosensitive material and Al and ITO are the top and bottom electrodes, respectively. The fabrication process of TiS_3 is shown in **Fig. 6(a)**. The solution of TiS_3 nanoribbon is dropped onto the

ITO substrate and spin-coated at 1200 rpm for 30 s. The top electrode of 100 nm thickness is deposited using the thermal evaporation method to fabricate the Al/TiS_3/ITO structure (see **Fig. 6(b)**). The filament-forming process under light illumination is depicted in **Fig. 6(c),** explaining that the excess photo-generated charge carriers in the active layer migrate and accumulate in the vicinity of the Al filament. Hence, the oxidation of the Al metal filament is inhibited under illumination, and the darkness intricate the rupture of the filament, resulting in a smaller Schottky barrier (see **Fig. 6(d)**). **Fig. 6(e)** shows the light and electric-induced potentiation and habituation, respectively. Additionally, the optical response is studied with multiple wavelengths ranging from 400 to 808 nm to realise the multilevel storage. The resistive switching from the HRS to LRS is obtained without forming a process with a large ON/OFF ratio (~400) and long retention time (~10^4 s) at the operating temperature of 85 °C (see **Fig. 6(f)**). As depicted in **Fig. 6(g)**, the bipolar resistive switching is achieved by the formation and breaking of the conductive Al filament. The fabricated devices exhibit cyclic endurance up to 100 cycles, as depicted in **Fig. 6(h)**. The investigation of the synaptic-like behaviour of TiS_3-based optoelectronic memristive device is also studied, which corresponds to the conduction modulation, replicating synaptic plasticity. The device conductance increases or decreases with the negative/positive voltage pulse and multilevel resistance during the LTP, and LTP is maintained over 20 pulses. Lastly, Pavlov's dog experiment is conducted to simulate classical conditioning, wherein the secretion of saliva in a dog is dependent on the conditioned and unconditioned stimulus, diction as a ringing bell or food, respectively. For the experiment, food as an unconditional signal is optically stimulated, while the electrical spike works as a conditioned stimulation. **Fig. 6(i)** unveils that, upon illumination, the current increases significantly and overcomes the threshold value, leading to the secretion of saliva. In contrast, the positive voltage results in a decrease in the current below the threshold value, which is associated with the forgetting process in biological systems. Thereby, Pavlovian associative learning is also established with a TiS_3-based memristive device, highlighting the potential of 2D TMTCs for artificial bionic visual systems. However, this work emphasises that the switching mechanism is primarily dominated by the Al ions, but the role of sulfur vacancies in filament formation is not addressed. The conductance change under different optical wavelengths is relatively small (from ~4.2 mS to 6.36 mS), which limits the precision tuning of the synaptic weight modulation. Additionally, the device exhibits cyclic endurance up to 100 cycles, which limits the long-term stability. The retention time of ~100 s for the photoinduced states is too short compared to biological memory processes and may not be sufficient for long-term learning in the neuromorphic hardware.

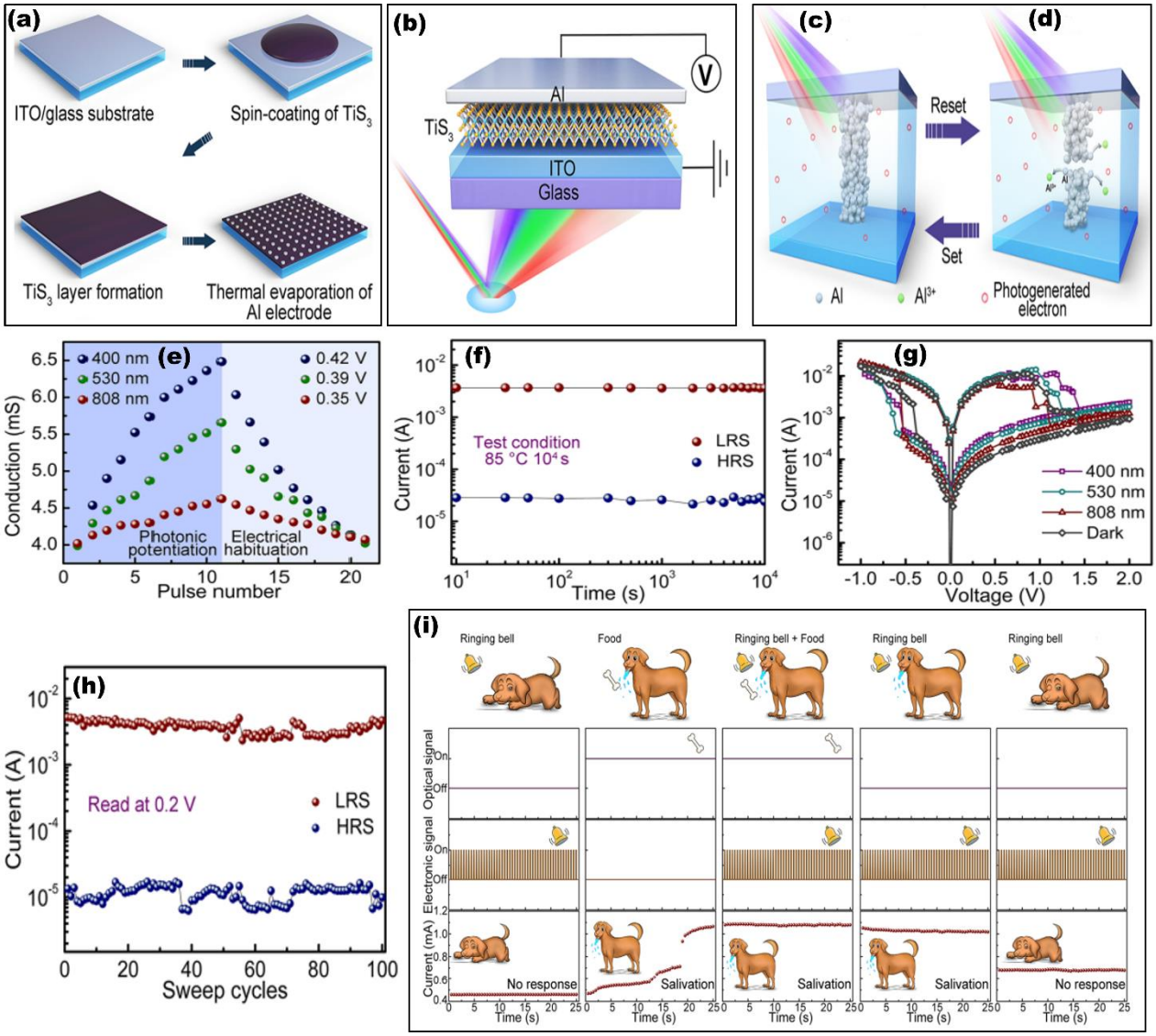

Fig. 6. (a) Schematic of the fabrication procedures, (b) Al/TiS_3/ITO-based memristive device with the experimental setup for backward light illumination, (c-d) conductive filament formation and rupture in the LRS and HRS, (e) conductance change under optical and electric signals, (f) data retention characteristics; (g) I-V curves upon illumination by different wavelengths, (h) endurance characteristics over 100 cycles with distinct HRS and LRS states, (i) Simulation of classical conditioning in Pavlov's dog experiment [42]. Reproduced or adapted with permission from Ref. [42] Copyright [2021] [American Chemical Society].

Recently, Bismuth oxyiodide (BiOI) has garnered attention owing to its layered structure and high photocatalytic activity [130]. The BiOI layer is stacked by the van der Waals (vdW) force, and each layer comprises $[Bi_2O_2]^{2+}$ sandwiched between two layers of I^- ions, as shown in **Fig. 7(a)** [130]. Benefitting from the outstanding electrical and optoelectronic properties of BiOI, it has been anticipated as a promising candidate for application in memristive devices with neuromorphic memory function. Lei *et al*. [44] demonstrated the resistive switching mechanism in 2D BiOI nanosheets together with light-induced synaptic plasticity behaviour. The 2D BiOI nanosheet is sandwiched between Ag and Pt as top and bottom electrodes, respectively, to fabricate a vertical memristive device,

as shown in **Fig. 7(b)**. **Fig. 7(c)** exhibits the optical image of the fabricated memristive device on a Si/SiO_2 substrate, and the inset shows the schematic of the memristive cell.

Under the application of the positive bias, the electroforming process initiates with the migration of Ag^+ ions toward the Pt electrode, forming a conductive channel, and the device is switched from HRS to LRS. The opposite phenomenon takes place during negative biasing, as shown in **Fig. 7(d)**. Moreover, Joule heating also plays a crucial role in rupturing the conductive filament when the device is at LRS [131]. The Joule heating can be restricted by decreasing the compliance current (I_{CC}), suggesting Write-Once-Read-Many-Times (WORM) memory behaviours. The WORM behaviours of the memristive device with I_{CC} of 10^{-6} A and 10^{-8} A are shown in **Fig. 7(e)** and **Fig. 7(f)**, respectively. Therefore, the Joule heating is not sufficient to rupture the conductive filament, and the device cannot be reset to the HRS. The device exhibits a non-volatile nature with an ON/OFF ratio of 10^4, suggesting good data retention performance (see **Fig. 7(g)**). The device also exhibited short- and long-term plasticity behaviour. The PPF is also found to increase with the decrease in pulse interval, similar to the biological synapses. The endurance and cumulative probability performance for 50 cycles were measured, and no noticeable deterioration was observed, as depicted in **Fig. 7(h)** and **Fig. 7(i)**, respectively. However, to further analyse the device stability, a longer cycle endurance measurement should be investigated, because some noticeable degradation was observed in HRS states that might have led to device failure.

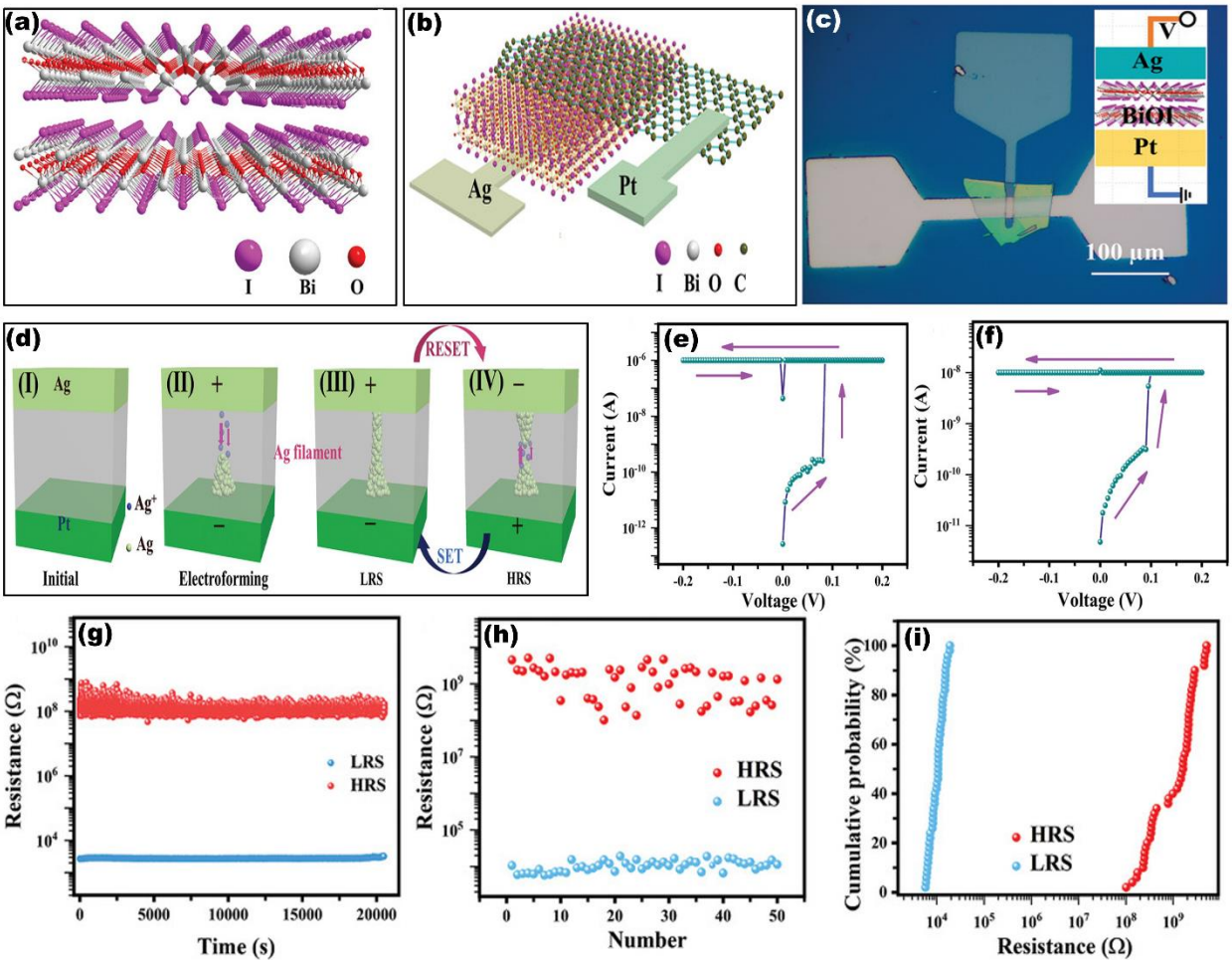

Fig. 7. (a) Schematic of BiOI layered structure, (b) Schematic of the Pt/graphene/BiOI/Ag structure, (c) Optical microscope image of the fabricated memristive device on Si/SiO_2 substrate and the inset shows the schematic of the memristive cell, (d) Illustration of the RS physical mechanism, WORM behaviors of the memristive device with ICC of (e) 10^{-6} A, and (f) 10^{-8} A, (g) Retention characteristics of the BiOI-based memristive device, (h) Endurance performance up to 50 cycles, (i) The cumulative probability of the LRS and HRS for the 50 cycles in the endurance performance. Reproduced or adapted with permission from Ref. [44] Copyright [2022] [Wiley].

The optoelectronic properties of the device are also investigated by replacing the top electrode with graphene. When the device is exposed to light power ranging from 0 to 800 μW cm^{-2}, a steady increase in PSC is observed due to photo-generated charge carriers, emulating STP as shown in **Fig. 8(a)**. The STD or decrease in current over time is observed due to the recombination of photogenerated charge carriers. **Fig. 8(b-c)** shows the current behaviour under illumination of light power of 400 μW $cm^{-2,}$ having a duration of 10 s with different pulse durations of 10 s and 30 s. Furthermore, **Fig. 8(d)** exhibits that the current is increasing with the light duration, the decay time is prolonged, and the amplitude of dark current is increased. **Fig. 8(e)** displays the gradual increase in current under light stimulation, emulating human learning. The device exhibits a continuous potentiation trend when stimulated by the subsequent optical pulses, suggesting LTP characteristics. The re-learning behaviour of the fabricated device is shown in **Fig. 8(f)**, which revealed that for the re-learning process, only 3 light pulses are

sufficient to attain the same current level as the previous 20 pulses in the first learning process. Inspiringly, the 2D BiOI-based memristive device showed a typical "learning experience" nature under the illumination of sequential light pulses, suggesting that photonic synapses have the potential to stimulate human learning. A small image version (8×8 pixels) of handwritten digits from the "Optical Recognition of Handwritten Digits" dataset is analysed, and ~ 80 % recognition accuracy is achieved after 40 epochs. However, the recognition accuracy is low, but it can be further enhanced by optimising the photosensitive materials and device structure.

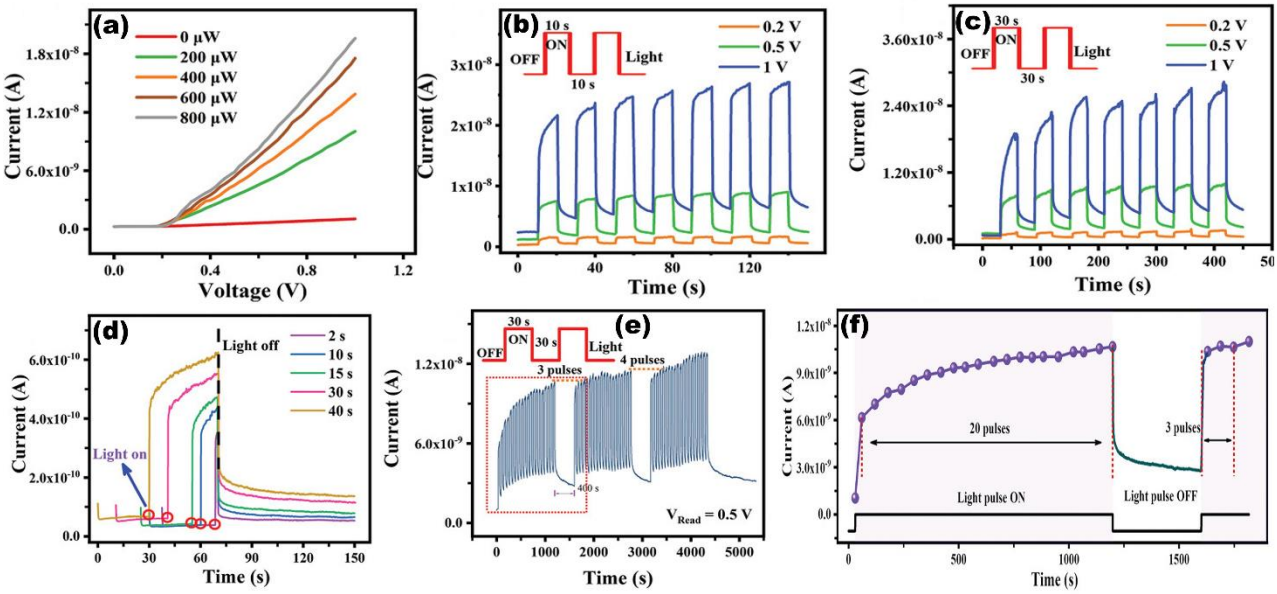

Fig. 8. (a) I-V characteristics of Pt/graphene/BiOI/Ag device with light power ranging from 0 to 800 μW cm^{-2}, (b) The behavior curve under illumination with a light pulse duration of 10 s and (c) 30 s, (d) current trend with light power of 250 μW cm^{-2} and pulse duration from 2 to 40 s,(e) The current response stimulated by three light sequences with each sequence consisting of 20 light pulses, (f) The "learning experience" processes by replotting the current curve. Reproduced or adapted with permission from Ref. [44] Copyright [2022] [Wiley].

Kumar *et al*. [46] demonstrated a flexible Cu/Hafnium oxide (HfO_x)/Pt and bilayer Cu/HfO_x/ Black phosphorus (BP)/Pt-based optoelectronic memristive device, which is inherent in both electrical and optical synaptic functions. The BP has gained attention due to its layered structure and high carrier mobility, along with strong in-plane anisotropy properties. The HfO_x-based memristive device shows poor endurance (100 cycles) due to the wider dispersion in SET and RESET voltage, attributed to the stochastic formation and rupture of CFs [132-133]. The HfO_x layer limits the migration of Cu ions, resulting in a low ion transport rate in the oxide layer. The filament diameter starts to spread again at the interface of HfO_x/BP, showing the increment in Cu ion transportation, which is attributable to the high thermal conductivity of BP [134]. This phenomenon leads to the formation of an hourglass-shaped Cu filament, and the weakest point of the filament is formed at the interface of HfO_x/BP, contributing to different ion mobility characteristics. When the negative pulse is applied, the filament ruptures at its weakest points due to the Joule heating, which leads to the diffusion of Cu ions, resulting in the

device switching from LRS to HRS. **Fig. 9(a)** shows the entire switching mechanism process of the fabricated devices. **Fig. 9(b)** illustrates the I-V curves of the HfO_x/BP-based devices up to 1,000 consistent cycles with excellent stability and reproducibility. The HfO_x/BP- devices showed the sharp distribution of V_{SET} and V_{RESET}, resulting in stable RS switching with endurance of up to 1,000 cycles without degradation, as shown in **Fig. 9(c)**. The device also showed stable synaptic properties, including LTP and LTD for repetitive 1000 epochs, with each epoch having 400 conducting pulses. The artificial neural network (ANN) consists of three layers: an input layer with 28×28 neurons, a hidden layer with 100 neurons, and an output layer with 10 neurons, used for accurate training on the MNIST pattern recognition task. The experimental results revealed that a stable accuracy of 90.16% is achieved after 150 training epochs (see **Fig. 9(d-f)**).

This work is further extended with the study of the optoelectronic synaptic feature of the proposed device by applying a series of light pulses with different intensities and time durations shown in **Fig. 9(g)**. The tuning in light intensity leads to different amounts of light absorption, which corresponds to the different excitation energies, resulting in different charge trapping/de-trapping and multiple resistance states. Additionally, the interface barrier between HfOx and BP suppresses the recombination of photogenerated carriers, extending their lifetime and allowing the device to maintain a non-volatile LRS even after the light stimulus is removed. The light exposure leads to an increase in photocurrent and later degrades to its initial level after a given time, replicating the learning and forgetting phenomenon. **Fig. 10(a)** exhibits synaptic photonic PPF functionality, which is a crucial property for neuromorphic vision systems. The transformation from short-term memory (STM) to long-term memory (LTM) is achieved with continuous learning and forgetting processes, enhancing memory ability displayed in **Fig. 10(b-c)**. **Fig. 10(d)** shows a model in which new information is stored in the sensory register for a very short time, and then the information is transferred from STM to permanent LTM storage. **Fig. 10(e)** demonstrates that the memorisation level is increased marginally with the initial learning, and thereafter the memorisation level increases temporarily in STM before decaying. Next, the repeated re-learning results in LTM, leading to permanent memorisation. The learning-forgetting-learning behaviour of the memristive device is depicted in **Fig. 10(f)**.

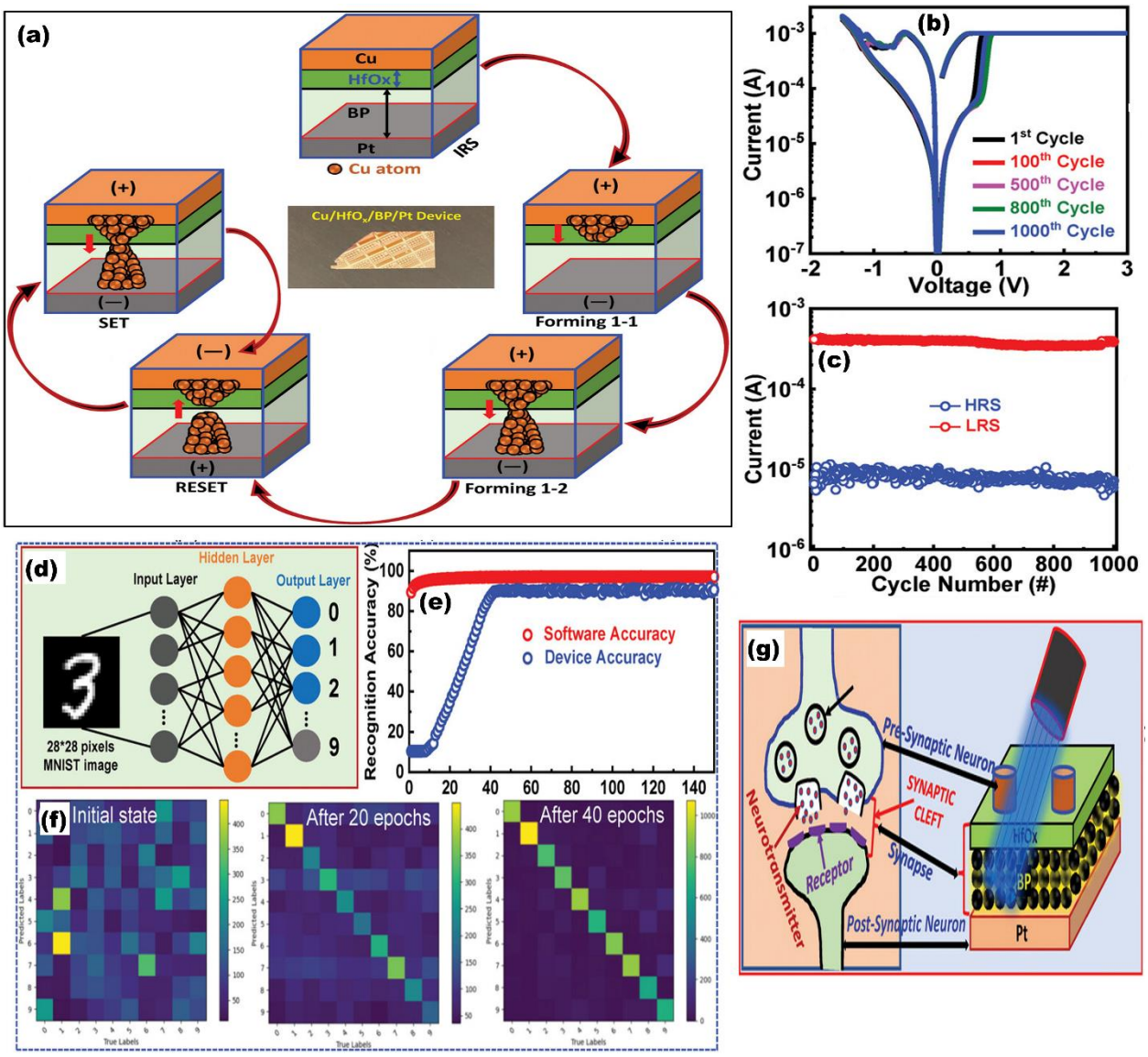

Fig. 9. (a) Switching mechanism in Cu/HfO_x/BP/Pt-based memristive devices, (b) 1,000 cycles of I-V responses of the HfO_x/BP-based memristive device, (c) DC endurance of the HfO_x/BP device, (d) The ANN network structure consisting of input, hidden and output layers, (e) The recognition accuracy increases with the training epochs, (f) Confusion matrix with different training states, (g) Schematic design of the biological synapse and artificial optoelectronic memristive synapse. Reprinted with permission under a Creative Commons CC-BY license from Ref. [46] Copyright [2023] [Wiley].

The vision memory function is also validated in a (6×6) memristive device array by using a light stimulus of 405 nm wavelength as illustrated in **Fig. 10(g)**. The five different regions named I, II, III, IV, and V are exposed to different light intensities of 68, 57, 48, 32 $mWcm^{-2,}$ and dark, respectively, as shown in **Fig. 10(h)**. The result depicted that the modulation in conductance state change corresponds to different optical stimuli intensities and time leads to the learning-forgetting-re-learning" process, which emulates the human visual perception property (see **Fig. 10(i)**). In summary, the synergistic effect of synaptic learning and optical sensing makes it a promising candidate for optoelectronic memory storage for artificial visual systems. However, the endurance measurement under bending is tested for only 100 cycles, which is insufficient for most flexible electronic systems. In addition, although the active layers are reported as biocompatible, the dependence on a silicon substrate limits practical flexibility and would require complex packaging for wearable or implantable applications.

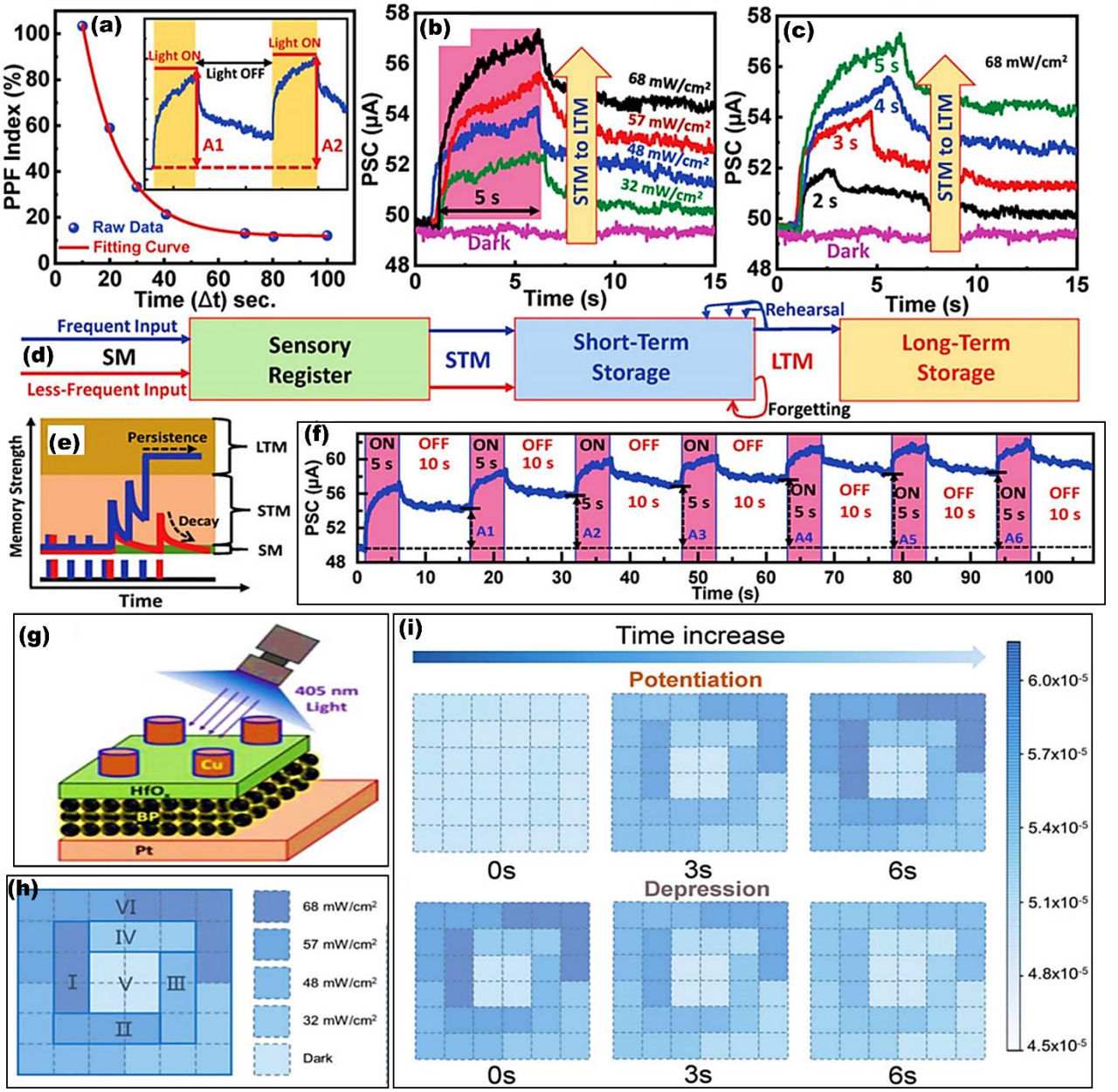

Fig. 10. (a) The PPF index variation of photonic pulse pairs along, Inset represents the PSC under blue light with an intensity of 68 mWcm^{-2} and time interval of 20 s, (b) PSC trend of light exposure for 5 s at a different light intensity and in dark condition, (c) PSC response under a light intensity of 68 mWcm^{-2} with different time duration, (d) Multi-storage psychological paradigm of the human memory system, (e) Memory strength model in the device, (f) The learning-forgetting-re-learning process for seven cycles, (g) illustration of giving a light pulse to device, (h) Image mapping of the (6×6) arrays with five different light intensities, (i) Conductance mapping to the (6×6) array in both potentiation and depression states with corresponding time at 0, 3, and 6 s. Reprinted with permission under a Creative Commons CC-BY license from Ref. [46] Copyright [2023] [Wiley].

Artificial photonic synapse exhibits dual characteristics of photo-detecting and synaptic elements, allowing temporary memory under the influence of light stimuli [135]. Hence, photonic synapses can mimic the visual perception by responding to the history of light signals, such as their intensity, number, duration, and frequency. In addition, to wide bandgap, high interference immunity, and low crosstalk properties make them ideal to mimic the visual perception of the retina [136]. The 2D

organic-inorganic halide perovskite (OIHP) is believed to be more stable, with inhibiting ion migration due to its higher formation energies and augmented dielectric confinement by organic spacer cations [137].

Owing to these characteristics, a 2D OIHP Bis(butylammonium) lead tetraiodide $(BA)_2PbI_4$-based memristive device is demonstrated by Wang *et al*. [52] to explore their application for human visual systems. The OIHP-based memristive device with ITO/$(BA)_2PbI_4$/ITO structure (see **Fig. 11(a)**) exhibits a neuron-like response under optical stimuli, enabling synaptic plasticity along with learning and memory function. The resistive switching was observed under different direct voltage sweeps, showing nonlinear current-voltage characteristics.

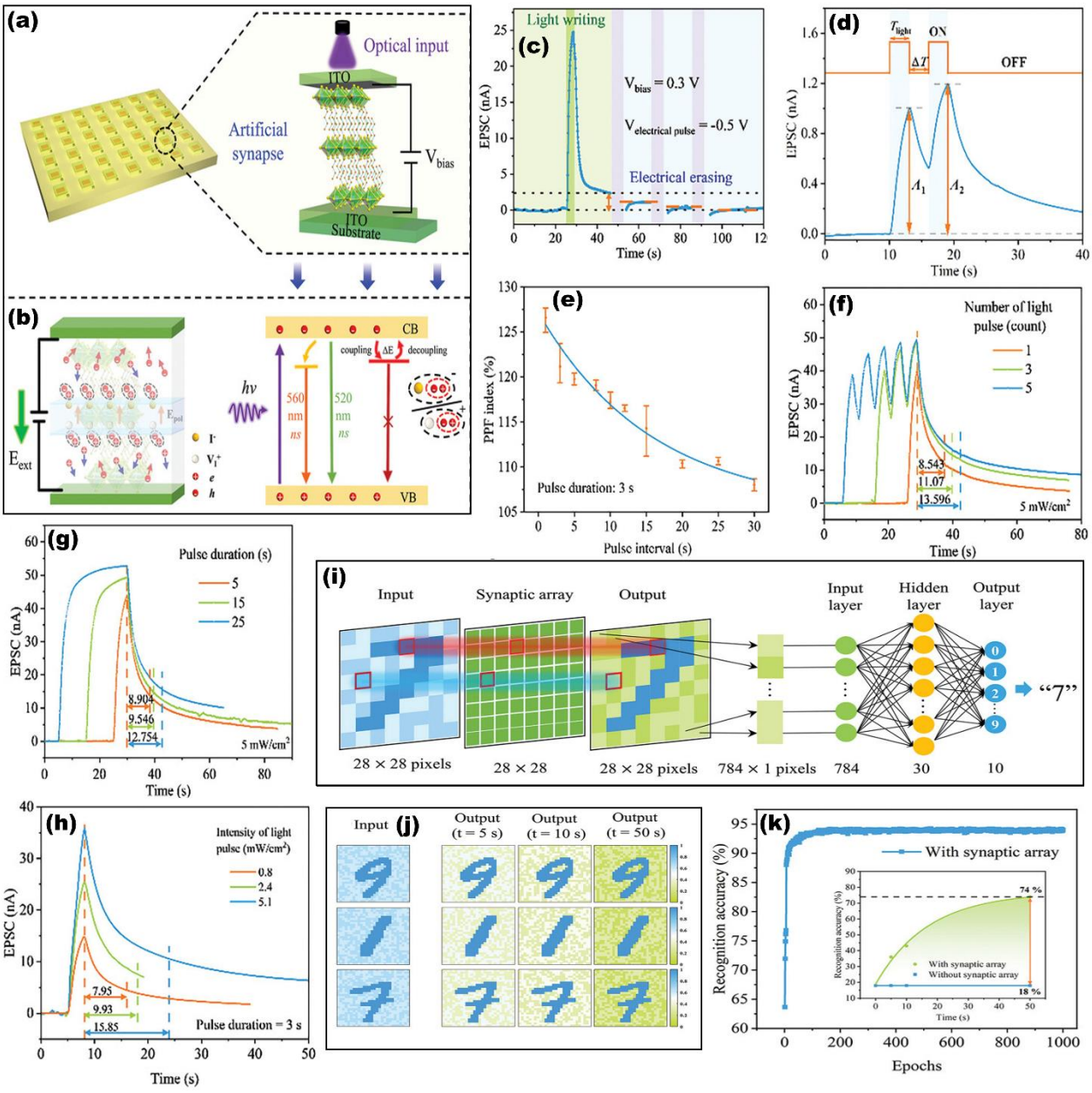

Fig. 11. (a) The artificial visual system based on ITO/$(BA)_2PbI_4$/ITO, (b) The mechanism of exciton-ion coupling which is responsible for the nonvolatile photocurrent, (c) EPSC response of the device with light writing (green region) and voltage erasing (blue regions), (d) PPF curve at two successively applied light pulses, (e) PPF as a function of pulse interval, (f) transition from STP to LTP with increasing number of pulse, (g) transition from STP to LTP with pulse duration, (h) transition from STP to LTP with the intensity of pulse, (i) Illustration of the synaptic array for image preprocessing and an artificial neural network for image recognition, (j) The input and output images at different preprocessing times, (k) the recognition accuracy at different epochs. The inset shows the image recognition accuracy for noisy images with and without preprocessing. Reprinted with permission under a Creative Commons CC-BY license from Ref. [52] Copyright [2024] [Wiley].

As illustrated in **Fig. 11(b)**, the electrical stimulation initiates the migration of iodine vacancies vertically within the inorganic layer, and simultaneously, the negative charge ion moves against the direction of the external field. However, the BA^+ cation is believed to hinder the iodine ions, leading to an increase in ion migration potential. Due to the ion redistribution within the inorganic layer, a quantum-confined polarisation field (E_{pol}) is induced. While applying the optical stimulus, this E_{pol} acts as a trap state for the photo-generated charge carriers via Coulomb interaction that leads to persistence photoconductivity (PPC). Light pulse-modulated synaptic characteristics were investigated by applying a small voltage of 0.1 V together with a light pulse at 410 nm with a duration of 3 s, showing an abrupt increment in excitatory postsynaptic current shown in **Fig. 11(c-d)**. The observed optical response is analogous to the STP involved in the encoding of visual signals, which play a pivotal role in pattern recognition and associative learning. PPF is also calculated as a function of pulse interval and found that it increased from 109% to 126% with the reduction of pulse duration from 30 s to 1 s (see **Fig. 11(e)**). The spike-number-dependent potentiation (SNDP) is also reported with an increasing number of optical pulses. A long, sustainable current is observed as the number of optical pulses is increased from 1 to 5, with a relaxation time of 13.579 s shown in **Fig. 11(f)**. In addition, EPSC also varies with pulse duration, pulse interval, and pulse intensity. This demonstrates spike-intensity-dependent potentiation (SIDP) and spike-time-dependent potentiation (STDP) **(see Fig. 11(g-h)).** Lastly, the MNIST dataset is used for training and testing of the (28×28) synaptic arrays, refer to **Fig. 11(i-j)**. It was observed that the recognition rate reached 94.01% by increasing the training epochs (see **Fig. 11(k)**). Hence, light-tunable synaptic plasticity enables the realization of first-stage image processing, including image contrast improvement with less noise. The facial recognition model is much more effective than the ANN, which can significantly learn visual features for recognizing target images. In this work, 2D OIHP single crystals are proposed as more stable candidates with suppressed ion migration. However, ionic motion remains a significant challenge in the OIHP. The ion translocation within inorganic layers cannot be prevented by organic spacers, leading to long-term instability in the device operation. The stability under ambient conditions and long-term device endurance under continuous light and electrical stimuli are not addressed.

In the 2D material space, Molybdenum disulfide (MoS_2) is a striking candidate due to its transition from an indirect bandgap of 1.2 eV to a direct bandgap of 1.8 eV. However, earlier reports suggest that the MoS_2-based device inherently has a narrow memory window at low operating voltage, insufficient charge storage, and poor endurance, limiting their use in artificial intelligence [138-143]. Kumar *et al*. [48] designed a MOS memory architecture wherein 2D MoS_2 light-sensitive material is utilized as a charge-trapping layer. **Fig. 12(a)** illustrates the fabrication of an $Al/Al_2O_3/MoS_2/Al_2O_3/P^+$-Si-based memristive device. The MoS_2 layer is sandwiched between the two Al_2O_3 atomic layers to design a charge-trapping memory architecture. The fabricated device showed enhancement in the memory window from 2.8 V to 6 V under the application of optical stimuli of 400 nm wavelength, along with a programming voltage of ±6 V, as shown in **Fig. 12(b-c)**. **Fig. 12(d)** shows the shift in the threshold voltage with the decreasing wavelength is explained by the larger charge trapping at the Al_2O_3/MoS_2. The optical characteristic of the device with different wavelengths ranging from 600 to 400 nm is shown in **Fig. 12(e)**. The optical stimulation increases the threshold voltage from 2.5 to 3.3 eV, which is explained as the device trapping a greater number of electrons compared to dark conditions. Furthermore, the device exhibits stable endurance for up to 10^3 cycles, and the data is sustained for at least 10^3 minutes and predicted to have more than 10 years, as depicted in **Fig. 12(g-h)**.

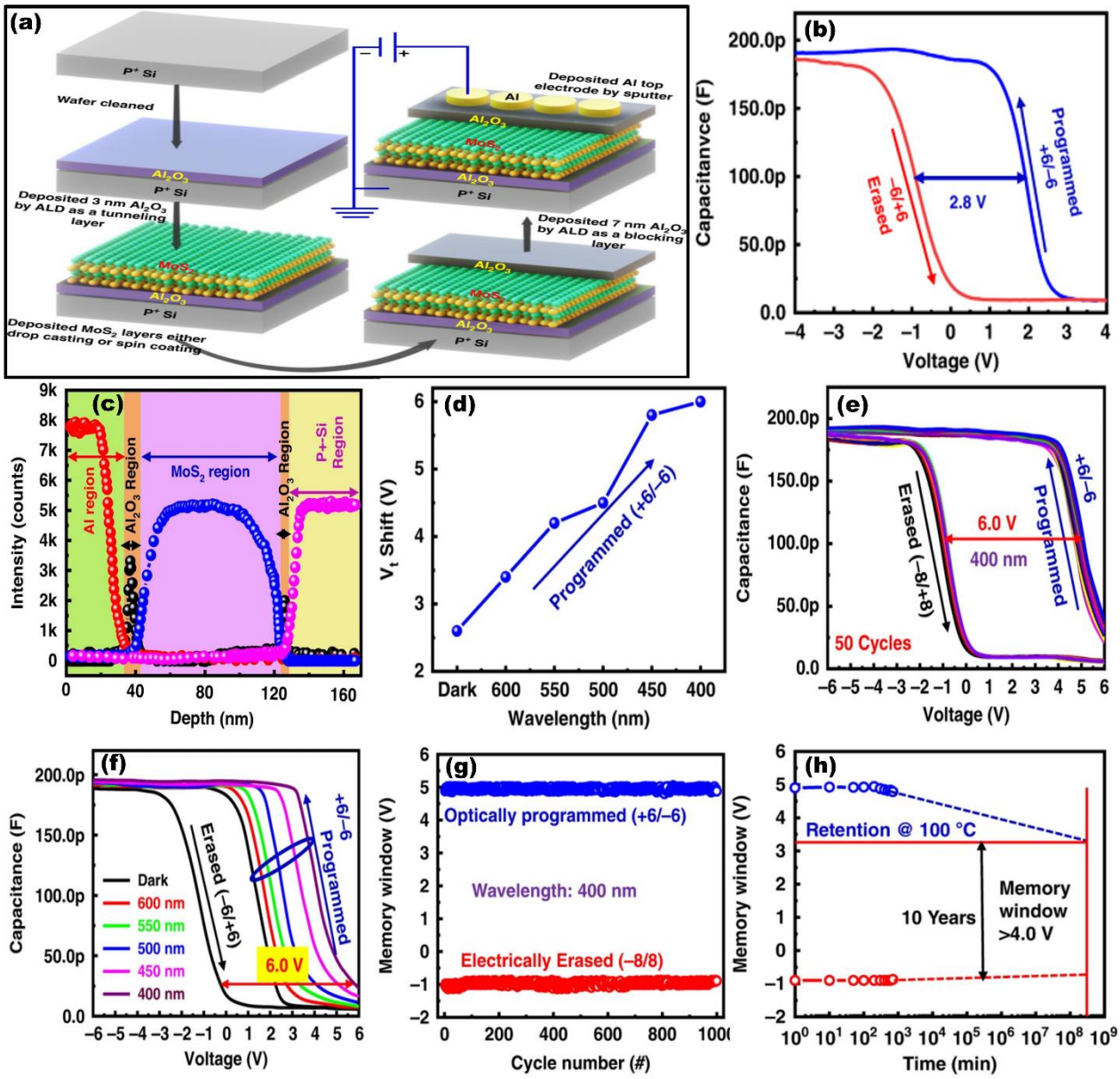

Fig. 12. (a) Schematic representation of the fabrication process of MOS memory device, (b) C-V curve depicting the memory window of 2.8 V, (c) Secondary ion mass spectrometry (SIMS) depth profile of Al/Al2O_3/MoS_2/Al_2O_3/P^+-Si, (d) wavelength-dependent threshold voltage of the device, (e) C-V curve for 50 continuous cycles with optical sweep (+6/-6) and electrically erasing with voltage sweep (+8/-8), (f) C-V curve employing different wavelength ranging from 600 to 400 nm with the pulse duration of 50 nm, (g) optically programmed and electrically erased endurance with 400 nm wavelength, (h) high-temperature retention stability of the device. Reprinted with permission under a Creative Commons CC-BY license from Ref. [48] Copyright [2023] [Springer Nature].

Fig. 13(a) shows the C-V response of the device, which can be successfully programmed and erased with optical and electrical stimulation, respectively. Here, a 400 nm wavelength optical source was used with a different pulse width (1 µs to 75 µs) that certainly modulates the memory window of the device. **Fig. 13(b)** and **Fig. 13 (c)** show the optically potentiation and electrically depressing processes, respectively. During the potentiation, different pulse width (1 µs to 75 µs) with a constant wavelength (or power) is utilized, while under the depression process, varied amplitudes of electrical pulses are used as depicted in **Fig. 13(b-c)**. Furthermore, a small CNN model was designed to validate the electrical programming capability of the device, as shown in **Fig. 13(d)**. Herein, the Canadian Institute

for Advanced Research (CIFAR)-10 dataset is used for the simple binary image recognition [144], and dogs and automobiles were chosen (see **Fig. 13(e)**). As shown in **Fig. 13(f)**, the software test was trained on 32-bit floating point arithmetic by default, and an accuracy of 95.41% was achieved, while the accuracy of 91.03% was obtained through an offline mapping kernel with $Al/Al_2O_3/MoS_2/Al_2O_3/P+$-Si device. The device exhibited a memory window of ~2.8 V at ±6 V, which further increased with higher sweeping voltages, reaching a maximum of ~5.9 V at ±10 V, indicating excellent charge-trapping capability. However, the requirement of such high operating voltages to achieve a large memory window raises concerns about energy efficiency and scalability for low-power neuromorphic applications. Furthermore, effective programming requires relatively high optical intensity (400 nm, 50 mW cm^{-2}) and long irradiation times (up to 75 µs), and subsequently, electrical erasing with high-voltage sweeps (−6/+6 V to −14/+14 V) complicates circuit integration for practical applications.

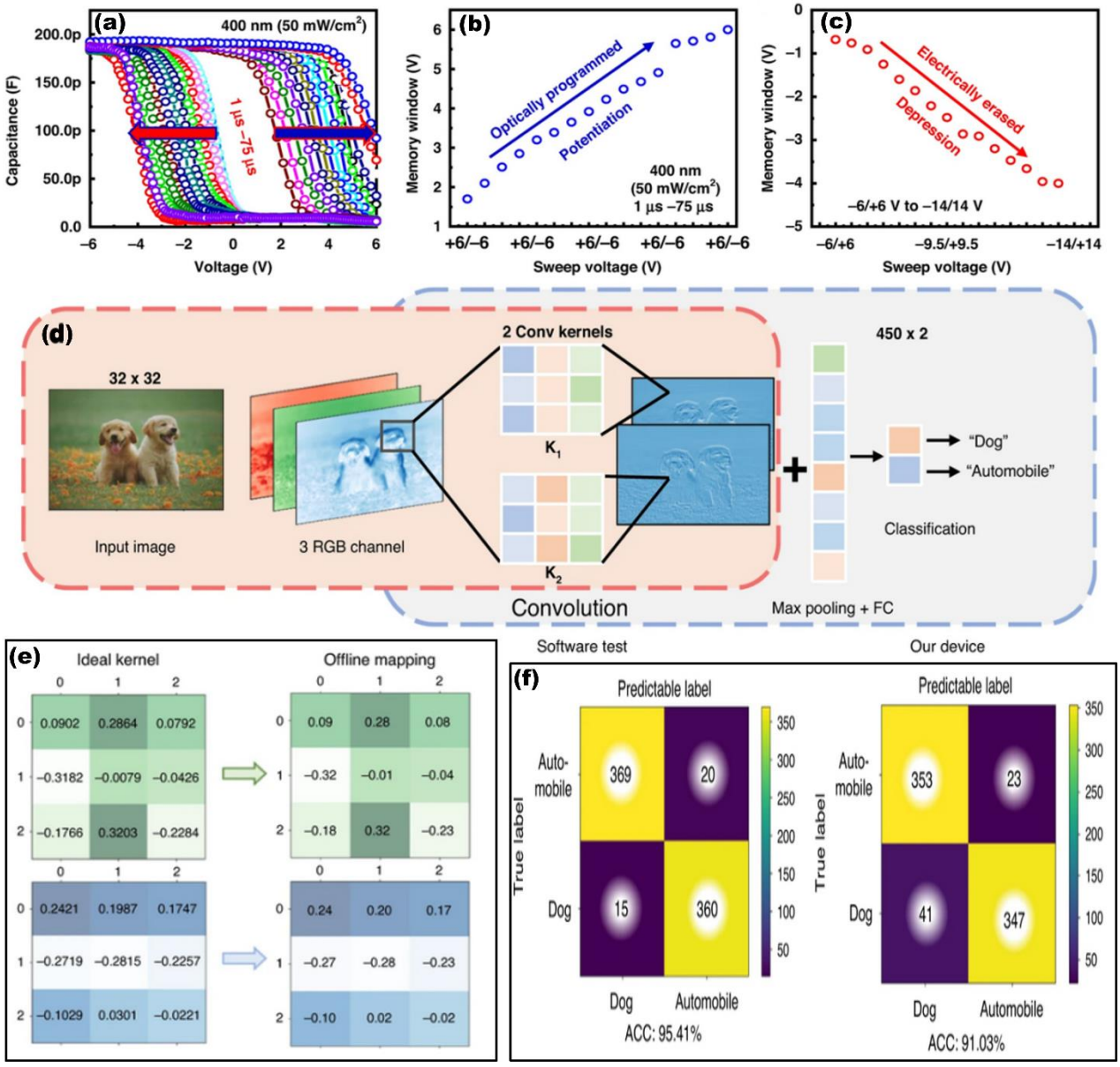

Fig. 13. (a) C-V curve of $Al/Al2O_3/MoS_2/Al_2O_3/P^+$-Si under light intensity of 50 $mWcm^{-2}$ (b) memory window of optically programmed device, (c) memory window of electrically erased device, (d) A CNN model employed to make a binary classification over the CIFAR-10 dataset, (e) The kernels (left) are obtained from the ideal software test. The offline

mapping kernels (right) are transferred from the corresponding ideal kernel values by illuminating and programming the device. (f) Confusion matrix of the test results for 764 images in the CIFAR-10 dataset. Reprinted with permission under a Creative Commons CC-BY license from Ref. [48] Copyright [2023] [Springer Nature].

Recently, wide bandgap metal oxide semiconductors have emerged as promising candidates due to their transparency to visible light, high conductivity, and unique electronic structure for optoelectronic applications [145]. Owing to these inimitable properties, Kumar *et al*. [54] demonstrate a zinc tin oxide (ZTO)/indium (III) oxide (In_2O_3)-based optoelectronic device (ITO/ZTO/In_2O_3/Pt) for sensing different light intensities and perceiving motion behavior (see **Fig.14 (a-b)**). In particular, In_2O_3 and ZTO have a wide optical band gap of 3.6 and 3.8 eV, respectively. The exceptional absorption properties in the ultraviolet spectrum make them promising candidates for visible light sensors. The synaptic behavior and current-voltage responses of the ITO/ZTO/In_2O_3/Pt memristive device are showcased in **Fig. 14(c),** showing bipolar resistive switching. The DC endurance was demonstrated at a read voltage of 0.1 V, resulting in high stability over 2,000 cycles without any degradation (see **Fig.14 (d)**), and the ON/OFF ratio is found to be in the order of 10^3.

Furthermore, the LTP and LTD behaviors were also investigated by employing 50 positive and 50 negative identical pulses, and the device exhibits the capabilities of modulating synaptic weight (see **Fig. 14 (e)**). In addition, **Fig. 14(f)** successfully validates the PPF functionalities by using two sequential light pulses, and the initial facilitation magnitude is increased from 8.96 % to 21.42 %, highlighting its ability to emulate biological phenomena.

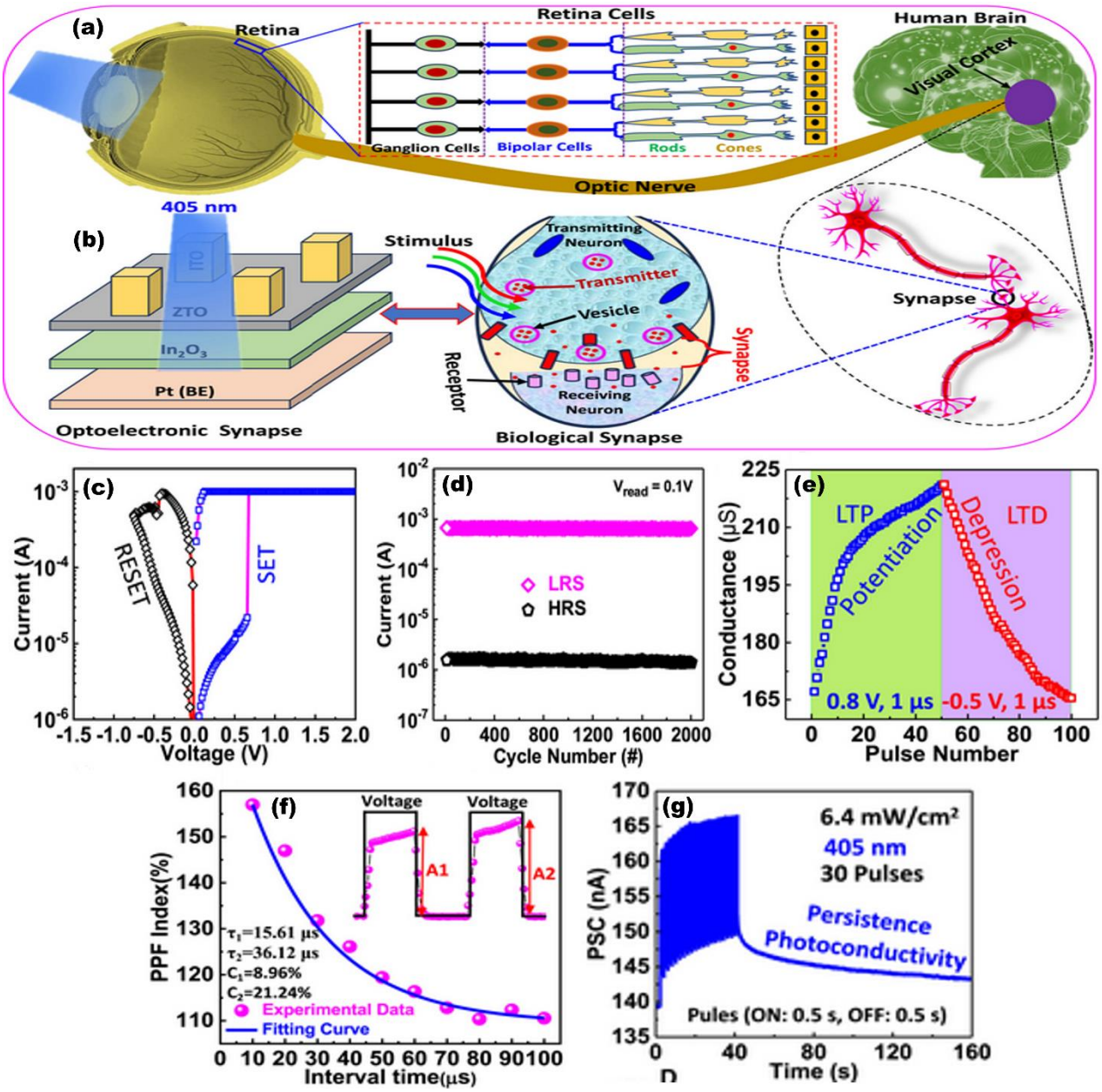

Fig. 14. (a) Schematic diagram of the retina and brain within the biological human neural visual subsystem, (b) Illustration outlining neurotransmitter between pre-synaptic and post-synaptic sites in the retina alongside an optoelectronic memristive array featuring an ITO/ZTO/In_2O_3/Pt bilayer structure, (c) Electrical I-V characteristics of the memristive device highlighting positive SET (0.8 V) and negative RESET (-0.4 V) transitions. (d) DC endurance of the device at a read voltage of 0.1 V, (e) Potentiation and depression of the memristive device induced by a series of voltage pulses (+0.8 V for potentiation, -0.5 V for depression, pulse width: 1 ms), (f) Paired-pulse facilitation (PPF) index of the device, with an inset providing a schematic depiction of the PPF measurement, and (g) PSC response of the device under consecutive 30 light pulses (wavelength: 405 nm, light intensity: 6.4 mWcm^{-2}) [54]. Reprinted with permission under a Creative Commons CC-BY-NC license from Ref. [54] Copyright [2024] [Elsevier].

Furthermore, optoelectronic characteristics with different intensities and durations of the light pulse are delved into, and found that the device exhibits a notable change in photonic post-synaptic current (PSC) in response to light stimuli. Upon exposure to 30 pulses of the optical pulse of 405 nm wavelength at 6.4 mW cm^{-2}, a significant enhancement in the PSC was observed, which was attributed to the photoconductive effect of In_2O_3 and ZTO (see **Fig. 14(g)**). Furthermore, the different optical

pulses of different intensities (2.3, 3.4, 4.7, 5.6, 6.4 $mWcm^{-2}$) depicted in **Fig. 15(a)** demonstrate that the higher intensity pulse corresponds to an enhancement of current conductance, and the rate of decay is affected by the light intensity. A low-intensity pulse slightly increases the current, which quickly decreases after the pulse is removed, similar to STM behavior in the human brain. In contrast, a high-intensity pulse promotes slow decay of the photocurrent, preserving higher levels above its initial state, and emulating LTM. In summary, the transformation from STM to LTM can be achieved by varying the intensity of the pulse and exposure time (see **Fig.15 (b-c)**). In practice, the pupil size reduces to the limit of the light exposure under bright conditions but enlarges in darkness to permit a greater number of photons. **Fig. 15(d)** demonstrates the response of the human pupil to different light intensities. To validate this ability, a "Z" pattern in a 5×5 array was exposed to optical stimuli for 2 s to facilitate learning, followed by a darkness period of 1 s to simulate the memory fading process. Followed by this, the motion detection ability is also demonstrated in memory sensor applications. A customized video dataset is built with five moving directions: up, down, left, right, and static, as shown in **Fig. 15 (e)**. The results signify that the device can efficiently encode video information to capture both temporal and spatial data. Lastly, the ANN network consists of three layers, including the input layer with 784 neurons, a hidden layer of 100 neurons, and the output layer of 5 neurons is used to detect moving objects. The result revealed that the device achieved 95.8 % recognition accuracy after 30 training epochs, which is promising for the application of bionic visual systems (see **Fig. 15(f-h)**). However, the fabricated device operation mechanism is restricted to a single wavelength (405 nm), which limits spectral selectivity and does not reflect the broadband response of the human retina. Lastly, although the device is successfully potentiated by the optical stimuli, electrical pulses are still required for the complete reset process. This led to the asymmetric operational mechanism that complicates circuit integration.

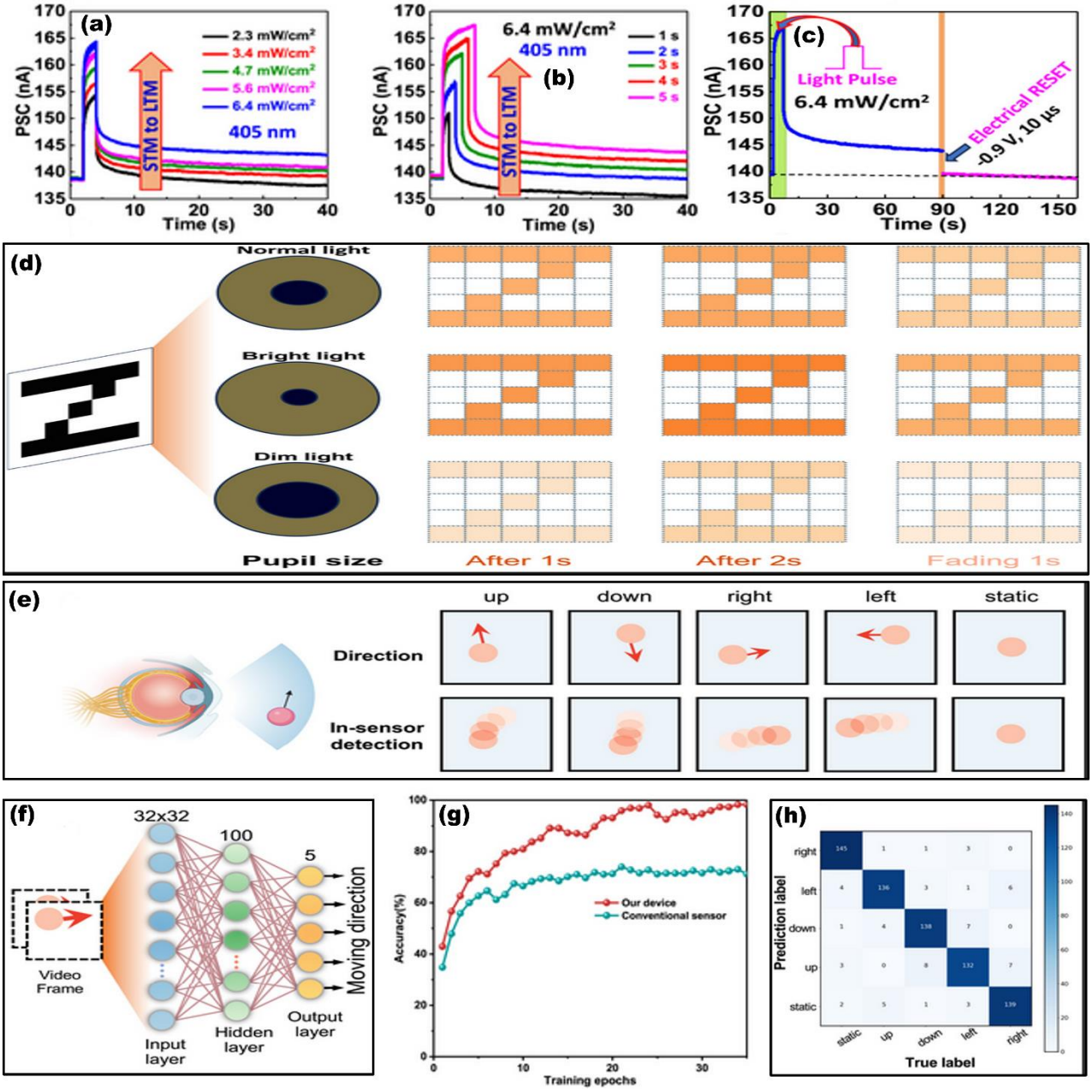

Fig. 15. (a) PSC response under light for 3 s at various light intensities of 2.3, 3.4, 4.7, 5.6, and 6.4 $mWcm^{-2}$, followed by PSC decay when the light is turned off, (b) PSC response under a light intensity of 6.4 $mWcm^{-2}$ with different time durations of 1, 2, 3, 4, and 5 s, followed by PSC decay when the light is turned off, (c) Light-induced PSC using a single blue light (wavelength: 405 nm, light intensity: 6.4 $mWcm^{-2}$, duration: 5 s) and electrical erasure using a voltage pulse (amplitude: -0.9 V, duration: 10 ms) in the device, (d) The different pupil sizes and corresponding conductance changes with fixed exposure and decay time wherein the intensity of a stimulus can influence the retention of response and delay in fading such as variations in light intensity, such as normal light, bright light, and dim light, affect pupil size to regulate the amount of light entering the human eye, (e) Schematic of the human eye detecting the moving object with different directions and the in-memory sensor detection result, (f) ANN network for classifying moving direction, (g) Recognition accuracy comparison between our device and conventional sensor, (h) Confusion matrix after 30 epochs of training. Reprinted with permission under a Creative Commons CC-BY-NC license from Ref. [54] Copyright [2024] [Elsevier].

Lin *et al* [56] designed a heterostructure of CeO_2/MoS_2 to realize the functionality of an artificial visual system, light sensing, and visual nociceptors. The schematic representation of the device is shown in **Fig. 16(a)**. The Ag and ITO are used as the top and bottom electrodes, respectively. Upon illumination, the heterojunction of CeO_2/MoS_2 promotes the carrier migration at the interface, which leads to a controlled light-induced response. The conductance modulation in the CeO_2/MoS_2 with different light intensity (0.097, 0.367, 1.290, 3.538, 4.781, 6.282, 8.460, and 10.842 mW/cm^2) at read voltage of 0.3 V is demonstrated in **Fig. 16(b)**. The larger conductance was observed for higher light intensity, which decays slowly with time when the light is turned off, attributed to the PPC effect. Notably, the STM to LTM was achieved by tuning the light intensity as the decay time is prolonged and remains above the initial state. Similarly, the light-induced response with the same light intensity at a read voltage of -0.3 V is illustrated in **Fig. 16(c)**. By applying the negative read voltage (-0.3 V), the current decays fast due to the inconsistent interface barrier height. **Fig. 16(d)** shows the learning-forgetting process by successively turning the light on/off. The device successfully achieved the relearning process under the exposure to optical pulses. Further, a (9×9) optoelectronic memristor array is fabricated to investigate the co-modulation characteristics. The light-induced response is observed in which current is increased from -251 nA to -800 nA to -3600 nA as the negative voltage increases from -0.5 V to -1 V to -1.5 V, under the light wavelength of 365 nm, as depicted in **Fig. 16(e)**. Lastly, the visual memory capability of the array is investigated by using the "traffic signal". The pattern mapping of the array at different wavelengths is shown in **Fig. 16(f)**. Initially, the device is exposed to light for the duration of 10 s through a shadow mask to create a current mapping pattern. Then, the light is turned off, and a decay trend is observed by applying a read voltage of -0.3 V. Upon light stimuli, the traffic signal pattern representing three different colors (red, yellow, green) is remembered for a short time. After removing the light stimuli, the yellow and green light images were maintained for 60 s, but the red-light image became blurred due to the overall change in device current was not enough (from 82 nA to 84.42 nA). These findings enable the multi-wavelength color image detection function and image memory in bionic visual systems. However, memory retention time needs to be further improved, especially for the red light, by creating defects that can respond at a lower energy to improve the overall change in the device current.

Bian *et al.* [145] demonstrated a 2D Tellurene-based optoelectronic memristor which capable of performing synaptic functionalities under both infrared (IR) light and electrical stimuli. The schematic of the device architecture is shown in **Fig. 17(a)**. A single-module reservoir computing (RC) system designed to process temporal information under optical input, as illustrated in **Fig. 17(b)**.

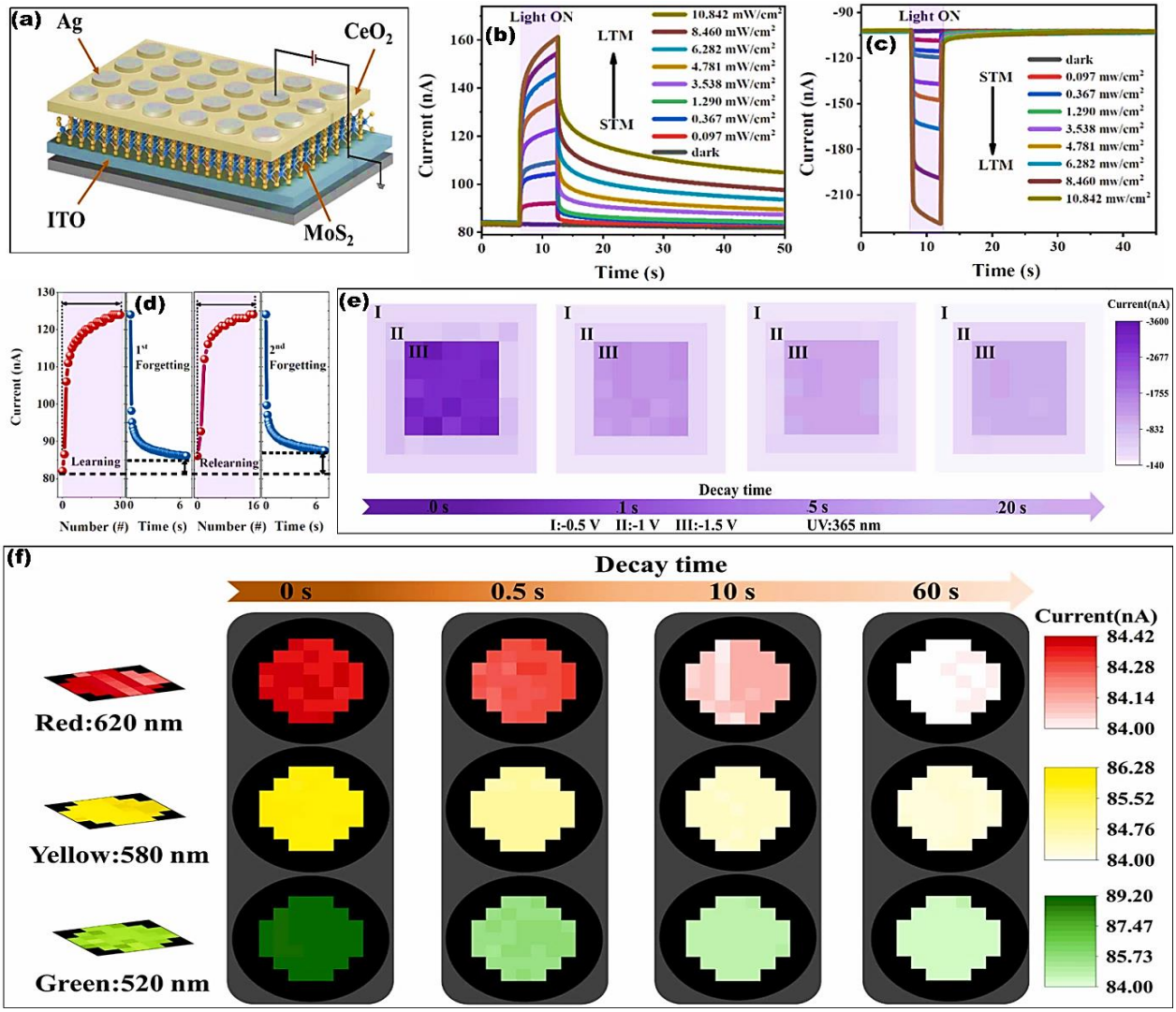

Fig. 16: (a) Schematic diagram of the optoelectronic memristor based on Ag/CeO_2/MoS_2/ITO heterostructure, the current response and decay process for various light intensities (dark, 0.097, 0.367, 1.290, 3.538, 4.781, 6.282, 8.460 and 10.842 mW/cm^2) at (b) positive read voltage (c) negative read voltage, (d) The learning-forgetting-relearning process, (e) sensing and memorizing images is realized using UV light (365 nm) with voltage-assisted modulation, and (f) The traffic light visual array for optical information sense, memory, and color recognition capabilities at different wavelengths (red (620 nm), yellow (580 nm), and green (520 nm)). Reproduced or adapted with permission from Ref. [56] Copyright [2024] [Elsevier].

Fig. 17(c) presents the paired-pulse facilitation (PPF) ratio, where two identical optical pulses at a wavelength of 1022 nm, light intensity of 50 mW mm^{-2}, and a pulse width of 50 ms were applied. The inset reveals that the PPF ratio decreases with shorter inter-pulse intervals. Furthermore, a binary bit stream with different encoding patterns ([1111], [1101], and [0110]) was applied using optical stimuli, as shown in **Fig. 17(d)**. The results demonstrate that the device successfully distinguished all three patterns, as validated by the corresponding current responses. Additionally, the confusion matrices and recognition accuracies of the ECG patterns under different input modes, such as optical, electrical, and mixed, are also investigated, as shown in **Fig. 17(e-f)**. The recognition accuracy is improved to 95.7%

after 200 training sessions through multimodal processing, surpassing the initial accuracy rates of 86.3% and 81% achieved with single-modal approaches. However, the optical mode exhibited a relatively lower recognition accuracy of 81%, which is significantly lower compared to other 2D material-based devices. This necessitates further optimization of the material properties and device architecture to enhance the optical-mode performance. Overall, these results indicate that the tellurene optoelectronic memristor-based MRC system holds strong potential as a high-precision single and multimodal sensory platform, offering valuable insights for future retinomorphic applications.

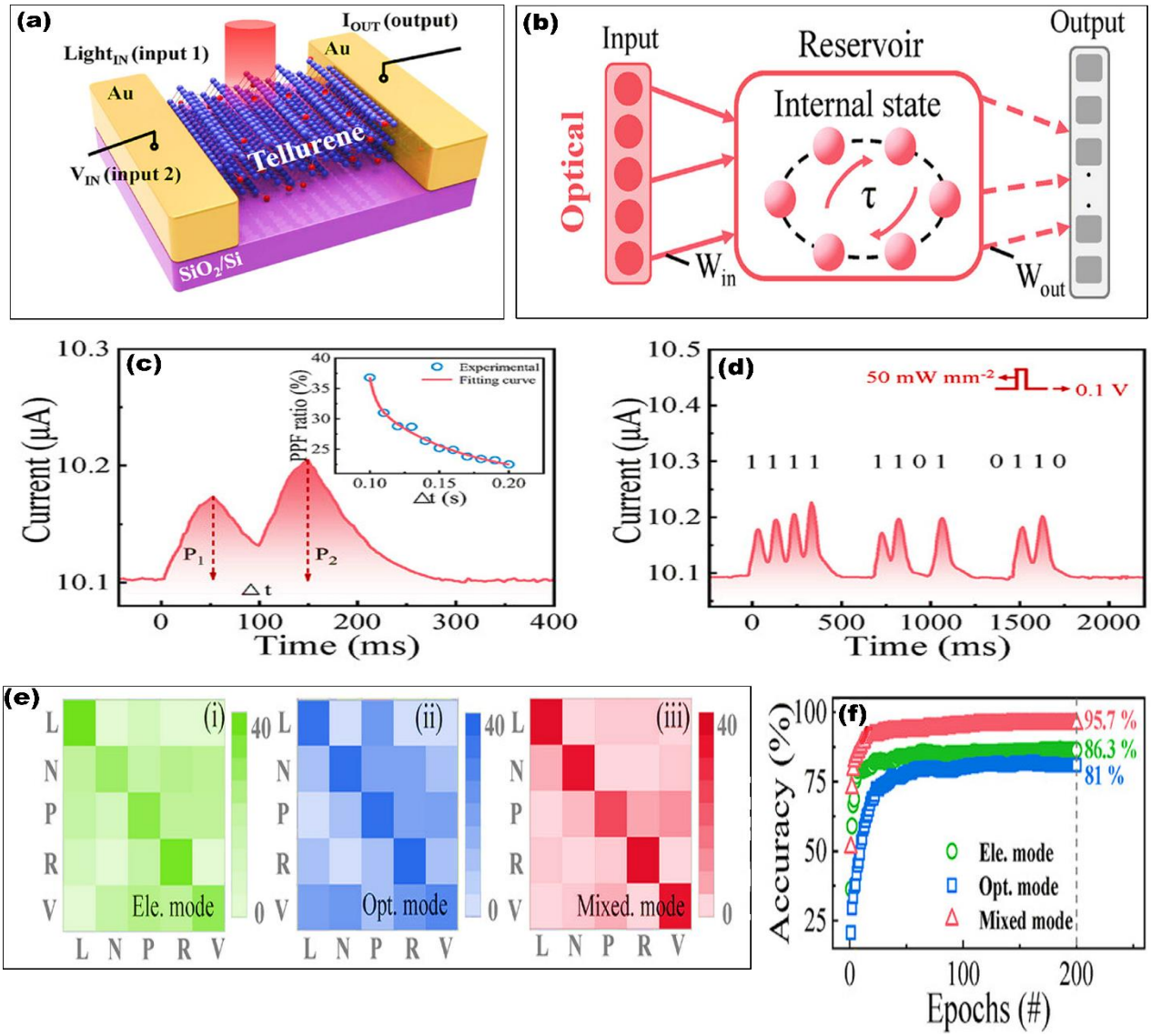

Fig. 17 (a) The schematic representation of tellurene-based optoelectronic memristor, (b) Schematics of the optical stimuli-based RC systems, (c) Current response under two optical pulses (wavelength = 1022 nm, intensity = 50 mW mm^{-2}, Pulse width = 50 ms). Inset: PPF index as a function of the inter pulse interval (*Δt*), (d) Current responses of device under optical stimuli to three typical pulse streams ([1111], [1101], and [0110]), (e) Confusion matrices for (i) electrical mode, (ii) optical mode, and (iii) mixed mode, and (f) Recognition accuracy of ECG patterns in electrical-input, optical-input, and mixed input modes. Reprinted with permission under a Creative Commons CC-BY license from Ref. [145], Copyright [2025] [Wiley].

TABLE I: Figure of merits of reported 2D materials-based memristive and memtransistor devices along with their applications.

Device Architecture TE-to-BE	**Device Type**	**Switching Type**	**Stimulus Type**	**ON/OFF ratio**	**Endurance**	**Recognition accuracy**	**Operating wavelength (nm); Optical Power Intensity (W cm^{-2})**	**Synaptic function**	**Applications**
Ag/SF@WS_2/ITO [120]	Memristive	Bipolar Switching	Optoelectronic	Not Reported	300	Not Reported	620 nm; 0, 4.6, 6.0, and 12.7 W/cm^2	STP, LTP, PPD	Autonomous driving and artificial vision systems.
Au/ReS_2/h-BN/Au [127]	Memristive	Bipolar Switching	Optoelectronic	13.8	Not Reported	89.4%	655 nm	Not Reported	Convolutional Neural Network
Al/TiS_3/ITO [42]	Memristive	Bipolar switching	Optoelectronic	~4×10^2	Not Reported	Not Reported	400 nm/530 nm/808 nm	Potentiation/depression, STDP	Neuromorphic chips
Ag/BiOI/Pt [44]	Memristive	Bipolar switching	Optoelectronic	10^5	50	80%	0 to 800 μW cm^{-2}	LTP and LTD, PPF, Learning experience	Neuromorphic computing and retina-like sensors
Cu/HfO_x/BP/Pt [46]	Memristive	Bipolar switching	Optoelectronic	10^2	10^4	90.16%	dark, 32, 48, 57, and 68 mW cm^{-2}	STP/STD/LTP/LTD/STM/ LTM/PPF	Artificial visual system
ITO/$(BA)_2PbI_4$/ITO [52]	Memristive	Bipolar switching	Optoelectronic	Not Reported	Not Reported	94.01%	450 nm-800 nm; 0.8 mW cm^{-2}, 2.4 mW cm^{-2}, 5.1 mW cm^{-2}	EPSC, PPF, STP to LTP transition, STDP, spike-intensity-dependent potentiation (SIDP)	Neuromorphic Vision Sensors
Al/Al_2O_3/MoS_2/Al_2O_3/ p^+Si [48]	Memristive	Bipolar switching	Optoelectronic		Electrically programmed /erased for 10^6 cycles. Optically programmed /erased for 1000 cycles for Wavelength: 600 nm, 550 nm, 500 nm,	91.03%	600 nm, 550 nm, 500 nm, 450 nm, 400 nm	Not Reported	Artificial visual system

					450 nm, 400 nm.				
ITO/ ZTO/In_2O_3/Pt [54]	Memristive	Bipolar switching	Optoelectronic	10^3	2000 cycle	95.8%	405 nm; 2.3 mW/cm^{-2}, 3.4 mW/cm^{-2}, 4.7 mW/cm^{-2}, 5.6 mW/cm^{-2}, and 6.4 mW/cm^{-2}	Potentiation/depression, PPF, STM to LTM transition, Learning-forgetting-relearning process	Human eye sensory perception and object tracking
Ag/CeO_2/MoS_2/ITO [56]	Memristive	Bipolar switching	Optoelectronic	Not Reported	Not Reported	Not Reported	620nm, 580 nm, 520 nm; 0.097, 0.367, 1.290, 3.538, 4.781, 6.282, 8.460, and 10.842 mW/cm^2	Potentiation/depression, PPF, PPD, STM to LTM transition, Learning-forgetting-relearning process	Human eye sensory perception and colour recognition
Au/tellurene/Au [145]	Memristive	Bipolar switching	Optoelectronic	Not Reported	Not Reported	81%	1022 nm, 50 mW mm^{-2}	EPSC, STP, PPF	Single- and multimodal sensory platform, neuromorphic computing
Au/WSe_2/WCL/h-BN/Au/SiO_2 [41]	Memtransistor	Not Reported	Optoelectronic	2.09 @ 532 nm	Not Reported	> 90%	655 nm, 532 nm, 405 nm; 6 mW mm^{-2}	EPSC, Potentiation/depression, STDP, LTP/LTD	Complex pattern recognition, Neural sensing
Ti/Au/MoS_2/h-BN/SiO_2 [45]	Memtransistor	Not Reported	Optoelectronic	Not Reported	Not Reported	96.1%	405 nm; 65 mW/cm^{-2} and 365 nm ; 2.1 mW/cm^{-2}	EPSC, LTP/LTD, PPF	Bio-signal pattern recognition
MoSSe/Al_2O_3/Li+ /Al_2O_3/ITO/PET [49]	Memtransistor	Not Reported	Optoelectronic	Not Reported	Not Reported	83.3%	400 nm- 600 nm; 0.041 mW/cm^{-2}, 0.061 mW/cm^{-2}	STP, STP to LTP transition, LTP/LTD, PPF, SNDP	Artificial retina perception system
Ni/Au/MoS_2/ Al_2O_3/ $PtTe_2$/p-Si [161]	Memtransistor	Not Reported	Optoelectronic	Not Reported	Not Reported	80%	300 nm, 450 nm, 1µm, 2 µm; 360 µW/cm^{-2}, 320 µW/cm^{-2}, 300 µW/cm^{-2}, 280 µW/cm^{-2}, 270 µW/cm^{-2}, 250 µW/cm^{-2}	STP/LTP, STP to LTP transition, SIDP	Mixed-color pattern recognition
Au/MoS_2/SiO_2 [51]	Memtransistor	Not Reported	Optoelectronic	Not Reported	Not Reported	Not Reported	466 nm; 245 µW/cm^{-2}	EPSC, STM to LTM transition, PPF	Neuromorphic computing applications

Ni/Au/Al_2O_3/MoS_2/$PtTe_2$/ SiO_2/p-Si [53]	Memtransistor	Not Reported	Optoelectronic	Not Reported	Not Reported	Not Reported	300 nm, 450 nm, 1µm, 2 µm	Potentiation and depression, the relearning process	In-sensor image preprocessing
Cr/Au/WS_2/MoS_2/SiO_2/ Si [57]	Memtransistor	Bipolar switching	Optoelectronic	Not Reported	400 cycles	Not Reported	400 nm, 500 nm, 600 nm; 0.3 mW/cm-^{2}, 0.66 mW/cm-^{2}, 0.98 mW/cm-^{2}	EPSC/IPSC, PPF, LTP/LTD, learning, forgetting, and relearning process, SRDP	Visual neuromorphic application
Ti/Au/ MoS_2/$TaNiS_2$/SiO_2/Si [55]	Memtransistor	Not Reported	Optoelectronic	Not Reported	Not Reported	91.52%	532 nm; 0-50 mW/cm^{-2}	EPSC/IPSC, PPF/PPD, LTP/LTD, STM to LTM transition	Artificial vision systems.
Au/Na^+@WS_2/P^+-SiO_2 [172]	Memtransistor	Bipolar switching	Optoelectronic	Not Reported	Not Reported	93.3%	405 nm; 4.63 mW/cm^{-2}, 2.48 mW/cm^{-2}, 1.09 mW/cm^{-2}, 0.19 mW/cm^{-2}	PSC, STDP, PPF, SNDP, SDDP, SRDP	Controlled neuromorphic computing
Au/MoS_2/P^+Si/SiO_2 [173]	Memtransistor	Bipolar switching	Optoelectronic	10^5	Not Reported	95.7 %	400 nm; 1.58 mW/cm^{-2}	EPSC, PPF, STP, LTP	neuromorphic computing

2D Materials-based Memtransistor

Memtransistor is a three-terminal device that upholds the memory resistance properties of a memristive device along with the switching characteristics [146-148]. Memtransistors have important advantages over the memristive device, including a lack of electroforming process, tunable memory function with a high ON/OFF ratio, high mobility (0.6 cm^2/Vs) [149], and a lack of sneak path in the crossbar array [150]. The channel conductance can be modulated by applying different voltages to the gate electrode. Depending on the modulation mechanism, three-terminal transistors can be divided as: floating gate field effect transistors (FGFETs), optoelectronic field effect transistors (OFETs), ferroelectric field effect transistors (FeFETs), and electromechanical coupling field effect transistors (MFETs) [151-154]. Among them, OFETs enable the synergistic processing of both electrical and optical signals, which can be used to realize artificial vision systems. Optoelectronic synapses showed good parallelism to emulate functions of retinal neurons with high energy efficiency [155-158].

Recently, Oh *et al*. [45] reported a MoS_2/hexagonal boron nitride (h-BN) heterojunction three-terminal transistor-based photoelectroactive synapse wherein the synaptic weight can be modulated by using optical spikes. The weight update phenomenon physically commences from the ionization and neutralization of inherent defects present in the h-BN by applying an optical pulse under negative and positive gate biasing, respectively, as shown in **Fig. 18(a)**. **Fig. 18(b)** depicts the band gap modulation wherein the channel conductance was observed to be increased or decreased due to ionization and neutralization, respectively, and emulating the LTP and LTD synaptic functionalities. The enhancement in the neutralization process with higher photon energy revealed that the threshold voltage (V_{th}) can be modulated by the light wavelength (see **Fig. 18(c-d)**). The C2C variations in V_{th} values were examined using an optical pulse under different values of V_{write} (+30, -10, -20, and -30 V). The obtained outcomes showed that the four V_{th} values presented similar values in all cycles, and the relative standard deviation (RSD) was reduced from 8.6% to 0.4% for +30 V and -30 V, respectively, as shown in **Fig. 18(e)**.

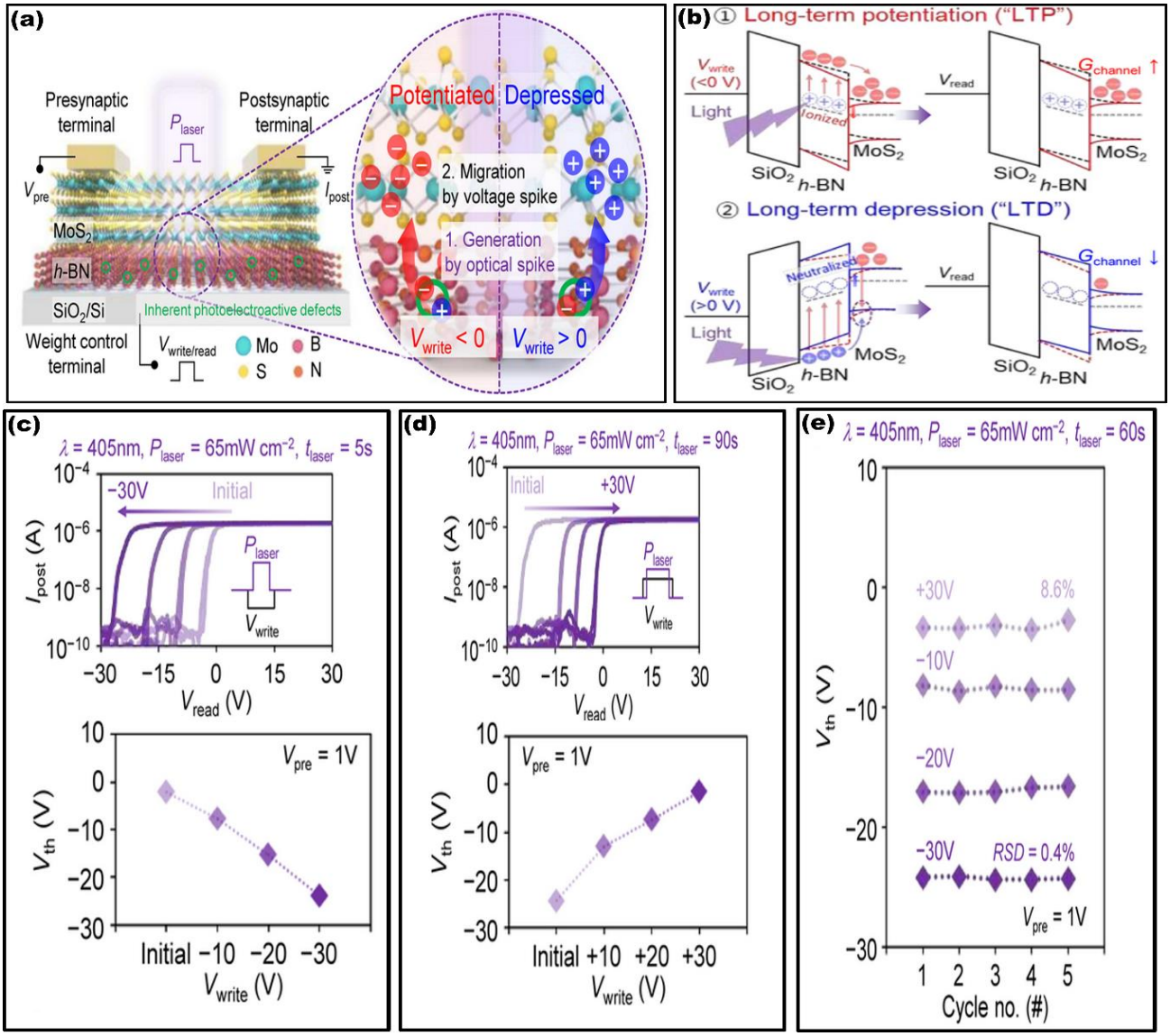

Fig. 18. (a) Schematic illustration of device structure and bidirectional weight operation process, (b) Energy band diagrams indicating weight-updating principles of long-term potentiation and depression (LTP/D), Multistate memory characteristics of vdW photoelectroactive synapse wherein, (c) Negative threshold voltage (V_{th}) shift characteristics controlled by optical spikes under negative voltage bias, (d) Positive V_{th} shift characteristics controlled by optical spikes under positive voltage bias, and (e) Cycle-to-cycle variations in V_{th} with the optical spikes under various V_{write} values. Reprinted with permission under a Creative Commons CC-BY license from Ref. [45] Copyright [2021] [Springer Nature].

Furthermore, the V_{th} value obtained by the co-stimulus of the electrical (- 30 V) and optical (405 nm, 65 mWcm^{-2}, and 5 s) spikes persisted even after 21 days with an RSD of 1.3% (see **Fig. 19(a)**). The change in the channel conductance (G) corresponding to 10 optical spikes of 365 nm 2.1 mWcm^{-2}, and 0.2 s, along with an electrical spike of -16 V, was further analyzed to investigate synaptic dynamics (see **Fig. 19(b-c)**). The result validates the gradual increment (0.03 to 13.1 nS) and rapid decrement (~1.1 nS) in channel conductance. However, its value is maintained even after 400 s, which can be explained by two reasons. First, the photogenerated charge carriers in the MoS_2 layer disappeared rapidly, while in the second case, the positive ionized defect in the h-BN layer that maintained for a

longer time [159-160]. The PPF ratio is also observed to decrease from 239% to 82% as the pulse interval increases from 0.5 s to 5 s. The pattern recognition was conducted using MNIST digit patterns using the platform "MLP+NeuroSim ver. 1.0", and the maximum accuracy achieved was 91.1% for 100 pulses (see **Fig. 19(d-f)**). However, some challenges warrant attention, including the large-scale growth of 2D materials and direct growth on the surface of 2D materials to form a heterojunction. Recently, some pioneering work has been reported on different methods for the large-scale growth of 2D materials, such as wafer-scale transferring, wafer-scale chemical vapor deposition (CVD) growth, and direct epitaxial growth [161-166]. Moreover, it is necessary to summarize and critically assess further technological advances like doping and contact engineering. The core operation of the device relies on the ionisation and neutralization of the inherent defects. However, variability in defect types and densities could impact the device reproducibility and long-term stability across a large area. In addition, the electrical and optical stimuli used 0.2 s durations and voltages up to -16 V. The variability in the conductance states and synaptic weight linearity across the devices should be explicitly quantified for reliable operation in the neural network. The high operational voltage and relatively long pulse duration limit the potential for high-speed low-energy neuromorphic operations.

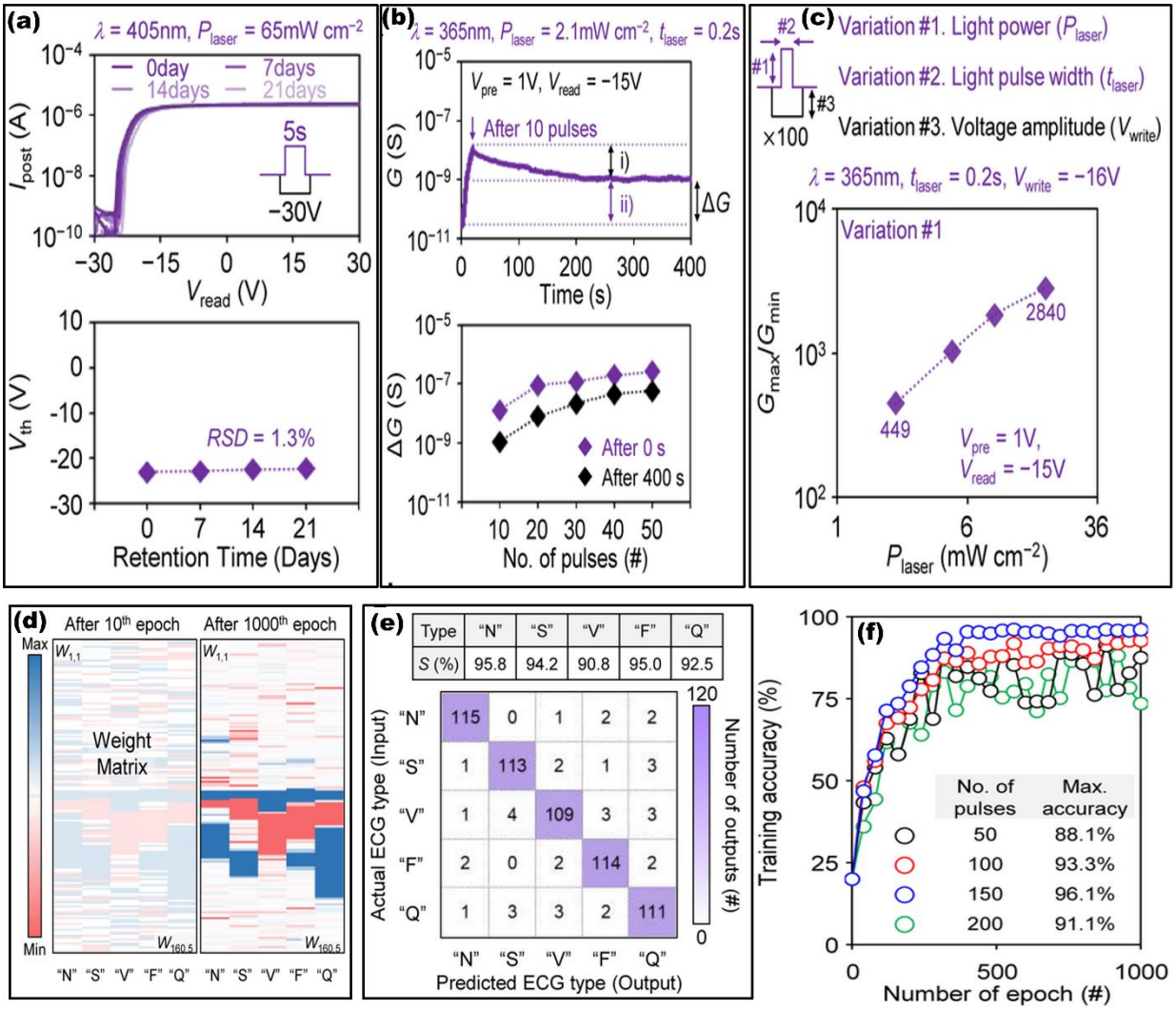

Fig. 19. (a) Retention characteristics of the modulated V_{th}, Dynamic characteristics of vdW photoelectroactive synapse, (b) Conductance (G) response decaying characteristic (upper panel) and retained conductance difference (ΔG) immediately after application of the co-stimuli and after 400 s (lower panel), (c) Dynamic range of conductance (G_{max}/G_{min}) concerning light power, (d) Mapping images of 800 synaptic weights after 10^{th} and 1000^{th} epochs, (e) Confusion matrix of heartbeat type classification for 600 test datasets, and (f) Training accuracy as a function of the number of training epochs according to the number of pulses. Reprinted with permission under a Creative Commons CC-BY license from Ref. [45] Copyright [2021] [Springer Nature].

Meng *et al*. [49] proposed a 2D Janus Molybdenum Sulfide Selenide (MoSSe)-based artificial retina to emulate the functionality of visual perception by electronic/ion and optical co-stimuli. The device comprises a flexible polyethylene terephthalate (PET)/ITO substrate, 2D MoSSe as a channel, and the stack of $Al_2O_3/Li^+/Al_2O_3$ acting as the dielectric, shown in **Fig. 20(a)**. Upon applying the negative voltage to the ITO gate electrode, Li^+ ions accumulated at the lithium perchlorate ($LiClO_4$)/Al_2O_3 interface, and perchlorate anions (ClO_4^-) accumulated in the ionic layer at $Al_2O_3/LiClO_4$ due to electric double layer (EDL) electrostatic effects. This phenomenon promotes the accumulation of positive charge carriers at the interface of $Al_2O_3/LiClO_4$, and the negative charge moves toward the MoSSe/Al_2O_3 interface, which subsequently reduces the channel current. The reverse phenomenon happens under positive electrical stimuli, resulting in an enhancement in channel current (see **Fig. 20(b-c)**). The excitatory postsynaptic current (EPSC) with a single electric pulse (3 V, 500 ms) was observed to be ~2.0 nA, which gradually decreased to ~0.28 nA and was maintained for 100 s,

signifying STM characteristics (see **Fig. 20(d-e)**). Furthermore, 25 successive negative voltage pulses were applied to realize the learning-forgetting-relearning process shown in **Fig. 20(f)**. At the first learning stage, the PSC was found to decrease from 1.73 nA to 0.692 nA, and later the current increased to 1.60 nA in 100s after removing the electrical stimuli (forgetting process). Notably, in the second learning process, 20 voltage pulses were enough to generate 0.682 nA PSC, resembling the re-learning process in the human brain.

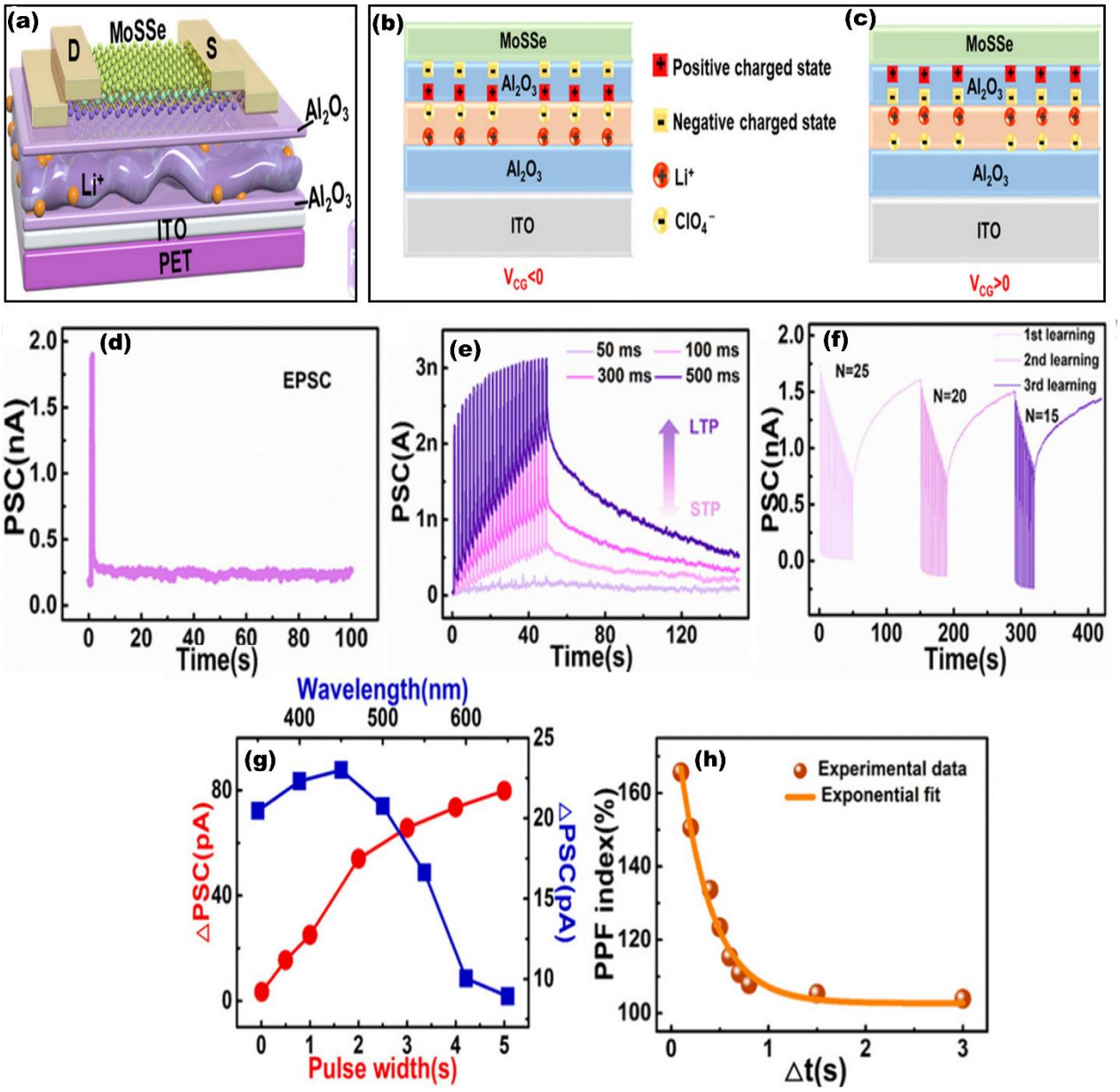

Fig. 20. (a) Design of 2D Janus MoSSe-based electronic device, Electrical characteristics of the artificial retina with the schematic mechanism and charge distribution under (b) negative and (c) positive gate voltage, (d) EPSC response to a single voltage pulse (3 V, 500 ms), (e) Transition from STP to LTP through increase of the voltage pulse width from 50 to 500 ms, (f) Realization of learning-forgetting-relearning with the artificial retina, (g) Postsynaptic current change of the device under different optical pulse widths and wavelengths, and (h) PPF index with optical stimuli. Reproduced or adapted with permission from Ref. [49] Copyright [2022] [American Chemical Society].

The capability of sensing optical stimuli and storing the incident pulse information was also investigated under different pulse intensities and pulse widths. The optical stimuli promote the generation of photoexcited charge carriers in the MoSSe channel, which stimulate the Li^+ to depart

from the ionic layer and approach the $Al_2O_3/LiClO_4$, resulting in diminishing the oxide thickness and consequently enhancing the channel current. The maximum synaptic weight was achieved at the wavelength of 450 nm, while the augmentation in ΔPSC was observed as the pulse width broadened from 10 ms to 5 s (see **Fig. 20(g)**). The PPF was also reported to be decreased from 166 % to 104 % as the pulse width increased from 100 ms to 3 s (see **Fig. 20(h)**).

The light intensity adaptation through self-regulation in the visual system is also realized under mild and dazzling illumination. Upon the mild illumination of 450 nm with a power of 0.040 mW/cm^2 for 1s, a threshold value of 1.3 nA; however, the eye does not have any discomfort (see **Fig. 21(a)**). As the intensity enhanced to 0.061 mW/cm^2, the current reached 1.44 nA, which was higher than the threshold value (see **Fig. 21(b)**). The dazzling illumination can be controlled and regulated by the biological eye by adjusting the pupil size. Similar behavior can be realized by applying a negative pulse voltage (-1 V), resulting in a fall of current below the threshold value (see **Fig. 21(c)**). An ANN system was constructed for image recognition with 100 input layers, 64 hidden layers, and 10 output layers. The recognition rate of 83.3% was achieved after 1,000 training epochs with preprocessing of the artificial retina system (ARS), whereas without image preprocessing, the recognition rate reduced to 77.6% (see **Fig. 21(d-h)**). Such characteristics revealed that image preprocessing can be achieved by the integration of ARS with a MoSSe-based device, which can also further enhance the image recognition rate and efficiency. The device demonstrated the spectral response well around 450 nm; however, the spectral sensitivity, particularly into the infrared region, remains limited. This restricts the applicability of the device in the multispectral sensitivity. For light adaptation by modulating current in response to varying optical intensities, the operation threshold (~1.3 nA at 450 nm, 0.06 mW/cm^2) is relatively high compared to the sensitivity of biological photoreceptors. The recognition rate of 83.3% was achieved after 1,000 training epochs with preprocessing is too low for advanced neuromorphic vision systems and image recognition applications. Also, the flexibility was demonstrated on a small scale, and the bending stability under different environmental challenges, such as temperature variation and electrical fatigue, needed further investigation.

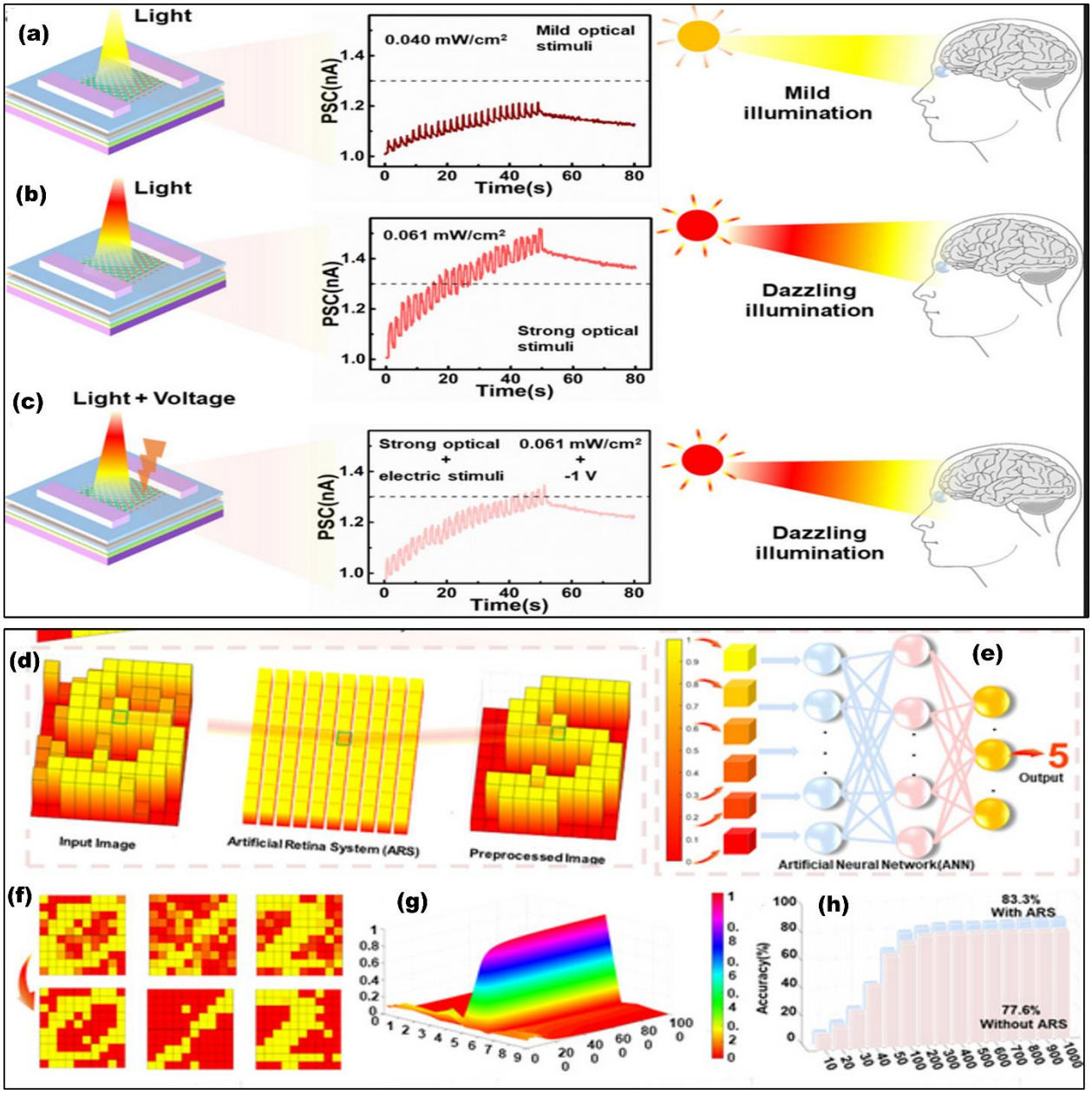

Fig. 21. Simulation of light adaptation of human visual system wherein, (a) The mild light illumination (0.040 $mWcm^{-2}$) could not induce injury of human eyes, corresponding to the current that is lower than the threshold (<1.3 nA), (b) Under excessively powerful optical intensity (0.061 $mWcm^{-2}$), the current could increase higher than the threshold (>1.3 nA), which mimics the injury of biological eyes exposed to harsh light, (c) The artificial retina could adapt to the strong light intensity through the modulation of negative voltage pulses (-1 V), and the current fell below the threshold (<1.3 nA), (d) Artificial retina system (ARS) with an array employing 100 (10×10) cells to realize the pretreatment, (e) Artificial neuromorphic (ANN) system with input layer (100), hidden layer (64), and output layer (10) was constructed to realize image recognition, (f) The filtering capability of the ARS, all of the digits of "0", "1", "2" revealed highlighted body features and smoothed background noises after the preprocessing by ARS, (g) Efficient recognition of number "5" with preprocessing by ANN, and (h) Recognition rate of the artificial visual system with and without ARS, which exhibits an improvement in the recognition rate and efficiency after the pretreatment of ARS. Reproduced or adapted with permission from Ref. [49] Copyright [2022] [American Chemical Society].

Furthermore, Islam *et al*. [161] demonstrated a multiwavelength optoelectronic synapse for real-time object identification and pattern recognition. **Fig. 22 (a)** shows the proposed device, which employs

monolayer MoS_2 as an active channel, Al_2O_3 is used as the back gate dielectric, and p-Si/platinum ditelluride ($PtTe_2$) acts as a gate electrode. Here, MoS_2 is used as a UV-visible sensitive material, and p-Si/$PtTe_2$ is employed to respond during infrared (IR) wavelength to realize the functionality of multiwavelength optoelectronic synapses. The optical image of the chip (bottom panel) and optical microscope image (top panel) of a single optoelectronic synapse device are shown in **Fig. 22(b)**. The light absorption was measured under a different wavelength ranging from 300 nm to 2.0 μm with a constant intensity of 400 μW/cm^2. A negative shift in the threshold voltage (V_{th}) was observed with the different wavelengths, and a maximum shift was achieved at 450 nm, which was attributed to the maximum absorption by the monolayer MoS_2 (see **Fig. 22(c)**). The contribution of $PtTe_2$ in the V_{th} shift was also investigated, and the result revealed that $PtTe_2$ contributed a significant shift in the infrared region; however, a higher shift was observed in the UV-visible region compared to the control device without $PtTe_2$ (see **Fig. 22(d-e)**). The memory window was observed to be increased from 0.27 to 3.92 V as the V_G sweep range increased from ±1 to ±5 V (see **Fig. 22(f)**). The trapping and de-trapping of holes at the MoS_2/Al_2O_3 interface enable the shifting of V_{th} to more negative and positive V_G, respectively. The light intensity-dependent responsivity was measured with the application of 10 light pulses of 50 ms pulse width, wherein the intensity ranged from 220 μW/cm^2 to 350 μW/cm^2. The transition from STP to LTP was observed with increasing light intensity (see **Fig. 22(g-h)**).

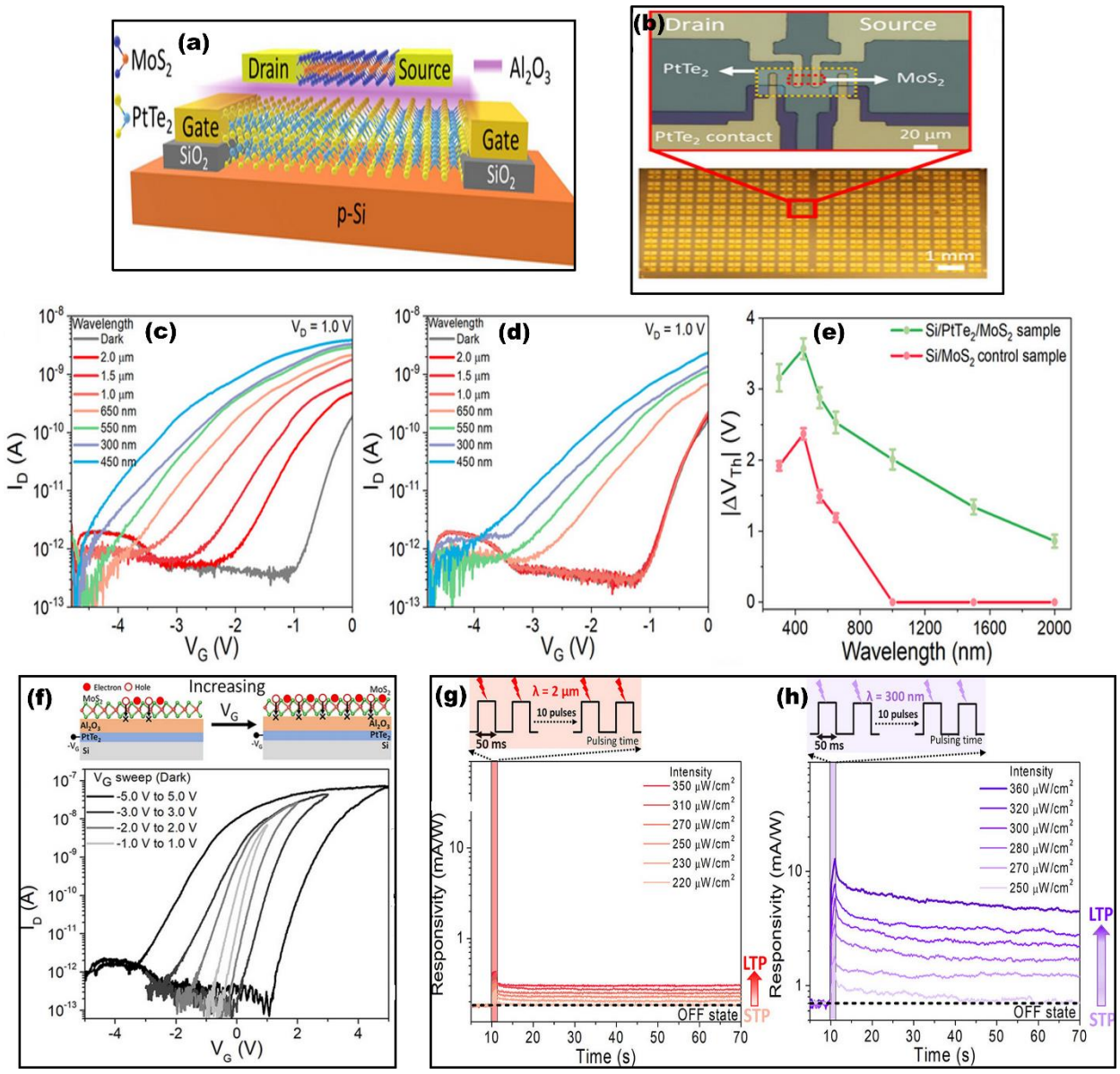

Fig. 22. (a) Schematic diagram of the multiwavelength optoelectronic synapse, and (b), (c) I_D-V_G characteristics showing the shift in threshold voltage with the application of light of wavelengths from 300 nm to 2 μm of Si/$PtTe_2$/Al_2O_3/MoS_2 device and (d) Si/Al_2O_3/MoS_2 device at a constant V_D of 1.0 V, (e) Comparison of $|\Delta V_{Th}|$ as a function of light wavelength for Si/$PtTe_2$/Al_2O_3/MoS_2 device and Si/Al_2O_3/MoS_2 device, (f) Increase in device hysteresis with higher negative V_G sweep. Gate-tunable potentiation and conductance retention at a constant V_D of 1.0 V with the application of light of wavelengths (g) 2.0 μm and (h) 300 nm with 10 pulses of 50 ms pulse width. Reproduced or adapted with permission from Ref. [161] Copyright [2022] [American Chemical Society].

Furthermore, the device achieved larger responsivity, with slow decay trends observed when the number of applied pulses increased from 100 to 1,000. The retention of 500 s was reported for seven different conducting states for different wavelengths, signifying that the device can successfully emulate the optoelectronic analog memory for wavelengths ranging from UV (300 nm) to IR (2 μm) (see **Fig. 23(a)**). The C2C weight update variation for all four wavelengths showed low variability along with high stability across 10 cycles. Following the weight update, an ANN was developed to train and identify both single and mixed wavelength patterns. Here, the test was conducted for three

mixed patterns, viz., 3 in 8, 1 in 7, and 1 in 4. The MNIST data set was used for training and testing the neural network. The recognition accuracy for single color digit "3' in '8" patterns was reported at ~80% after 1,000 epochs, while it maintained its performance for mixed color digit recognition (see **Fig. 23(b-e)**). These findings lay the groundwork for designing and developing multiwavelength neuromorphic visual perception systems for pattern recognition. In this work, a semimetal with a narrow bandgap resulted in relatively high dark current and low-energy efficiency. Also, the performance parameters are limited for long-term stability as well as performance under ambient conditions. The C2C validation is limited to only 10 cycles, which is insufficient for long-term endurance and stability. The result demonstrated the performance under the tested wavelength. However, the optical response speed and the frequency bandwidth of the synaptic behavior require an extensive analysis. The reported ANN recognition accuracy (~80%) is far below the practical usability for complex image recognition.

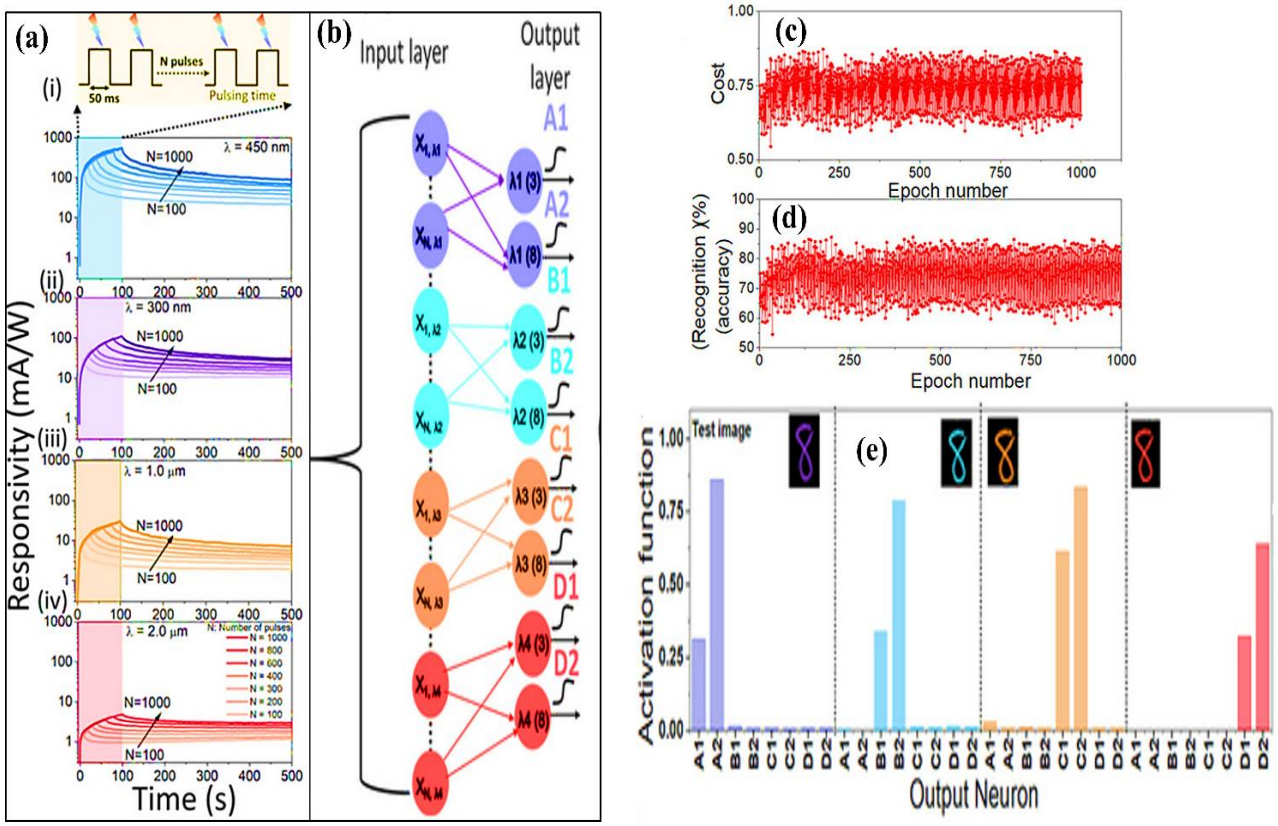

Fig. 23. (a) Long-term potentiation and memory retention with the application of light of 50 ms pulse width with wavelengths (i) 450 nm, (ii) 300 nm, (iii) 1.0 μm, and (iv) 2.0 μm at a constant V_G of -400 mV and V_D of 1.0 V with increasing pulse number from 100 to 1000, (b) Single layer neural network schematic, (c) Cost function as a function of number of training epochs for all the test cases, (d) Recognition rate as a function of number of training epochs, (e) Activation values of each neuron for single wavelength images. High activation values are observed for '3' and '8' neurons, indicative of the presence of these patterns in digit '8' for four different wavelengths. Insets show test images and (f) Activation values for mixed wavelength patterns. High activation values for three neurons are observed, corresponding to the wavelengths of inside and complement digits. Reproduced or adapted with permission from Ref. [161] Copyright [2022] [American Chemical Society].

This work is further extended by Sahu *et al*. [51], exploring the PPC effect on 2D-based MoS_2 and its potential to emulate complex learning behavior with integrated reconfigurable logic and arithmetic operations (see **Fig. 24(a)**. The proposed device demonstrates photo-responsivity from the UV to visible, suggesting a wide range of tunability in synaptic weight. A rapid increment in drain current (~143 nA) was observed upon applying an optical pulse of 466 nm wavelength with a power of 245 $\mu W/cm^{-2}$ (see **Fig. 24 (b)**). Following this, a gradual decay is observed after the removal of optical stimuli, signifying synaptic behavior. The PPC originated in MoS_2 due to the inherent trap states.

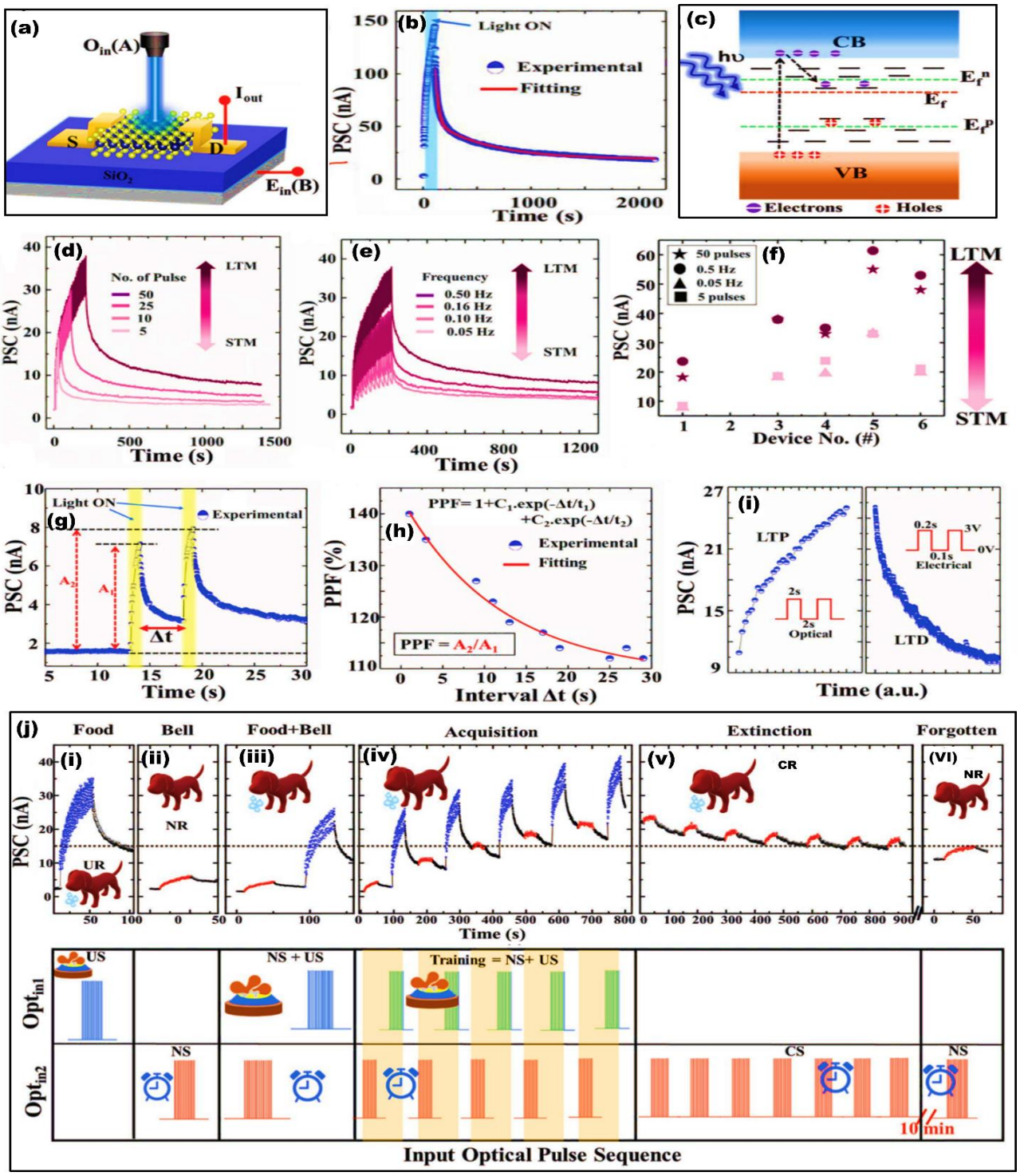

Fig. 24 (a) Device structure of proposed MoS_2 artificial synapse, (b) Transient current measured at reading voltage V_d = 1 V and V_g = 0 V, with response to the blue optical stimulus of power (P) 245 μWcm^{-2} for 100 s, (c) Band model of MoS_2

under optical illumination. Herein, the red dotted line represents the Fermi energy, and the green dotted line represents the quasi-Fermi level for electrons and holes. Complex neurological behavior of MoS_2 artificial synapse, (d) Transient PSC measured at V_d = 1 V, V_g = 0 V by illuminating multiple blue optical pulses having PW = 1 s and P = 245 μWcm^{-2}, (e) Transient PSC for varying frequencies of blue optical pulses. The frequency is varied by increasing the OFF time of the optical pulse, keeping the ON time fixed, (f) Maximum PSC of several devices under the extreme values of optical pulse number and frequency, (g) PSC under two optical pulse stimulations, (h) Typical pulse paired facilitation (PPF) index variation with change in the time interval (Δt) between two pairs of the optical pulse, (i) The left panel shows the LTP, that is, the increase in PSC under stimulation of thirty-five identical optical pulses. The right panel shows the LTD, that is, the decrease in PSC under identical electrical gate pulses, and (j) Demonstration of Pavlov's classical conditioning using MoS_2 artificial synapse. The upper panel shows the output current (PSC) measured at V_d = 1 V and V_g = 0 V, and the lower panel shows the input optical spikes Opt_{in1} and Opt_{in2}. The black dotted line is the threshold current (15 nA) for salivation (i) PSC for 20 consecutive blue optical input spikes of PW = 1 s, P = 245 μWcm^{-2} (US), (ii) PSC for 20 consecutive red optical spikes of PW = 1 s, P = 108 μWcm^{-2} (NS), (iii) PSC for a single training set, where each training set contains 20 red spikes followed by 20 blue spikes, (iv) PSC for Five consecutive training sets. The training sets are highlighted in cyan color, (v) PSC for repeated NS without the US, and (vi) PSC for a single NS showing the forgetting process. Reproduced or adapted with permission from Ref. [51] Copyright [2023] [Wiley].

The photogenerated charge carriers are being trapped in these trap states, resulting in a rise to quasi-Fermi levels E_{fn} and E_{fp}, respectively. The variation in potential energy induced by these trapped charge carriers, resulting in the delay in recombination, leads to the PPC (see **Fig. 24 (c)**). The influence of optical pulse intensity, illumination time, and frequency on the PSC is investigated with the read voltage of V_d =1 V with zero gate bias (see **Fig. 24 (d-f)**). The maximum synaptic change was observed at higher energetic blue pulses, which can be explained by the dependency of PPC on the intensity and illumination time. From the STM/LTM front, the lower potentiation was observed with 5 pulses together with 0.05 Hz frequency, signifying STM. The STM to LTM transition was achieved with 50 pulses along with a 0.5 Hz frequency, which prompted the large potentiation. After potentiation, the decay time was observed to increase with the increase in the number of pulses and frequency. **Fig. 24 (g)** depicts that the PPF is calculated by applying an optical power of 245 μW cm^{-2} for 2s, and associative PSC is measured at a read voltage of 1V at zero gate voltage. The PPF is found to be decreased from 140 % and 112 % for the time intervals of 1 s and 29 s, respectively (see **Fig. 24(h)**). The LTD was achieved with the electrical spike of +3 V with a pulse width of 0.2 s, and the PSC was measured with V_d of 1 V at zero gate bias (see **Fig. 24(i)**). The PSC was observed to be decreased from 25 nA to 10.5 nA with the increase in the number of pulses, emulating biological LTD function. Furthermore, this work demonstrated that Pavlov's experiment under different optical stimuli and the broadband sensitivity of the device can be realized to mimic classical conditioning for associative learning of the biological brain (see **Fig. 24(j)**). The long decay (τ_2 ~ 356 s) and low on/off ratio (~ 42) that enabled the memory limits the real-time vision, as a result, the image-sensor grade detectivity hinders the performance. The weight drifts, device variability, C2C variation, and the training-relevant linearity in the neuromorphic array need further extensive quantification. Key system

matrix for, such as energy per optical spike, write/erase energy, cumulative endurance, and latency per update, are still needed to address for optimization of synaptic device performance.

In general, image processing involves low-level preprocessing like denoising at the sensor end, which typically requires operations such as Gaussian smoothing, median filtering for salt and pepper noise, wavelet denoising, and deep learning-based denoising [167-170]. This required additional circuitry in the back pane of the display or energy-intensive cloud communications [171]. However, the human brain exploits previous experience to understand the information, enabling it to filter out noise signals and selectively process visual data [55]. Even though the brain receives a huge amount of visual information from the peripheral environment, the visual perception typically focuses on a particular object, while the other stimuli are ultimately overlooked. This is the inherent capability of the human brain to "self-denoise" the information, which is expected to be a crucial property of artificial visual systems.

Inspired by this, Islam *et al*. [53] demonstrated the "Self-denoising" capability of 2D materials in optoelectronic synaptic arrays. The self-denoising can be realized when the conductance state corresponding to LTP is higher than the conductance state corresponding to STP. The longer exposure time is an effective approach to remembering the pattern for a longer time. For instance, if a noisy pixel imposes on the array for a short time duration, the stimulus corresponding to the noise is weaker compared to the stimulus corresponding to the training process. During the scanning of noisy pixels, the pattern pixel undergoes second-level learning while the noise pixel experiences its first-level learning. The re-learning process of pattern pixels further increases the conductance level (see **Fig. 25(a)**).

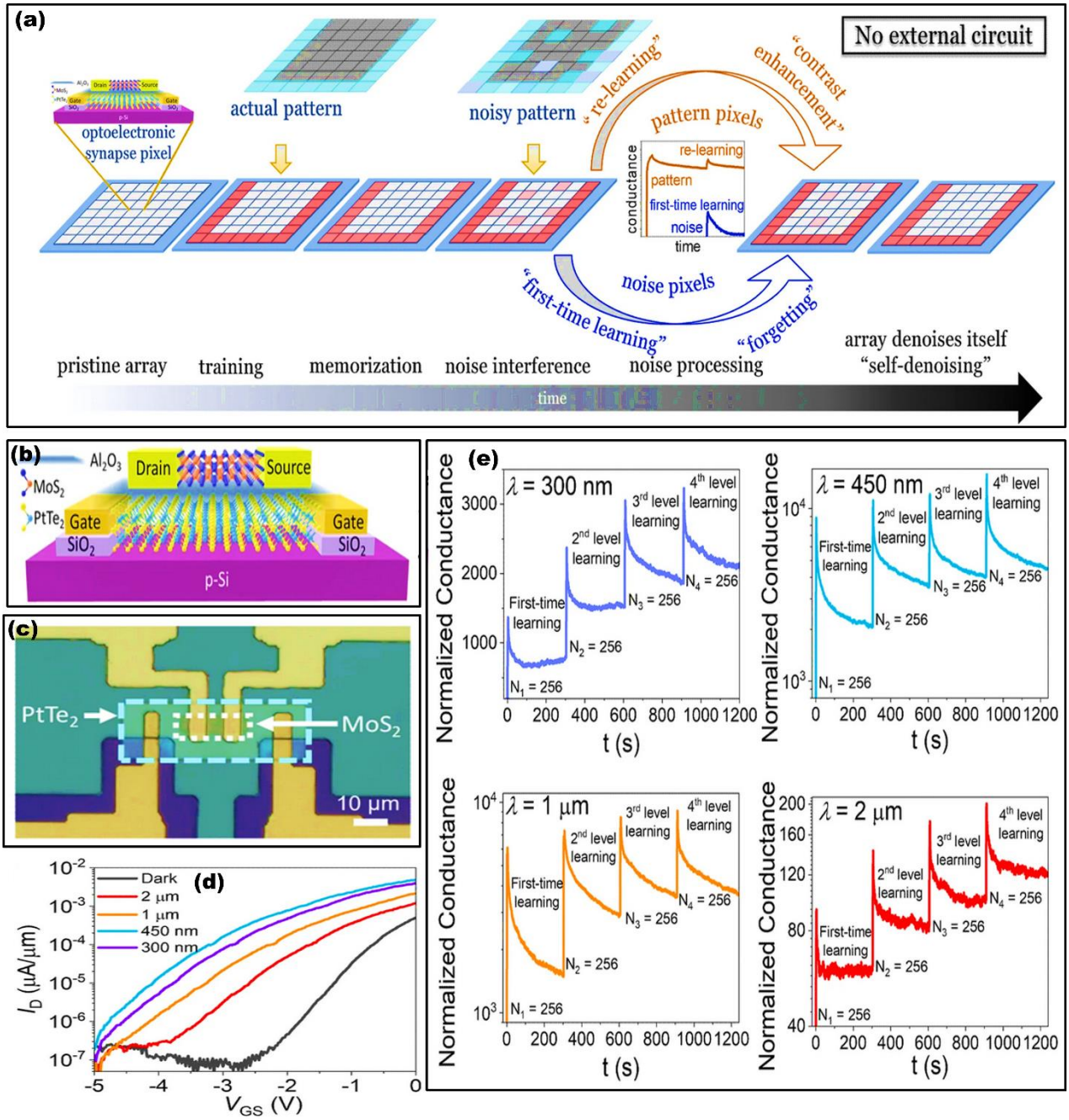

Fig. 25. Concept of "self-denoising" of an optoelectronic synapse array, (a) Cartoon of the concept of "self-denoising" process of an optoelectronic synapse array, where the pattern pixels, which are already trained undergo "relearning" process, while the noise pixels experience "first-time learning" resulting in fading of noise by contrast without involving any external circuitry, (b) Schematic and (c) optical microscope image of a 2D materials-based optoelectronic synapse device consisting of MoS_2 as the channel and p-Si/$PtTe_2$ as the buried gate electrode, (d) Transfer characteristics, I_D-V_{GS} of the device in dark and under four wavelengths: 300 nm, 450 nm, 1 μm and 2 μm, showing broadband response and distinct threshold shift for each wavelength, and (e) Optical potentiation of the device by applying four bursts of 256 pulses of pulse width 5 ms (effective illumination time = 1.28 s) and optical wavelengths of 300 nm, 450 nm, 1.0 μm and 2.0 μm with memory retention recorded for 300 s after application of each burst of pulses. For all wavelengths, memory gets stronger at each "relearning" level (2nd level learning and onwards). The final memory (conductance) of the devices after four-level learning is more than twice that of "first time (first-level) learning", which ensures the capability of the device to sufficiently demonstrate a "self-denoising" process. Reprinted with permission under a Creative Commons CC-BY license from Ref. [53] Copyright [2021] [Springer Nature].

In contrast, noise pixels exposed to less time retain low conductance levels and fade away with time. The (7×7) array is designed to achieve this functionality, wherein MoS_2 is employed as a channel, Al_2O_3 as the back gate dielectric, and p-Si/$PtTe_2$ as a gate electrode (see **Fig. 25(b-c)**). The device was illuminated under different wavelengths (300 nm, 450 nm, 1.0 μm, 2.0 μm) with the intensity of 400 μWcm^{-2} (see **Fig. 25(d)**). The device was consecutively potentiated four times with a burst of 256 optical pulses with an effective exposure time of 1.28 s. Each burst of optical pulse with a different wavelength leads to enhancement of the conductance state referred to as first-level learning, second-level learning, and so on (see **Fig. 25(e)**). The self-denoising mechanism for all the wavelengths was demonstrated by applying 1024 optical pulses having a pulse width of 5 ms to train and memorize the pattern "U". The "U" pattern was then exposed to Gaussian noise having standard deviations $\sigma = 0.3$ (see **Fig. 26(a-d)**). The intensity of optical pulses is normalized to 400 $\mu Wcm^{-2,}$ and the conductance of each device was measured after 0 s, 10 s, 30 s, and 60 s.

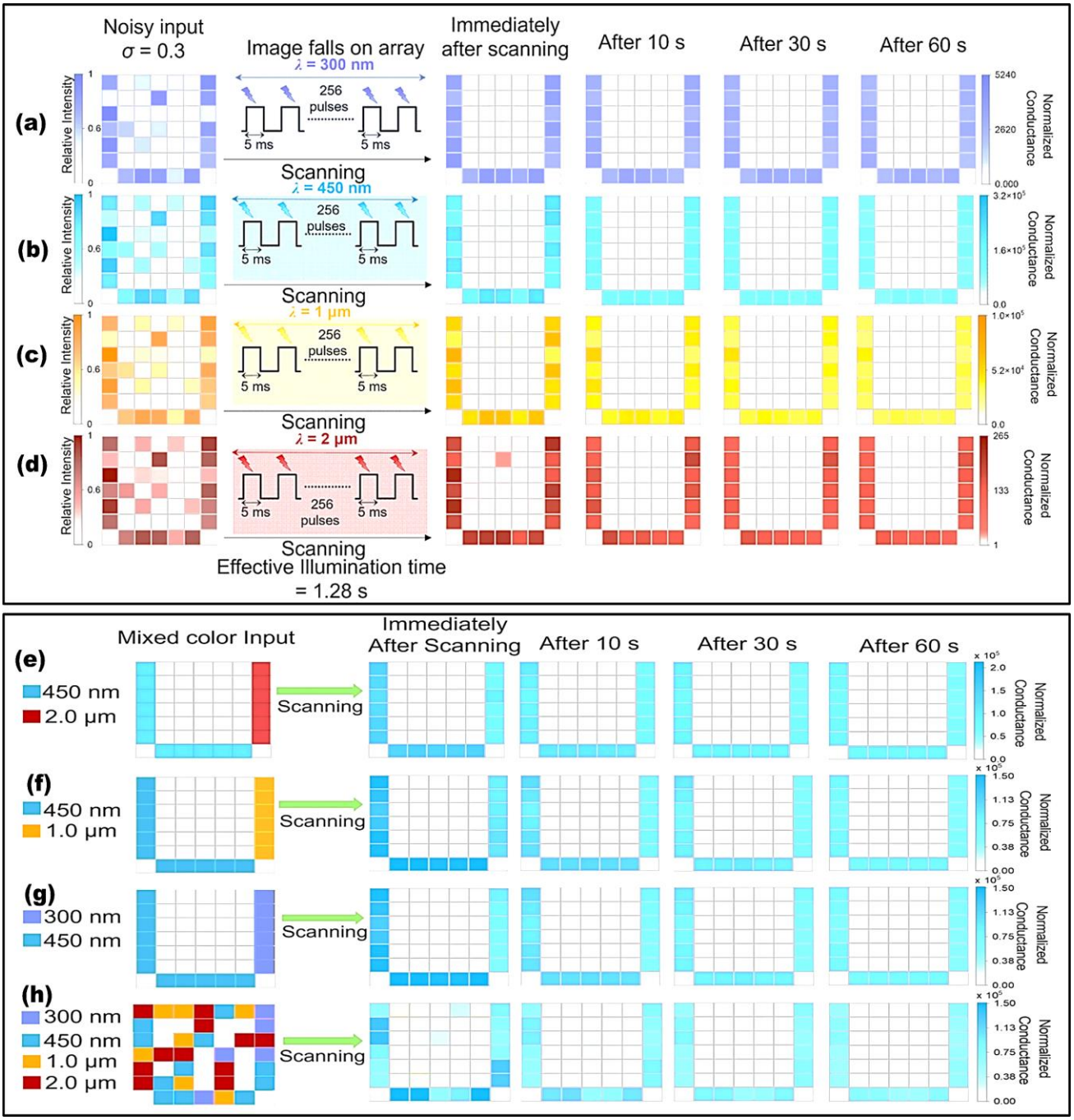

Fig. 26. (a-d) shows the input noise pattern and photoconductance retention for "U" input with Gaussian noise of σ = 0.3. For all wavelengths and both noise levels, the array is capable of denoising itself within 10 s (maximum), even for the noise pixels having intensity comparable to pattern intensity, e.g. $(2,4)^{th}$ pixel of the noisy image with σ = 0.3 (a-d) has 100% of the pattern intensity, still, the array can appreciably eliminate the noise within 10 s for all wavelengths. Conductance values up to 60 s depict no memory degradation during this "self-denoising" process. "Self-denoising" with mixed-color input. Heatmap plot of the normalized conductance levels of the array, as the trained array is "scanned" (allowing the input image to shine the device or reading the image) with a "U" input corrupted by multi-color interference with 256 pulses having pulse width 5 ms (effective illumination time = 1.28 s), (e-g) only the pattern is corrupted by single-color interference, (h) the whole pattern is corrupted by random coloured pixels with equal optical intensity (light intensity = 400 μWcm^{-2}). The conductance states of the array are shown immediately (column 2), at 10 s (column 3), 30 s (column 4), and 60 s (column 5) after the scanning pulse removal. For all cases, the array was trained with a "U" pattern at 450 nm wavelength light, allowing the conductance levels of the pixel devices to reach high enough to be capable of "self-denoising". For (e-g), the multicolour interference is removed immediately after scanning, while for (h), the array denoises

itself completely in ~10 s. Reprinted with permission under a Creative Commons CC-BY license from Ref. [53] Copyright [2021] [Springer Nature].

The contour plot illustrates that the noisy input was successfully detected and suppressed after scanning (t ~ 0 s) for the wavelengths of 300 nm, 450 nm, and 1.0 µm, and noise pixels were processed and eliminated within 10 s for a 2 µm wavelength. The same experiment was performed with a higher Gaussian noise level of σ = 0.3. The entire noise pixels are intimidated within the 10s for the wavelengths 300 nm, 450 nm, and 1.0 µm, whereas the 2.0 µm wavelength required 30 s to completely remove the noise pixel. The outcomes revealed that the denoising process takes a longer time even if the LTP conductance state is low. Next, the multi-color noise pixel of 100 % intensity was exposed to the target pattern (see **Fig. 26(e-h)**). The proposed array successfully differentiated between the target and noise pixel, and the noise pixel was completely suppressed within 10 s of scanning. These findings are vital to achieve the human visual system, which has the capability of sensing and processing optical information without any external aid. However, a self-denoising mechanism is applicable for supervised learning, and further algorithms are required to develop noise robustness for unsupervised learning. In addition, further growth kinetics of MoS_2 and the interface between MoS_2 and the gate dielectric oxide need to be optimized to enhance the operational speed of the device. However, both strategies might impede the data retention of optoelectronic synapse devices. Hence, a novel device design can be an effective approach to memory retention. The report shows excellent memory performance, such as long LTP, retention ≥ 1200 s. However, the pulse width of 5 ms and scanning time of 1.28 s describe the tradeoff between speed and retention. This required more extensive exploration of the device performance for real-time imaging and video rating. The energy per spike, DC endurance of potentiation and depression cycles, and retention with cycle number are also crucial for exploration. A larger number of offline training pulses (1024 pulses) limits the fast and dynamic updating scenarios.

Inspired by this, Wang *et al*. [57] proposed a MoS_2/WSe_2-based p-n van der Waals heterostructure memtransistor to emulate optoelectronic synaptic function (see **Fig. 27(a)**). The output transfer characteristics confirmed the bipolar resistive switching with a switching ratio of 10^3 under 30 cycles, along with minimum variation in V_{SET} and V_{RESET} voltages throughout the scan loop, signifying high stability (see **Fig. 27(b)**). The positive and negative gate voltage of different amplitudes (V_G = 1, 3, 5, 7 V) having a pulse width of 500 ms at a constant V_{ds} of 1 V is used to simulate EPSC and IPSC, respectively (see **Fig. 27(c)**. The EPSC and the decay time gradually increased with the amplitude, indicating the STM to LTM transition. In contrast, the IPSC decreased with the negative gate voltage amplitude, and the relaxation time increased. The LTP and LTD were successfully demonstrated with 20 positive and negative gate voltage pulses of amplitude 3 V with a pulse width of 500 ms. The results showed excellent reproducibility with 10 consecutive LTP/LTD measurements, unveiling stable conductance modulation and consistent synaptic weight changes up to 400 pulses (see **Fig. 27 (d-e)**). The photoresponse of the device was demonstrated with different wavelengths (600, 500, 400 nm) at a constant power density of 0.55 mW cm^{-2}. The high PSC was perceived for a shorter wavelength, and the device current did not decay to its initial value, dictating non-volatile memory behaviour. The STM

to LTM transition was observed for a high-power-density optical pulse, which is explained by the presence of defects within the channel, resulting in an extended relaxation time. The learning, forgetting, and re-learning process is simulated by applying 30 consecutive pulses, which symbolize the initial learning process in which EPSC increases. Following this, the forgetting process is achieved by allowing the device to rest for 40 s, and EPSC declines. In the re-learning phase, 17 pulses were enough to achieve the previous current level, which indicates the device exhibits memory functionality similar to the human brain (see **Fig. 27(f)**). The PPF calculation of the device is shown in **Fig. 27 (g)**. The light adaptation behavior of human vision was realized under mild and strong illumination (see **Fig. 27(h)**). In particular, the human eyes adapt to strong illumination by adjusting the pupil size and modulating the light sensitivity of the retina. This particular function was realized by applying the negative gate voltage, which modulates the current by impeding the flow of the charge carrier in the channel. Hence, this strategy offers great potential for p-n heterojunction memtransistor for visual neuromorphic applications. This work reported the limited resistive switching (RS) cycles of 30 SET/RESET 10 repeated LTP/LTD cycles need further performance enhancement for synaptic application. The D2D variation, including the ON/OFF ratio and elevated temperature retention, is needed to explore more for device performance. The high operation voltage ±5 V and the optical pulse width 100-500 ms lead to high energy consumption and slow synaptic update.

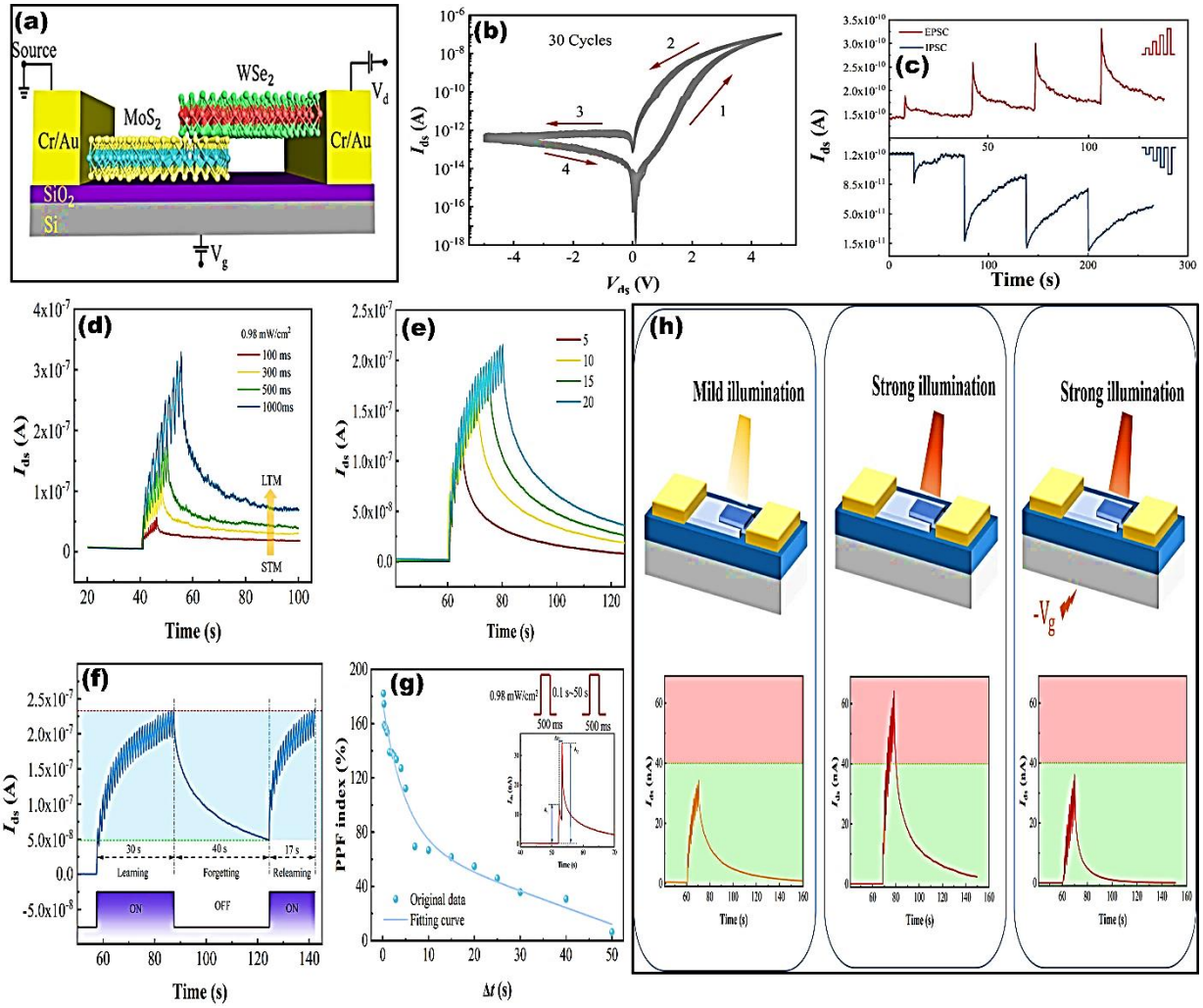

Fig. 27. (a) Schematic diagram of the MoS_2/WSe_2 heterojunction memtransistor, (b) Resistive switching in I_{ds}-V_{ds} curves for 30 cycles, (c) EPSC/IPSC curve of the device. Optical synaptic simulations in the MoS_2/WSe_2 memtransistor, (d) Under different pulse widths, (e) EPSC results under different light pulse numbers, (f) Learning, forgetting, and relearning training of optical synapses, and (g) PPF index versus pulse interval (Δt). The inset shows the PSC triggered by a pair of light pulses. Simulation of light adaption behavior, (h) Primarily, the current of the device is below the threshold (< 40 nA) under mild illumination while in the second case, the current of the device is above the threshold (> 40 nA) under strong illumination and lastly, when a negative gate voltage is applied, the current in the device under strong illumination falls below the threshold (< 40 nA), which corresponds to the light adaption behavior of the visual system. Reproduced or adapted with permission from Ref. [57] Copyright [2024] [American Chemical Society].

Furthermore, An *et al*. [55] demonstrated tantalum nickel sulfide (Ta_2NiS_5)/MoS_2 heterojunction to emulate energy-efficient optoelectronic synapses, which can be stimulated by gate voltage, bias voltage, and light pulses (see **Fig. 28 (a)**). **Fig. 28. (b)** depicts the optical microscope image of the heterojunction on the Si/SiO_2 substrate, where the orange outline represents the MoS_2 region, and the green one represents the Ta_2NiS_5 region. The optoelectronic synaptic functionality was explored by modulating the synaptic weight through optical pulse intensity, duration, width, frequency, and gate voltage. The EPSC was rapidly increased to 117.47 nA upon applying the optical pulse with a wavelength of 532 nm for 200 ms, and the current persisted at the same value for a longer time, indicating non-volatile behavior (see **Fig. 28(c)**). The EPSC was observed to increase with time

duration, which is attributed to the trap state present in the materials and the potential barrier at the interface. The PPF was observed to reach its maximum value of 135 % when the time interval was 100 ms and exponentially decayed with the increasing time interval (see **Fig. 28(d)**). The device showed STM to LTM transformation with an increasing number of pulses (see **Fig. 28(e)**). In addition, frequency-dependent retention was also explored. The EPSC was found to be increased from 140.3 to 253.2 nA as the frequency increased from 0.1 to 2.5 Hz, signifying better learning and retention (see **Fig. 28(f)**). Lastly, the device showed excellent pattern accuracy of 91.52% after 1,000 training sessions (see **Fig. 28(g-h)**). The performance across multiple devices is limited, making it difficult to statistically assess energy efficiency and multilevel stability. The long-term DC cycling, read/write endurance, and retention over thermal stress are also needed to explore the device's performance. The large pulse width of 200-300 ms and the non-linearity over optical intensity hinder the fast update of the devices to be implemented in the neuromorphic application.

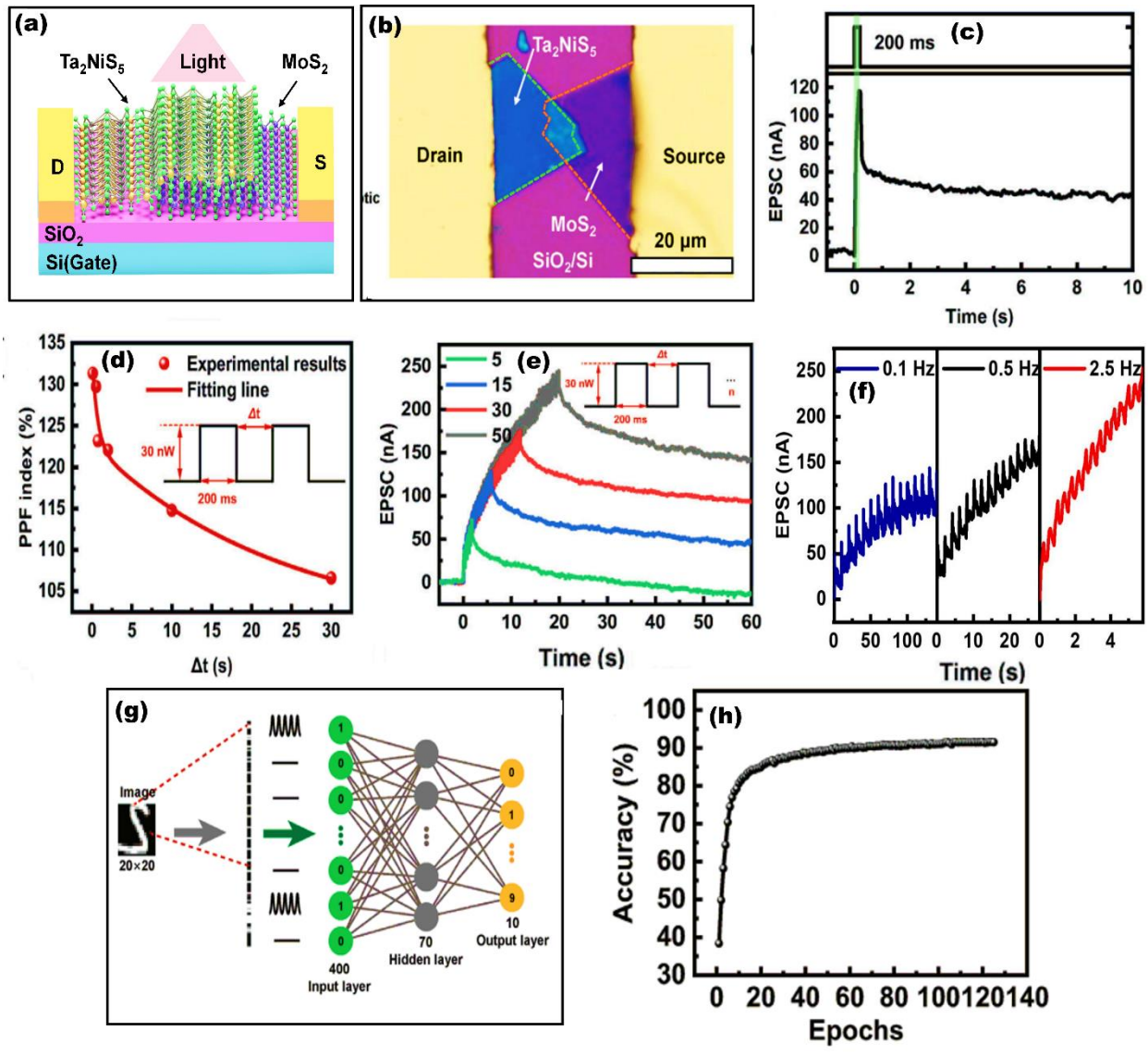

Fig. 28 (a) Schematic diagram of the MoS_2/WSe_2 heterojunction memtransistor, (b) Optical microscope image of the heterojunction on Si/SiO_2 substrate, where the orange outline represented the MoS_2 region, and the green one represented the Ta_2NiS_5 region. Optoelectronic hetero-synaptic measurements of MoS_2/Ta_2NiS_5 heterojunction, (c) EPSC triggered by an optical pulse (532 nm), (d) PPF index measured at different time intervals while inset shows pulsing scheme, (e) EPSC of the device in response to multiple optical pulses while inset shows pulsing scheme for each cycle, (f) The EPSC of the device stimulated by fifteen optical spikes of 200 ms with different frequencies, (g) Schematic diagram of a three-layer neural network and (h) Simulation result of the pattern recognition accuracy. Reproduced or adapted with permission from Ref. [55] Copyright [2024] [Wiley].

Recently, an ion-modulated 2D-WS_2 heterosynaptic memtransistor (Na^+@WSHMT) was proposed by Liu *et al*. [172] by incorporating Na^+ ions to achieve synaptic modulation and energy-efficient neuromorphic computing. The resistive switching is initiated by the interaction of S vacancies and Na^+ ions. Under the electric field (V_{sd}) stimulation, Na^+ ion adsorbs S vacancies and then migrate on its surface, and finally bind with the vacancies, resulting in a resistive switching mechanism (see **Fig. 29(a)**. **Fig. 29(b)** shows a typical peak of E^1_{2g} (in-plane) and A_{1g} (out-of-plane) vibration mode of WS_2 in the Raman spectra under 0 to 3V. The gate voltage-driven tunability in heterosynaptic plasticity was examined. Primarily, the Na^+ ion within the lattice plays a crucial role in modulating the conductivity. When the V_G increases significantly, the Na^+ ion relocates toward the WS_2 lattice, resulting in the augmentation of Na^+ ions within the lattice, which consequently enhances the device conductance (see **Fig. 29(c-d)**). Furthermore, Na^+ ions introduce a defect in the WS_2 lattice, resulting in an additional impurity energy level (E_i).

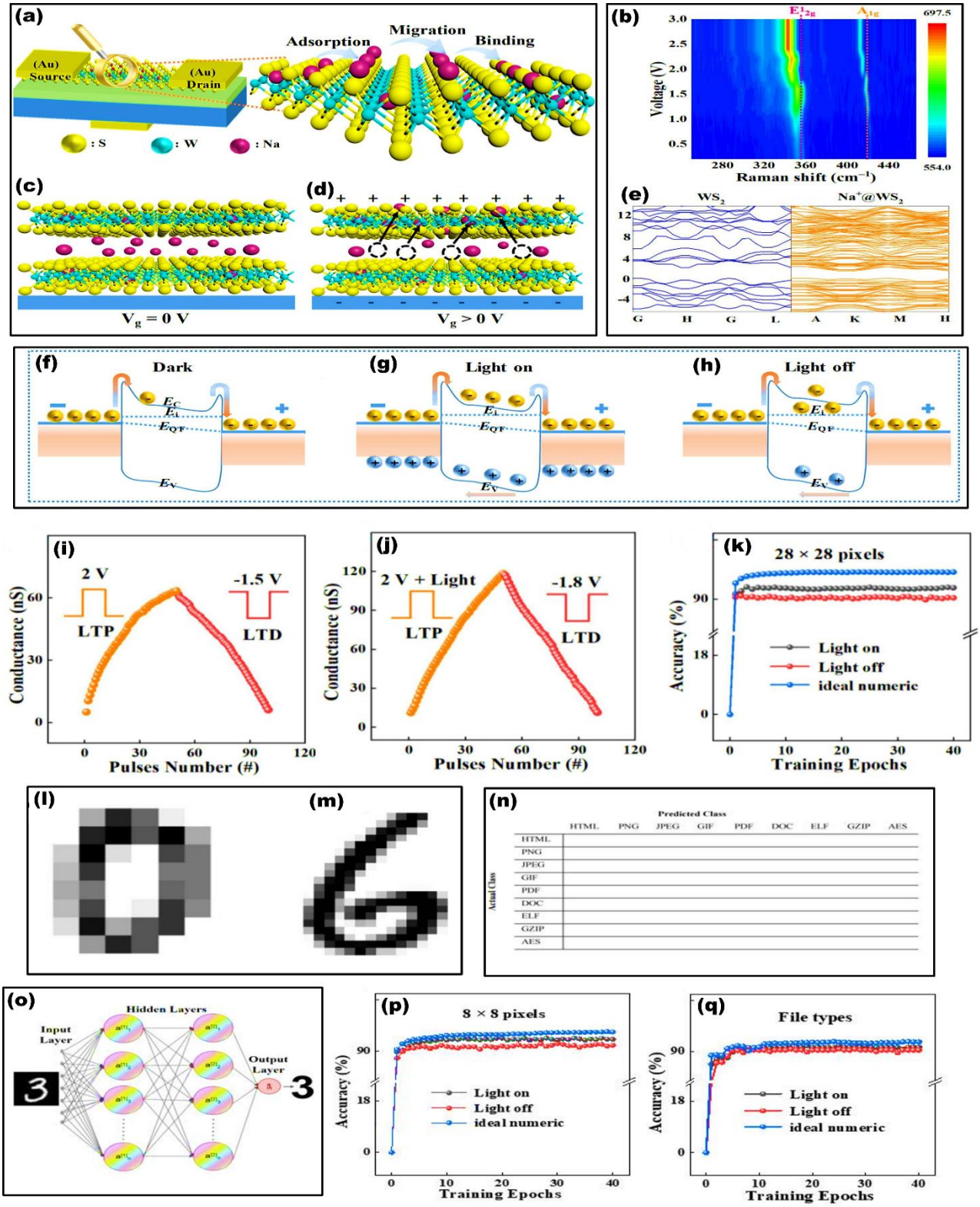

Fig. 29. Mechanistic study of the Na^+@WSHMT, (a) Adsorption-migration-binding mechanism dominated by Na^+ ions and S vacancies under source and drain voltage stimulation, (b) Pseudo-color plot of the V_{sd}-dependent Raman spectra measured on Na^+@WSHMT for 0 to 3 V voltage sweep, (c-d) Mechanism of V_g-induced heterosynaptic plasticity, (e) Band structure of WS_2 and Na^+@WS_2, (f-h) Mechanism of light-induced heterosynaptic plasticity. Application of Na^+@WSHMT for pattern recognition and feature extraction, (i-j) LTP and LTD profiles of Na^+@WSHMT without light (i) and under light (j), (k) The recognition results of Na^+@WSHMT-based ANN for (28×28) pixel digit, (l-n). Examples of the different datasets. 8×8 image is from the Optical Recognition of Handwritten Digits dataset. (o) An ANN consisting

of an input layer, hidden layer, and output layer. (p-q) The recognition results of Na^+@WSHMT-based ANN for 8×8-pixel digits (p) and file type datasets (q). Reproduced or adapted with permission from Ref. [172] Copyright [2024] [Elsevier].

Under optical stimulation, this E_i acts as the trapping center for photogenerated charge carriers and increases the carrier lifetime, unlocking the potential of optical modulation. These results are confirmed with the DFT simulation (see **Fig. 29(e)**). Furthermore, the energy band diagram of Au/WS_2/Au formed a Schottky barrier due to the difference between the high work function of Au (5.1 V) and the WS_2 electron affinity (4.0-1.5 eV). Under dark conditions, the voltage stimulation (V_{sd}) promotes the electron injection from the source to the drain by crossing the Schottky barrier and forming a current. Under the optical stimulation, the photogenerated charge carrier led to the enhancement of current. These charge carriers are trapped by E_i when the optical stimuli are withdrawn, which extends the lifetime, resulting in the light-induced PSC response of the device (see **Fig. 29(f-h)**). Hence, either gate voltage or light pulses can be used to achieve homosynaptic plasticity. Furthermore, the heterosynaptic plasticity was also studied by applying both V_{sd} and V_G/optical stimulation. The conductance of the device was more linear and symmetric under light, suggesting it is controlled by both electrical and optical signals (see **Fig. 29(i-j)**). The ANN was designed for the recognition of Handwritten digit datasets, including handwritten digital images of 28 × 28 (MNIST) and 8×8-pixel images. The **Fig. 29(k)** depicts the recognition results for a (28×28) pixel digit. The examples of the different datasets of 8×8 images are from the Optical Recognition of Handwritten Digits dataset, and a three-layer network based on the Cross-Sim crossbar simulator is shown in **Fig. 29(l-o**). The recognition accuracy under the light of 93.3 % and 94.5 % was achieved for large and small pixel digits, respectively. The recognition accuracies enhance under the light stimulation, which demonstrates a great potential to design the basic artificial neural network. The result demonstrated that the larger pulse width in milliseconds to seconds is not mapped to high throughput for ANN hardware requirements. The ANN simulations needed to explore the array level non-idealities such as D2D variation, parasitic overlap, and sneak path issues. The device also needs further quantification on the long-time endurance cycles, retention for elevated device performance. The hetero synaptic modulation is utilized by the top electrical terminal. The energy overhead of the integrated light source of the optical simulation still needs to be addressed.

Deng *et al.* [173] developed a mild oxygen-doped MoS_2-based memtransistor for neuromorphic computing. The mechanically exfoliated MoS_2 was exposed to rapid thermal annealing in an Ar environment, along with low-temperature ultraviolet ozone (UVO) for surface modification. The schematic representation of biological neurons and a 4-terminal artificial hetero-synaptic device is shown in **Fig. 30(a)**. Herein, the source terminal acts as postsynaptic neurons, the top photogate and bottom electric gate act as presynaptic neurons, and channel conductance represents the synaptic

weight. The EPSC response of the fabricated device under optical stimuli (wavelength = 400 nm, V_{ds} = 1 V) with varying durations (50 to 2000 ms) is shown in **Fig. 30(b)**. A rapid increment in the EPSC is observed, followed by a slow relaxation time by applying the different presynaptic spikes. In addition, the EPSC response was enhanced by increasing the pulse width from 50 ms to 2000 ms. Furthermore, the PPF index is gradually decreased from 1.33 to 1.02 as the time interval varies from 50 ms to 20 s. The PPF index is fitted with an exponential decay function, which reveals very low fluctuation within a 95% confidence interval. Next, the denoising and image recognition capabilities of the device are realized. For this, a (28×28) grayscale image with a denoised pixel is used as an input for the ANN for image recognition, as depicted in **Fig. 30(d)**. The ANN network comprises 784 input neurons linked to 32 hidden neurons and 10 output neurons. The enhancement in the image recognition accuracy with the training time after 50 epochs is observed at different denoising preprocessing stages, as shown in **Fig. 30(e-g)**. The image recognition accuracy was enhanced from 89.7 to 95.7% after denoising for the photo-heterosynaptic device. The outstanding performance of photo-heterosynaptic devices establishes a promising paradigm for the development of complex neuromorphic electronic systems.

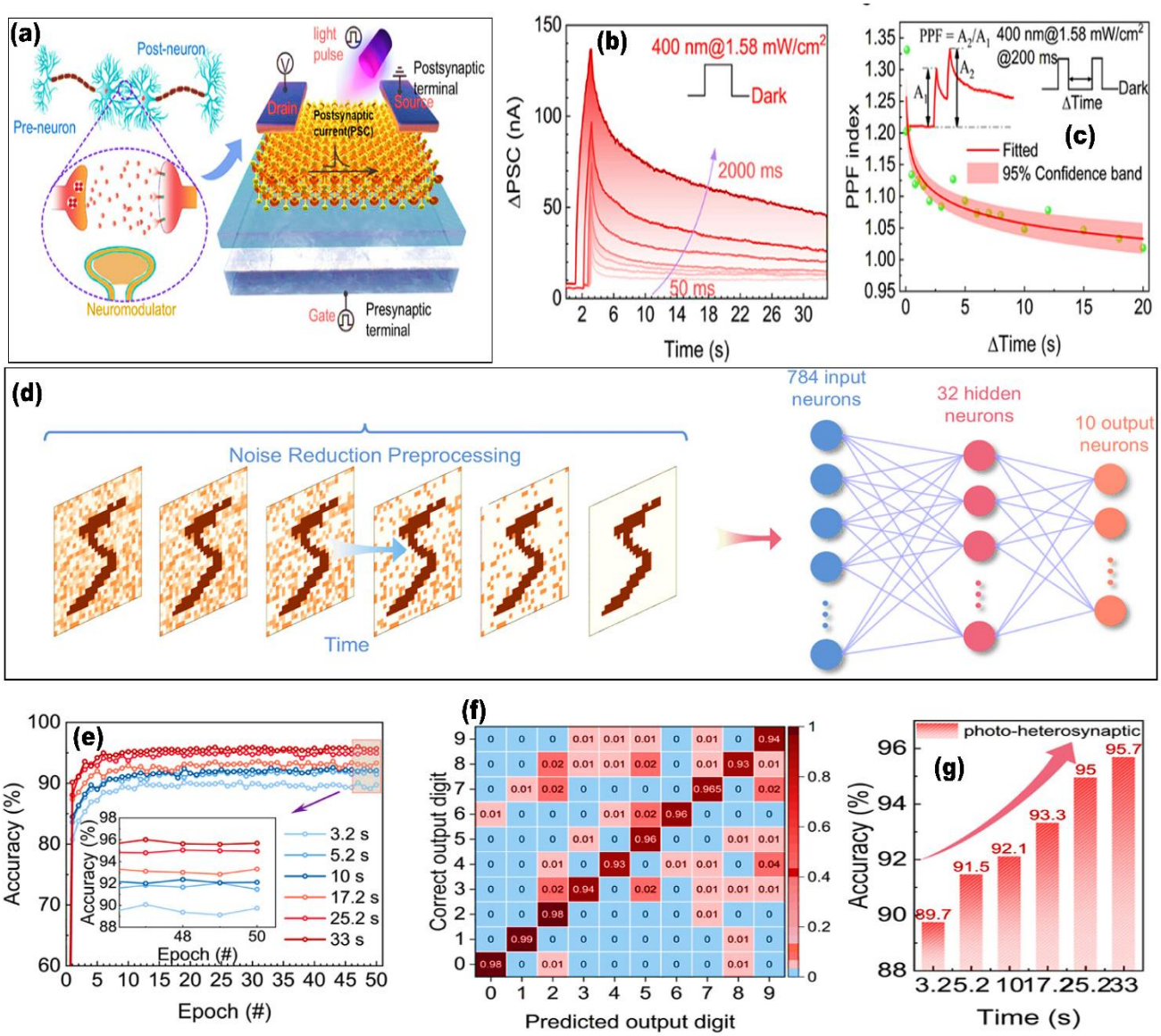

Fig. 30 (a) Schematic illustration of biological neurons (left) and artificial synapse memtransistor (right), (b) current response under the optical stimuli (400 nm, 1.58 mW/cm^2) as a function of light pulse duration time, (c) PPF index as a function of time interval between two sequential optical pulses (400 nm, 1.58 mW/cm^2), (d) Schematic diagram of the effect of denoising preprocessing over time, and the input of the denoising preprocessed image into an artificial neural network (ANN) for image recognition, (e) image recognition accuracy with training times at different denoising preprocessing stages (Inset: the accuracy at the last 4 iterations), (f) confusion matrix after 33 s denoising preprocessing. (g) Comparison of accuracy between different denoising preprocessing stages after 50 training cycles. Reproduced or adapted with permission from Ref. [173], Copyright [2025] [American Chemical Society].

Critical Challenges and Future Outlook

Advancements in materials science and device engineering have driven the development of optoelectronic synaptic devices, which integrate sensing, storage, and computing functions to meet the demands of applications like robotics, autonomous vehicles, and smart cities. These devices enable synaptic weight adjustment across a wide optical spectrum (UV to near-infrared) and offer capabilities, such as colour discrimination, selective non-volatile photodetection, and bidirectional photo-responsiveness, making them vital for artificial visual intelligence. Additionally, their high bandwidth,

low power consumption, and minimal crosstalk enhance response speed, enabling efficient visual information processing and supporting hardware-level artificial visual perception systems. Despite these advancements, developing optoelectronic memristive and memtransistors with enhanced opto-synaptic performance, cost-effective fabrication processes, low power consumption, and environmental sustainability remains a significant challenge. Materials such as 2D layered materials, perovskites, and ferroelectric materials hold great promise for optoelectronic synaptic devices due to their exceptional optical and electrical properties. However, to fully harness their potential for photodetection and synaptic functionality, the synergistic integration of hybrid materials from the macroscopic to nanoscale levels is essential. For heterojunction-based optoelectronic synaptic transistors, a critical challenge lies in achieving long-term synaptic plasticity. This issue arises from the rapid de-trapping of photocarriers at the interface, which often leads to volatile retention behavior. Photonic neuromorphic computing inherently demands both positive (e.g., EPSC) and negative (e.g., IPSC) synaptic plasticity. However, most optoelectronic synapses struggle to generate negative light responses, relying instead on electrical stimulation to implement IPSCs for bidirectional weight updates. This dependency significantly limits the processing speed, bandwidth, and integration density of these devices. Polychromatic identification systems have been demonstrated in other studies, but they often produce relatively narrow output differences for varying input lengths, leading to potential ambiguities under optically complex conditions. Modulating synaptic plasticity through multispectral selectivity has been proposed as a solution for achieving more effective colour perception. However, realising selectivity for three or more colours typically requires multi-channel logic operations and intricate circuit architectures, which involve complex manufacturing processes. This complexity increases production costs, extends manufacturing cycles, and results in higher power consumption and lower system integration. Consequently, these factors reduce pixel density and resolution in vision perception systems. Beyond these challenges, optoelectronic synaptic devices for artificial visual perception systems generally operate within static light intensity ranges, leading to fixed thresholds. This limitation hinders the development of adaptive artificial visual systems capable of self-regulation in response to environmental changes, such as biological light adaptation or dark adaptation. Such systems are essential for distinguishing bright light in well-lit conditions or recognising weak light in low-light environments. To address this, the visual system's triggering threshold must be dynamically adjusted based on synaptic weights corresponding to ambient light conditions. Despite these requirements, the absence of ideal hardware for adaptive visual perception that combines low complexity, feasible power consumption, and practical implementation remains a significant barrier to the realisation of bionic visual neuromorphic systems.

Significant progress has been made in optoelectronic synapses as a promising candidate for visual signal processing. However, practical application in neuromorphic visual perception and memory faces challenges such as miniaturisation, high power consumption, low CMOS compatibility, and complex architectures. Current research largely focuses on single devices mimicking basic synaptic functions and is far from large-scale integration. For miniaturised, high-resolution artificial vision systems, optoelectronic synapses must scale to the nanoscale, requiring advanced nanofabrication techniques. Although new photosensitive materials improve photo-responsivity and spectral range, immature fabrication processes limit device stability and reproducibility. Wafer-scale production of 2D materials via methods like CVD is still rare, with most relying on mechanical exfoliation, leading to inconsistent device performance. These issues hinder the development of large-scale device arrays for hardware artificial neural networks. Developing high-performance optoelectronic synaptic transistors for mimicking the human eye in artificial intelligence faces significant challenges. A flexible, highly sensitive neuromorphic imaging system capable of image perception and data preprocessing is essential but difficult to achieve due to material, device, and imaging module limitations. While some photo-synaptic transistors exhibit high sensitivity, most rely on rigid inorganic materials unsuitable for flexible applications. Organic materials allow large-area, ultra-flexible devices that conform to 3D surfaces like the human retina, but they suffer from low photosensitivity under dim light due to high exciton binding energy. Consequently, photodetection accuracy, noise immunity, and image recognition are poor, limiting the advancement of neuromorphic imaging systems for AI applications.

Optoelectronic synaptic devices that combine sensing, storage, and computing are crucial for advancing artificial intelligence and the Internet of Things. These devices enable breakthroughs in synaptic plasticity, image enhancement/erasure, and 3D image perception and preprocessing. With appropriate material choices and device designs, their potential can be further unlocked, accelerating the development of hardware-based neural networks and neuromorphic computing systems. This progress could overcome the limitations of the von Neumann architecture by integrating vision sensors and information processing units. However, challenges remain in addressing complex processing, uniformity, and reliability for widespread application.

Conclusion

In summary, we have discussed the potential of 2D materials for bionic vision, highlighting their properties and the challenges limiting memristive and memtransistor device technologies. Benefitting from atomic-scale thickness, high surface area, strong light-matter interaction, and attractive electronic properties, 2D materials stand out as a prominent candidate for making advancements in neuromorphic

computing. These materials facilitate the development of novel device architectures with operational mechanisms involving ion/vacancy migration, charge trapping, and de-trapping under the influence of both electric and optical stimuli, which are vital for designing a bionic vision system. Furthermore, 2D-based memristive and memtransistors devices offer great advantages, such as high sensitivity, low power consumption, and fast response, which are crucial for artificial vision applications. Regardless of their potential, some technological challenges warrant attention related to optimising the growth mechanism of 2D materials to achieve high-quality thin film, clean large-area transfer of thin film, uniform deposition, industry-compatible fabrication, enhancing the device endurance, and improving operational stability. Moreover, along with existing challenges, future research must emphasise achieving realistic biological vision functionality, such as high colour resolution, the process of encoding and processing image data in the vision system, and extending the light response range. Moving forward, the biocompatibility and safety of 2D materials-based hardware devices still require more clinical and biological trials. Therefore, the multidisciplinary approach, poised with academia and industry, needs joint effort and cooperation of materials scientists, electronic engineering, computational modeling, and biomedicine to unlock the potential of 2D-based hardware devices for bionic vision applications.

CRediT authorship contribution statement

Aarti Dahiya: Writing-review & editing, Writing-original draft, Methodology, Investigation, Formal Analysis, and Conceptualization. **Parthasarathi Pal**: Writing-review & editing, Investigation, and Formal analysis. **Shalu Rani**: Writing-review & editing, Formal analysis, Methodology, Resources, and Supervision. **Mohit K. Gautam**: Writing-review & editing, and Formal Analysis. **Roshni Shateesh Babu**: Writing-review & editing and Formal Analysis. **Ioannis Zeimpekis**: Writing-review & editing, and Formal Analysis. **Dimitra D. Georgiadou**: Writing-review & editing, Formal Analysis, Methodology, Resources, and Supervision. **Sanjay Kumar**: Writing-review & editing, Conceptualization, Methodology, Investigation, Formal Analysis, Resources, and Supervision.

Declaration of Competing Interest

The authors declare that they have no known competing financial interests or personal relationships that could have appeared to influence the work reported in this paper.

Acknowledgements

A. Dahiya would like to thank the IIT(ISM) Dhanbad for providing an institute teaching assistant fellowship for a PhD. P. Pal would like to thank the Department of Science & Technology (DST), New

Delhi, for the DST-NPDF fellowship award letter no. JNC/AO/A.1707/(29)/25-OW-183. S. Kumar would like to thank the Department of Science & Technology (DST), New Delhi, for the research grant via IFA23-ENG-375. S. Rani would like to thank the Faculty Research Scheme (FRS) project no. MISC0085. M. K. Gautam would like to thank National Overseas Scholarship (File No.: K-11015/100/2023-SCD-V-(NOS)). D. G. Georgiadou and R. S. Babu acknowledge support from the UK Multidisciplinary Centre for Neuromorphic Computing (UKRI982) and the UKRI Future Leaders Fellowship Grant (MR/V024442/1).

Data availability

No data was used for the research described in the article.

References

1. I. Arikpo, F. U. Ogban, and I. E. Eteng, Von Neumann Architecture, and Modern Computers, Global Journal of Mathematical Sciences. 6 (2007) 97-103. https://doi.org/10.4314/gjmas.v6i2.21415.
2. W. Wulf and S.A. McKee, Hitting the memory wall: implications of the obvious, Computer Architecture News. 23 (1995) 20-24. https://doi.org/10.1145/216585.216588.
3. W. Ou, S. Xiao, C. Zhu, W. Han, and Q. Zhang, An overview of brain-like computing: Architecture, applications, and future trends, Frontier in Nanorobotics. 24 (2022) 1041108.10.3389/fnbot.2022.1041108
4. H. Seok, D. Lee, S. Son, H. Choi, G. Kim, and T. Kim, Beyond von Neumann Architecture: Brain-Inspired Artificial Neuromorphic Devices and Integrated Computing, Advanced Electronics Materials. 10 (2024) 2300839. https://doi.org/10.1002/aelm.202300839.
5. D. Ielmini, Z. Wang, and Y. Liu, Brain-inspired computing via memory device physics, APL Materials. 9 (2021) 050702. https://doi.org/10.1063/5.0047641.
6. S. J. Kim, S. Kim, and H. W. Jang, Competing memristors for brain-inspired computing, iSCIENCE. 24 (2021) 101889. https://doi.org/10.1016/j.isci.2020.101889.
7. F. Rosenblatt, The Perceptron: A Perceiving and Recognizing Automaton, Report No. 85-460-1, Cornell Aeronautical Laboratory, Buffalo, New York, 1957.
8. M. Minsky and S.A. Papert, Perceptrons: An Introduction to Computational Geometry. MIT Press (1969), Cambridge. https://core.ac.uk/download/pdf/82206249.pdf
9. P. Gao and M. Adnan, Overview of emerging electronics technologies for artificial intelligence: A review, Materials Today Electronics. 11 (2025) 100136. https://doi.org/10.1016/j.mtelec.2025.100136.
10. S. Jiang, S. Nie, Y. He, R. Liu, C. Chen, Q. Wan, Emerging synaptic devices: from two-terminal memristors to multiterminal neuromorphic transistors, Materials Today Nano. 8 (2019) 100059. https://doi.org/10.1016/j.mtnano.2019.100059.
11. H. Bian, Y.Y. Goh, Y. Liu, H. Ling, L. Xie, and X. Liu, Stimuli-responsive memristive materials for artificial synapses and neuromorphic computing, Advanced Materials. 33 (2021) 2006469. https://doi.org/10.1002/adma.202006469.
12. Z. R. Wang, S. Joshi, S. E. Savel'ev, H. Jiang, R. Midya, P. Lin, M. Hu, N. Ge, J. P. Strachan, Z. Li, Q. Wu, M. Barnell, G. L. Li, H. L. Xin, R. S. Williams, Q. Xia, and J. J. Yang, Memristors with diffusive dynamics as synaptic emulators for neuromorphic computing, Nature Materials. 16 (2017) 101–108. https://doi.org/10.1038/nmat4756.
13. L. Chua, Memristor-the missing circuit element, IEEE Transactions on Circuit Theory. 18 (1971) 507–519. https://doi.org/10.1109/TCT.1971.1083337.
14. D. B. Strukov, G.S. Snider, D.R. Stewart, and R. S. Williams, The missing memristor found, Nature. 453 (2008) 80–83. https://doi.org/10.1038/nature06932.
15. K. Gou, Y. Li, H. Song, R. Lu, and J. Jiang, Optimization strategy of the emerging memristors: From material preparation to device applications, iSCIENCE. 27 (2024) 111327. https://doi.org/10.1016/j.isci.2024.111327.
16. J. B. Roldán, E. Miranda, D. Maldonado, A. N. Mikhaylov, N. V. Agudov, A. A. Dubkov, M. N. Koryazhkina, M. B. González, M. A. Villena, S. Poblador, M. S. Tapia, R. Picos, F. J. Molinos, S. G. Stavrinides, E. Salvador, F. J. Alonso, F. Campabadal, B. Spagnolo, M. Lanza, and L. O. Chua, Variability in Resistive Memories, Advanced Intelligent System. 5 (2023) 2200338. https://doi.org/10.1002/aisy.202200338.

17. G. C. Adam, A. Khiat, and T. Prodromakis, Challenges hindering memristive neuromorphic hardware from going mainstream, Nature Communications. 9 (2018) 5267. https://doi.org/10.1038/s41467-018-07565-4.
18. J. Bae, J. Won, and W. Shim, The rise of memtransistors for neuromorphic hardware and In-memory computing, Nano Energy. 126 (2024) 109646. https://doi.org/10.1016/j.nanoen.2024.109646.
19. F. Yang, Z. Liu, X. Ding, Y. Li, C. Wang, and G. Shen, Carbon-based memristors for resistive random-access memory and neuromorphic applications, Chip. 3 (2024) 100086. https://doi.org/10.1016/j.chip.2024.100086.
20. E. Shi, Y. Gao, B. P. Finkenauer, Akriti, A. H. Coffeya, and L. Dou, Two-dimensional halide perovskite nanomaterials and heterostructures, Chemical Society Reviews. 47 (2018) 6046-6072. https://doi.org/10.1039/C7CS00886D.
21. K. T. Chen and J. S. Chen, Perspective on oxide-based three-terminal artificial synapses in physical neural networks, Applied Physics Letters. 121 (2022) 190501. https://doi.org/10.1063/5.0115449.
22. J. Panisilvam, H. Y. Lee, S. Byun, D. Fan, and S. Kim, Two-dimensional material-based memristive devices for alternative computing, Nano Convergence. 11 (2024). https://doi.org/10.1186/s40580-024-00432-7.
23. S. Oh, H. Hwang, and I. K. Yoo, Ferroelectric materials for neuromorphic computing, APL Materials. 7 (2019) 091109. https://doi.org/10.1063/1.5108562.
24. S. H. Choi, S. J. Yun, Y. S. Won, C. S. Oh, S. M. Kim, K. K. Kim, and Y. H. Lee, Large-scale synthesis of graphene and other 2D materials towards industrialization, Nature Communications. 13 (2022) 1484. https://doi.org/10.1038/s41467-022-29182-y.
25. K. S. Novoselov, A. Mishchenko, A. Carvalho, and A. H. C. Neto, 2D materials and van der Waals heterostructures, Science. 353 (2016) aac9439. https://doi.org/10.1126/science.aac9439.
26. L. Yin, R. Cheng, Y. Wen, C. Liu, and J. He, Emerging 2D Memory Devices for In-Memory Computing, Advanced Materials 33 (2021) 2007081. http://dx.doi.org/10.1002/adma.202007081.
27. Z. Peng, L. Tong, W. Shi, L. Xu, X. Huang, Z. Li, X. Yu, X. Meng, X. He, S. Lv, G. Yang, H. Hao, T. Jiang, X. Miao, and L. Ye, Multifunctional human visual pathway-replicated hardware based on 2D materials, Nature Communications. 15 (2024) 8650. DOI: https://doi.org/10.1038/s41467-024-52982-3.
28. Y. Wang, L. Yin, W. Huang, Y. Li, S. Huang, Y. Zhu, D. Yang, and X. Pi, Optoelectronic synaptic devices for neuromorphic computing, Advanced Intelligent Systems. 3 (2021) 2000099. https://doi.org/10.1002/aisy.202000099.
29. W. Huang, H. Zhang, J. Tang, Z. Lin, T. Guo, Y. Zhou, S. Jiang, P. Hang, M. Jiao. C. Zhu, L. Wang, D. Yang, X. Yu, and X. Li, Self-Powered Optoelectronic Synaptic Devices for Neuromorphic Computing with the Lowest Energy Consumption Density, ACS Photonics. 11 (2024) 3095–3104. https://doi.org/10.1021/acsphotonics.4c00379.
30. S. M. Kwon, S. W. Cho, M. Kim, J. S. Heo, Y. H. Kim, and S. K. Park, Environment-adaptable artificial visual perception behaviors using a light-adjustable optoelectronic neuromorphic device array, Advanced Materials. 31 (2019) 1906433. https://doi.org/10.1002/adma.201906433.
31. S. Hong, S. H. Choi, J. Park, H. Yoo, J. Y. Oh, E. Hwang, D. H. Yoon, and S. Kim, Sensory adaptation and neuromorphic phototransistors based on $CsPb(Br_{1-x}I_x)_3$ perovskite and MoS_2 hybrid structure, ACS Nano. 14 (2020) 9796–9806. https://doi.org/10.1021/acsnano.0c01689.
32. J. K. Han, D. M. Geum, M. W. Lee, J. M. Yu, S. K. Kim, S. Kim, and Y. K. Choi, Bioinspired photoresponsive single transistor neuron for a neuromorphic visual system, Nano Letters. 20 (2020) 8781–8788. https://doi.org/10.1021/acs.nanolett.0c03652.
33. N. Li, S. Zhang, Y. Peng, X. Li, Y. Zhang, C. He, and G. Zhang, 2D Semiconductor-Based Optoelectronics for Artificial Vision, Advanced Functional Materials. 33 (2023) 2305589. https://doi.org/10.1002/adfm.202305589.
34. Q. B. Zhu, B. Li, D. D. Yang, C. Liu, S. Feng, M. L. Chen, Y. Sun, Y. N. Tian, X. Su, X. M. Wang, S. Qiu, Q. W. Li, X. M. Li, H. B. Zeng, H. M Cheng, and D. M. Sun, A flexible ultrasensitive optoelectronic sensor array for neuromorphic vision systems, Nature Communications. 12 (2021) 1798. https://doi.org/10.1038/s41467-021-22047-w.
35. R. K. Shepherd, M. N. Shivdasani, D. A. X. Nayagam, C. E. Williams, and P. J. Blamey, Visual prostheses for the blind, Trends Biotechnology. 31 (2013) 562–571. https://doi.org/10.1016/j.tibtech.2013.07.001.
36. H. Wang, Q. Zhao, Z. Ni, Q. Li, H. Liu, Y. Yang, L. Wang, Y. Ran, Y. Guo, W. Hu, and Y. Liu, A ferroelectric/electrochemical modulated organic synapse for ultraflexible. Artificial Visual-Perception System, Advanced Materials. 30 (2018) 1803961. https://doi.org/10.1002/adma.201803961.
37. Y. Lee and T. W. Lee, Organic synapses for neuromorphic electronics: from brain-inspired computing to sensorimotor nervetronics, Account of Chemical Research. 52 (2019) 964–974. https://doi.org/10.1021/acs.accounts.8b00553.
38. L. Huilin, J. Xiantao, Y. Wenbin, H. Zhang, L. Zhou, F. Zhang, D. She, Y. Zhou, and S. T. Han, Fully photon modulated heterostructure for neuromorphic computing, Nano Energy. 65 (2019) 104000. https://doi.org/10.1016/j.nanoen.2019.104000.
39. J. Sun, S. Oh, Y. Choi, S. Seo, M. J. Oh, M. Lee, W. B. Lee, P. J. Yoo, J. H. Cho, J. H. Park, Optoelectronic Synapse Based on IGZO-Alkylated Graphene Oxide Hybrid Structure, Advanced Functional Materials. 28 (2018) 1804397. https://doi.org/10.1002/adfm.201804397.

40. F. Zhou, Z. Zhou, J. Chen, H. Choy, N. Zhang, Z. Lin, S. Yu, J. Kang, H. S. P. Wong, and Y. Chai, Optoelectronic resistive random-access memory for neuromorphic vision sensors, Nature Nanotechnology. 14 (2019) 776-782. https://doi.org/10.1038/s41565-019-0501-3.
41. S. Seo, S. H. Jo, S. Kim, J. Shim, S. Oh, J. H. Kim, K. Heo, J. W. Choi, C. Choi, S. Oh, D. Kuzum, H. S. P. Wong, and J. H. Park, Artificial optic-neural synapse for colored and color-mixed Pattern recognition, Nature Communications. 9 (2018) 5106. https://doi.org/10.1038/s41467-018-07572-5.
42. L. Liu, Z. Cheng, B. Jiang, Y. Liu, Y. Zhang, F. Yang, J. Wang, X. F. Yu, P. K. Chu, and C. Ye, Optoelectronic Artificial Synapses Based on Two-Dimensional Transitional-Metal Trichalcogenide, ACS Applied Materials & Interfaces. 13 (2021) 30797−30805. https://doi.org/10.1021/acsami.1c03202
43. S. G. Kim, S. H. Kim, J. Park, G. S. Kim, J. H. Park, K. C. Saraswat, J. Kim, and H. Y. Yu, Infrared Detectable MoS_2 Phototransistor and its Application to Artificial Multilevel Optic-Neural Synapse, ACS Nano. 13 (2019) 10294–10300. https://doi.org/10.1021/acsnano.9b03683.
44. P. Lei, H. Duan, L. Qin, X. Wei, R. Tao, Z. Wang, F. Guo, M. Song, W. Jie, and J. Hao, High-Performance Memristor Based on 2D Layered BiOI Nanosheet for Low-Power Artificial Optoelectronic Synapses, Advanced Functional Materials. 32 (2022) 220127. https://doi.org/10.1002/adfm.202201276.
45. S. Oh, J. J. Lee, S. Seo, G. Yoo, and J. H. Park, Photoelectroactive artificial synapse and its application to biosignal pattern recognition, npj 2D Materials and Applications. 5 (2021) 95. https://doi.org/10.1038/s41699-021-00274-5.
46. D. Kumar, H. Li, U. K. Das, A. M. Syed, and N. E. Atab, Flexible Solution-Processable Black-Phosphorus-Based Optoelectronic Memristive Synapses for Neuromorphic Computing and Artificial Visual Perception Applications, Advanced Materials. 35 (2023) 2300446. https://doi.org/10.1002/adma.202300446.
47. J. Du, D. Xie, Q. Zhang, H. Zhong, F. Meng, X. Fu, Q. Sun, H. Ni, T. Li, E. Guo, H. Guo, M. He, C. Wang, L. Gu, X. Xu, G. Zhang, G. Yang, K. Jin, and C. Ge, A robust neuromorphic vision sensor with optical control of ferroelectric switching, Nano Energy. 89 (2021) 106439. https://doi.org/10.1016/j.nanoen.2021.106439.
48. D. Kumar, L. Joharji, H. Li, A. Rezk, A. Nayfeh, and N. E. Atab, Artificial visual perception neural system using a solution-processable MoS_2-based in-memory light sensor, Light: Science & Applications. 12 (2023) 109. https://doi.org/10.1038/s41377-023-01166-7.
49. J. Meng, T. Wang, H. Zhu, L. Ji, W. Bao, P. Zhou, L. Chen, Q. Q. Sun, D. W. Zhang, Integrated In-Sensor Computing Optoelectronic Device for Environment-Adaptable Artificial Retina Perception Application, Nano Letters. 22 (2022) 81-89. https://doi.org/10.1021/acs.nanolett.1c03240.
50. W. Li, W. Li, T. Cheng, L. Wang, L. Yao, H. Yang, X. Zhang, W. Zheng, Y. Wang, J. Zhang, Visible-light irradiation improved resistive switching characteristics of a 2D $Cs_2Pb(SCN)_2I_2$-Based memristor device, Ceramics International. 49 (2023) 4909-4918. https://doi.org/10.1016/j.ceramint.2022.10.005.
51. M. C. Sahu, S. Sahoo, S. K. Mallik, A. K. Jena, and S. Sahoo, Multifunctional 2D MoS_2 Optoelectronic Artificial Synapse with Integrated Arithmetic and Reconfigurable Logic Operations for In-Memory Neuromorphic Computing Applications, Advanced Materials Technologies. 8 (2023) 2201125. https://doi.org/10.1002/admt.202201125.
52. Y. Wang, Y. Zha, C. Bao, Y. Di, C. Liu, F. Xing, X. Xu, X. Wen, Z. Gan, and B. Jia, Monolithic 2D Perovskites Enabled Artificial Photonic Synapses for Neuromorphic Vision Sensors, Advanced Materials. 36 (2024) 2311524. https://doi.org/10.1002/adma.202311524.
53. M. M. Islam, M. S. Rahman, H. Heldmyer, S. S. Han, Y. Jung, and T. Roy, Bio-inspired "Self-denoising" capability of 2D materials incorporated optoelectronic synaptic array, npj 2D Materials and Applications. 8 (2024) 21. https://doi.org/10.1038/s41699-024-00458-9.
54. D. Kumar, R. Bharti, H. Li, D. D. Kumbhar, and N. E. Atab, Optoelectronic wide-band-gap oxide-based memristor for mimicking human eye sensory perception and object tracking, Cell Reports Physical Science. 5 (2024) 102144. https://doi.org/10.1016/j.xcrp.2024.102144.
55. J. An, N. Zhang, F. Tan, X. Zhao, C. Chang, M. Lanza, and S. Li, Programmable Optoelectronic Synaptic Transistors Based on MoS_2/Ta_2NiS_5 Heterojunction for Energy-Efficient Neuromorphic Optical Operation, Small. 20 (2024) 2403103. https://doi.org/10.1002/smll.202403103.
56. Y. Lin, W. Wang, R. Li, J. Kim, C. Zhang, H. Kan, and Y. Li. Multifunctional optoelectronic memristor based on CeO_2/MoS_2 heterojunction for advanced artificial synapses and bionic visual system with nociceptive sensing, Nano Energy. 121 (2024) 109267. https://doi.org/10.1016/j.nanoen.2024.109267.
57. X. Wang, F. Chen, X. Li, T. Xiang, and L. Wang, Emulation of Optoelectronic Synaptic Behavior in a MoS_2/WSe_2-Based p−n van der Waals Heterostructure Memtransistor, ACS Applied Electronic Materials. 6 (2024) 4311−4320. https://doi.org/10.1021/acsaelm.4c00397.
58. M. T. H. Do, S. H. Kang, T. Xue, H. Zhong, H.W. Liao, D. E Bergles, and K. W. Yau, Photon capture and signaling by melanopsin retinal ganglion cell, Nature. 457 (2008) 281–287. 10.1038/nature07682
59. R. S. Molday and O. L. Moritz, Photoreceptors at a glance, Journal of Cell Science. 128 (2015) 4039–4045. https://doi.org/10.1242/jcs.175687.
60. M. H. Pirenne. Rods and Cones, The Visual Process. (1962) 13-29. https://doi.org/10.1016/B978-1-4832-3089-4.50011-X.

61. F. Zhou, Z. Zhou, J. Chen, T. H. Choy, J. Wang, N. Zhang, Z. Lin, S. Yu, J. Kang, H. S. P. Wong, and Y. Chai, Optoelectronic resistive random access memory for neuromorphic vision sensors, Nature Nanotechnology. 14 (2019). 776-782. https://doi.org/10.1038/s41565-019-0501-3.
62. C. Choi, J. Leem, M.S. Kim, A. Taqieddin, C. Cho, K. W. Cho, G. J. Lee, H. Seung, H. J. Bae, Y. M. Song, T. Hyeon, N. R. Aluru, S. W. Nam, and D. H. Kim, Curved neuromorphic image sensor array using a MoS_2-organic heterostructure inspired by the human visual recognition system, Nature Communications. 11 (2020) 5934. https://doi.org/10.1038/s41467-020-19806-6.
63. M. Prezioso, F. M. Bayat, B. D. Hoskins, G. C. Adam, K. K. Likharev, and D. B. Strukov, Training and operation of an integrated neuromorphic network based on metal-oxide memristors, Nature. 521 (2015) 61-64. https://doi.org/10.1038/nature14441.
64. T. Leydecker, M. Herder, E. Pavlica, G. Bratina, S. Hecht, E. Orgiu, and P. Samorì, Flexible non-volatile optical memory thin-film transistor device with over 256 distinct levels based on an organic bicomponent blend, Nature Nanotechnology. 11 (2016) 769–775. https://doi.org/10.1038/nnano.2016.87.
65. M. Kuno, T. Yasunami, and S. Matsuura, Excitatory postsynaptic currents in response to different synaptic inputs of frog spinal motoneurons, Neuroscience Research. 5 (1988) 240-252. https://doi.org/10.1016/0168-0102(88)90052-1.
66. T. Zhao, S. Zhang, Y. Guo, and Q. Wang, TiC_2: a new two-dimensional sheet beyond MXenes, Nanoscale. 8 (2016) 233–242. https://doi.org/10.1039/C5NR04472C.
67. H. Wang, H. Liu, Q. Zhao, Z. Ni, Y. Zou, J. Yang, L. Wang, Y. Sun, Y. Guo, W. Hu, and Y. Liu, A retina-like dual band organic photosensor array for filter-free near-infrared-to-memory operations, Advanced Materials. 29 (2017) 1701772. https://doi.org/10.1002/adma.201770234.
68. Y. Wang, Z. Lv, J. Chen, Y. Zhou, L. Zhou, X. Chen, and S. T. Han, Photonic synapses based on inorganic perovskite quantum dots for neuromorphic computing, Advanced Materials. 30 (2018) 1802883. https://doi.org/10.1002/adma.201802883.
69. D. C. Hu, R. Yang, L. Jiang, and X. Guo, Memristive synapses with photoelectric plasticity realized in ZnO_{1-x}/AlO_y heterojunction, ACS Applied Materials Interfaces. 10 (2018) 6463–6470. https://doi.org/10.1021/acsami.8b01036.
70. T. Tsuchiya, T. Nakayama, and K. Ariga, Nanoarchitectonics Intelligence with atomic switch and neuromorphic network system, Applied Physics Express. 15 (2022) 100101. https://doi.org/10.35848/1882-0786/ac926b.
71. W. S. Wang and L. Q. Zhu, Recent advances in neuromorphic transistors for artificial perception applications, Science and Technology of Advanced Materials. 24 (2023) 2152290. https://doi.org/10.1080/14686996.2022.2152290.
72. K. Pilarczyk, A. Podborska, M. Lis, M. Kawa, D. Migdal, and K. Szaciłowski, Synaptic behavior in an optoelectronic device based on semiconductor-nanotube hybrid, Advanced Electronics Materials. 2 (2016) 1500471. https://doi.org/10.1002/aelm.201500471.
73. D. Kuzum, S. Yu, and H. S. W Philip, Synaptic electronics: materials, devices and applications, Nanotechnology. 24 (2013) 382001. http://doi.org/10.1088/0957-4484/24/38/38200.
74. P. Maier, F. Hartmann, M. Emmerling, C. Schneider, M. Kamp, S. Höfling, and L. Worschech, Electrophoto-sensitive memristor for neuromorphic and arithmetic computing, Physics Review Applied. 5 (2016) 054011. https://doi.org/10.1103/PhysRevApplied.5.054011.
75. R. A. John, F. Liu, N. A. Chien, M. R. Kulkarni, C. Zhu, Q. Fu, A. Basu, Z. Liu, and N. Mathews, Synergistic gating of electro-iono-photoactive 2D chalcogenide neuristors: coexistence of Hebbian and homeostatic synaptic metaplasticity, Advanced Materials. 30 (2018) 1800220. https://doi.org/10.1002/adma.201800220.
76. D. Ielmini, and H. S. P. Wong, In-memory computing with resistive switching devices, Nature Electronics. 1 (2018) 333–343. https://doi.org/10.1038/s41928-018-0092-2.
77. Y. Zhai, Z. Feng, Y. Zhou, and S. T. Han, Energy-efficient transistors: suppressing the subthreshold swing below the physical limit, Materials Horizons. 8 (2021) 1601–1617. https://doi.org/10.1039/D0MH02029J.
78. H. Li, R. Wang, S.T. Han, Y. Zhou, Ferroelectric polymers for non-volatile memory devices: a review, Polymer International. 69 (2020) 533–544. https://doi.org/10.1002/pi.5980.
79. Q. Zhang, T. Jin, X. Ye, D. Geng, W. Chen, and W. Hu, Organic field effect transistor-based photonic synapses: materials, devices, and applications, Advanced Functional Materials. 31 (2021) 2106151. http://dx.doi.org/10.1002/adfm.202106151.
80. C. Chang, W. Chen, Y. Chen, Y. Chen, Y. Chen, F. Ding, C. Fan, H. J. Fan, Z. Fan, C. Gong, Y. Gong, Q. He, X. Hong, S. Hu, W. Hu, W. Huang, Y. Huang, W. Ji, D. Li, L. J. Li, Q. Li, Li Lin, C. Ling, M. Liu, N. Liu, Z. Liu, K. P. Loh, J. Ma, F. Miao, H. Peng, M. Shao, L. Song, S. Su, S. Sun, C. Tan, Z. Tang, D. Wang, H. Wang, J. Wang, X. Wang, X. Wang, A. T. S. Wee, Z. Wei, Y. Wu, Z. S. Wu, J. Xiong, Q. Xiong, W. Xu, P. Yin, H. Zeng, Z. Zeng, T. Zhai, H. Zhang, H. Zhang, Q. Zhang, T. Zhang, X. Zhang, L. D. Zhao, M. Zhao, W. Zhao, Y. Zhao, K. G. Zhou, X. Zhou, Y. Zhou, H. Zhu, H. Zhang, and Z. Liu, Recent progress on two-dimensional materials, Acta Physico-Chimica Sinica. 37 (2021) 2108017. https://doi.org/10.3866/PKU.WHXB2021080173.

81. C. Du, Y. Ren, Z. Qu, L. Gao, Y. Zhai, S. T. Han, and Y. Zhou, Synaptic transistors and neuromorphic systems based on carbon nano-materials, Nanoscale. 13 (2021) 7498–7522. https://doi.org/10.1039/D1NR00148E.
82. T. Hasegawa, K. Terabe, T. Nakayama, and M. Aono, Quantum point contact switch realized by solid electrochemical reaction, International Conference on Solid State Devices and Materials, Tokyo, (2001) 564-565. https://doi.org/10.7567/SSDM.2001.D-8-3.
83. K. Terabe, T. Hasegawa, T. Nakayama, and M. Aono, Quantized conductance atomic switch. Nature. 433 (2005) 47–50. https://doi.org/10.1038/nature03190.
84. T. Sakamoto, H. Sunamura, H. Kawaura, T. Hasegawa, T. Nakayama, and M. Aono, Nanometer-scale switches using copper sulfide, Applied Physics Letters. 82 (2003) 3032-3034. https://doi.org/10.1063/1.1572964.
85. S. Sucharitakul, G. Ye, W.R.L. Lambrecht, C. Bhandari, A. Gross, R. He, H. Poelman, and X.P.A. Gao, V_2O_5: A 2D van der Waals oxide with strong in-plane electrical and optical anisotropy, ACS Applied Materials Interfaces. 9 (2017) 23949-23956 https://doi.org/10.1021/acsami.7b05377.
86. S. M. Hus, R. Ge, P.A. Chen, L. Liang, G. E. Donnelly, W. Ko, F. Huang, M. H. Chiang, A. P. Li, and D. Akinwande, Observation of single-defect memristor in an MoS_2 atomic sheet, Nature Nanotechnology. 16 (2021) 58-62. https://doi.org/10.1038/s41565-020-00789-w.
87. V. K. Sangwan, D. Jariwala, I. S. Kim, K. S. Chen, T. J. Marks, L. J. Lauhon, and M. C. Hersam, Gate-tunable memristive phenomena mediated by grain boundaries in single-layer MoS_2, Nature Nanotechnology. 10 (2015) 403-406. https://doi.org/10.1038/nnano.2015.56.
88. M. Belete, S. Kataria, A. Turfanda, S. Vaziri, T. Wahlbrink, O. Engström, and M. C. Lemme, Nonvolatile Resistive Switching in Nanocrystalline Molybdenum Disulfide with Ion-Based Plasticity, Advanced Electronics Materials. 6 (2020) 1900892. https://doi.org/10.1002/aelm.201900892.
89. S. Wang, C. Y. Wang, P. Wang, C. Wang, Z. A. Li, C. Pan, Y. Dai, A. Gao, C. Liu, J. Liu, H. Yang, X. Liu, B. Cheng, K. Chen, Z. Wang, K. Watanabe, T. Taniguchi, S. J. Liang, and F. Miao. Networking retinomorphic sensor with memristive crossbar for brain-inspired visual perception. National Science Review. 8 (2021) nwaa172. https://doi.org/10.1093/nsr/nwaa172.
90. K. A. Nirmal, D. D. Kumbhar, A. V. Kesavan, T. D. Dongale, and T. G. Kim, "Advancements in 2D layered material memristors: unleashing their potential beyond memory," npj 2D Mater Applied. 8 (2024) 83. https://doi.org/10.1038/s41699-024-00522-4.
91. V. K. Sangwan, H. S. Lee, H. Bergeron, I. Balla, M. E. Beck, K. S. Chen, and M. C. Hersam, Multi-terminal memtransistors from polycrystalline monolayer molybdenum disulfide, Nature. 554 (2018) 500-504. https://doi.org/10.1038/nature25747.
92. J. Bae, J. Won, and W. Shim, The rise of memtransistors for neuromorphic hardware and In-memory computing, Nano Energy. 126 (2024) 109646. https://doi.org/10.1016/j.nanoen.2024.109646
93. X. Yan, J. H. Qian, V. K. Sangwan, and M. C. Hersam, Progress and challenges for memtransistors in neuromorphic circuits and systems. Advanced Materials. 34 (2022) 2108025. https://doi.org/10.1002/adma.202108025.
94. L. Sun, L. Y. Zhang, G. Han, G. Hwang, J. Jiang, B. Joo, K. Watanabe, T. Taniguchi, Y. M. Kim, W. J. Yu, B. S. Kong, R. Zhao, and H. Yang, Self-selective van der Waals heterostructures for large-scale memory array. Nature Communications. 10 (2019) 3161. https://doi.org/10.1038/s41467-019-11187-9.
95. C. Y. Wang, S. J. Liang, S. Wang, P. Wang, Z. Li, Z. Wang, A. Gao, C. Pan, C. Liu, J. Liu, H. Yang, X. Liu, W. Song, C. Wang, B. Cheng, X. Wang, K. Chen, Z. Wang, K. Watanabe, T. Taniguchi, J. J. Yang, and F. Miao, Gate-tunable van der Waals heterostructure for reconfigurable neural network vision sensor, Science Advances. 6 (2020) eaba6173. https://doi.org/10.1126/sciadv.aba6173.
96. G. R. Bhimanapati, Z. Lin, V. Meunier, Y. Jung, J. Cha, S. Das, D. Xiao, Y. Son, M. S. Strano, V. R. Cooper, L. Liang, S. G. Louie, E. Ringe, W. Zhou, S. S. Kim, R. R. Naik, B. G. Sumpter, H. Terrones, F. Xia, Y. Wang, J. Zhu, D. Akinwande, N. Alem, J. A. Schuller, R. E. Schaak, M. Terrones, and J. A. Robinson, Recent Advances in Two-Dimensional Materials beyond Graphene. ACS Nano. 9 (2015) 11509. https://doi.org/10.1021/acsnano.5b05556.
97. M. Chhowalla, H. S. Shin, G. Eda, L. J. Li, K. P. Loh, and H. Zhang, The chemistry of two-dimensional layered transition metal dichalcogenide nanosheets. Nature Chemistry. 5 (2013) 263. https://doi.org/10.1038/nchem.1589.
98. M. Wang, H. Li, T. J. Ko, M. S. Shawkat, E. Okogbue, C. Yoo, S. S. Han, M. A. Islam, K. H. Oh, and Y. Jung, Manufacturing strategies for wafer-scale two-dimensional transition metal dichalcogenide heterolayers. Journal of Materials Research. 35 (2020) 1350. https://doi.org/10.1557/jmr.2020.27.
99. F. Xia, H. Wang, and Y. Jia, Rediscovering black phosphorus as an anisotropic layered material for optoelectronics and electronics. Nature Communications. 5 (2014) 4458. https://doi.org/10.1038/ncomms5458.
100. S. Bertolazzi, P. Bondavalli, S. Roche, T. San, S.Y. Choi, L. Colombo, F. Bonaccorso, and P. Samori, Nonvolatile memories based on graphene and related 2D materials. Advanced Materials. 31 (2019) 1806663. https://doi.org/10.1002/adma.201806663.

101. F. Hui, E. G. Gutierrez, S. Long, Q. Liu, A.K. Ott, A.C. Ferrari, and M. Lanza, Graphene and related materials for resistive random-access memories, Advanced Electronics Materials. 3 (2017) 1600195. https://doi.org/10.1002/aelm.201600195.
102. D.P. Sahu, P. Jetty, and S.N. Jammalamadaka, Graphene oxide-based synaptic memristor device for neuromorphic computing. Nanotechnology. 32 (2021) 155701. https://doi.org/10.1088/1361-6528/abd978.
103. X. Meng, G. Qin, and Y. Sun, Graphene oxide-based bioinspired neuromorphic transistors with artificial synaptic plasticity. Materials Science in Semiconductor Processing. 186 (2025) 109053. https://doi.org/10.1016/j.mssp.2024.109053.
104. Q. Tian, X. Sui, X. Zhao, Y. Lin, Z. Wang, Y. Tao, H. Xu, Y. Liu. An Optoelectronic Memristor Based on Proton-Involved Photoreduction for Bimodal Sensing, Memory, and Processing. Advanced intelligent system. 7 (2025) 2400968. https://doi.org/10.1002/aisy.202400968.
105. J. Wu, H. Lin, D.J. Moss, K.P. Loh, and B. Jia, Graphene oxide for photonics, electronics, and optoelectronics. Nature Reviews Chemistry. 7 (2023) 162–183. https://doi.org/10.1038/s41570-022-00458-7.
106. Yi Zhou, D. Liu, J. Wang, Z. Cheng, L. Liu, N. Yang, Y. Liu, T. Xia, X. Liu, X. Zhang, C. Ye, Z. Xu, W. Xiong, P.K. Chu, and X. F. Yu, Black Phosphorus-Based Multicolor Light-Modulated Transparent Memristor with Enhanced Resistive Switching Performance. ACS Applied Materials Interfaces. 12 (2020) 25108–25114. https://doi.org/10.1021/acsami.0c04493
107. Q.H. Wang, K.K. Zadeh, A. Kis, J.N. Coleman, and M.S. Strano, Electronics and optoelectronics of two-dimensional transition metal dichalcogenides. Nature Nanotechnology. **7** (2012) 699-712. https://doi.org/10.1038/nnano.2012.193
108. J.A. Wilson, F.J.D. Salvo, and S. Mahajan, Charge-density waves and superlattices in the metallic layered transition metal dichalcogenides. Advances in Physics. 24 (1975) 117-201. https://doi.org/10.1080/00018737500101391.
109. S. Joseph, J. Mohan, S. Lakshmy, S. Thomas, B. Chakraborty, S. Thomas, and N. Kalarikkal, A review of the synthesis, properties, and applications of 2D transition metal dichalcogenides and their heterostructures, Materials Chemistry and Physics. 297 (2023) 127332. https://doi.org/10.1016/j.matchemphys.2023.127332.
110. R.S. Babu and D.G. Georgiadou, 2D transition metal dichalcogenides for energy-efficient two-terminal optoelectronic synaptic devices. Devices. 3 (2025) 100805. https://doi.org/10.1016/j.device.2025.100805.
111. Q. Ma, G. Ren, A. Mitchell, and J.Z. Ou, Recent advances on hybrid integration of 2D materials on integrated optics platforms. Nanophotonics. 9 (2020) 2191-2214. 10.1515/nanoph-2019-0565.
112. A. Chaves, J.G. Azadani, H. Alsalman, D.R.D. Costa, R. Frisenda, A.J. Chaves, S.H. Song, Y.D. Kim, D. He, J. Zhou, A.C. Gomez, F.M. Peeters, Z. Liu, C.L. Hinkle, S. Oh, P.D. Ye, S.J. Koester, Y.H. Lee, P. Avouris, X. Wang, and T. Low, Bandgap engineering of two-dimensional semiconductor materials. Npj 2D Materials and Applications 4 (2020) 1-21. https://doi.org/10.1038/s41699-020-00162-4S.
113. M. Long, A. Gao, P. Wang, H. Xia, C. Ott, C. Pan, Y. Fu, E. Liu, X. Chen, W. Lu, T. Nilges, J. Xu, X. Wang, W. Hu, and F. Miao, Room temperature high-detectivity mid-infrared photodetectors based on black arsenic phosphorus, Science Advances. 3 (2017) 1700589. https://doi.org/10.1126/sciadv.1700589.
114. J. Jiang, J. Guo, X. Wan, Y. Yang, H. Xie, D. Niu, J. Yang, J. He, Y. Gao, and Q. Wa, 2D MoS_2 neuromorphic devices for brain-like computational systems, Small 13 (2017) 1700933. https://doi.org/10.1002/smll.201700933.
115. D. Xie, J. Jiang, and L. Ding, Anisotropic 2D materials for post-Moore photoelectric devices, Journal of Semiconductors. 43 (2022) 010201. http://doi.org/10.1088/1674-4926/43/1/010201.
116. L. Wei, Y. Li, C. Tian, and J. Jiang, Recent progress in anisotropic 2D semiconductors: from material properties to photoelectric detection, Physica Status Solidi (a). 218 (2021) 2100204. https://doi.org/10.1002/pssa.202100204.
117. N. Li, S. Zhang, Y. Peng, X. Li, Y. Zhang, C. He, and G. Zhang, 2D Semiconductor-Based Optoelectronics for Artificial Vision, Advanced Functional Materials. 33 (2023) 2305589. https://doi.org/10.1002/adfm.202305589.
118. J. Bullock, A. Cuevas, T. Allen, and C. Battaglia, Molybdenum oxide MoOx: A versatile hole contact for silicon solar cells, Applied Physics Letters. 105 (2014) 232109. https://doi.org/10.1063/1.4903467.
119. S. Kumar, D.D. Kumbhar, J.H. Park, R. K. Kamat, T. D. Dongale, and S. Mukherjee, Y_2O_3-Based Crossbar Array for Analog and Neuromorphic Computation, IEEE Transactions on Electron Devices 70 (2022) 473-477. https://doi.org/10.1109/TED.2022.3227890.
120. X. Zhou, W. Wu, J. Chen, S. Fan, and Y. Zhang, Self-adaptive negative photoelectric memristor for an autobrake system with sensing-memory-computing-control function, Chemical Engineering Journal 519 (2025) 164912. https://doi.org/10.1016/j.cej.2025.164912.
121. X. Dong, Q. Liu, S. Liu, R. Wu, and L. Ma, Silk fibroin-based conductive film for multifunctional sensing and energy harvesting, Advanced Fiber Materials. 4 (2022) 885–893, https://doi.org/10.1007/s42765-022-00152-9.
122. A. Eftekhari, Tungsten dichalcogenides (WS_2, WSe_2, and WTe_2): materials chemistry and applications, Journal of Materials Chemistry A. 5 (2017) 18299–18325, https://doi.org/10.1039/C7TA04268J.

123. N. Lu, L. Li, P. Sun, M. Wang, Q. Liu, H. Lv, S. Long, and M. Liu, A novel method of identifying the carrier transport path in metal oxide resistive random-access memory, Journal of Physics D: Applied Physics. 48 (2015) 065101. https://doi.org/10.1088/0022-3727/48/6/065101.
124. H. Wang, J. Peca, M. Matsuzaki, K. Matsuzaki, J. Noguchi, L. Qiu, D. Wang, F. Zhang, E. Boyden, K. Deisseroth, H. Kasai, W. C. Hall, G. Feng, and G. J. Augustine, High-speed mapping of synaptic connectivity using photostimulation in Channelrhodopsin-2 transgenic mice, Proceedings of the National Academy of Sciences. 104 (2007) 8143-8148. https://doi.org/10.1073/pnas.0700384104
125. X. Liu, S. Ramirez, P.T. Pang, C. B. Puryear, A. Govindarajan, K. Deisseroth, and S. Tonegawa, Optogenetic stimulation of a hippocampal engram activates fear memory recall, Nature. 484 (2012) 381. https://doi.org/10.1038/nature11028.
126. S. Nabavi, R. Fox, C.D. Proulx, J. Y. Lin, R. Y. Tsien, and R. Malinow, Engineering a memory with LTD and LTP, Nature 511 (2014) 348. https://doi.org/10.1038/nature13294.
127. S. Seo, J. J. Lee, R. G. Lee, T. H. Kim, S. Park, S. Jung, H. K. Lee, M. Andreev, K. B. Lee, K. S. Jung, S. Oh, H. J. Lee, K. S. Kim, G. Y. Yeom, Y. H. Kim, and J. H. Park, An Optogenetics-Inspired Flexible van der Waals Optoelectronic Synapse and its Application to a Convolutional Neural Network, Advanced Materials. 33 (2021) 2102980. https://doi.org/10.1002/adma.202102980.
128. S. Tongay, H. Sahin, C. Ko, A. Luce, W. Fan, K. Liu, J. Zhou, Y. S. Huang, C. H. Ho, J. Yan, D. F. Ogletree, S. Aloni, J. Ji, S. Li, J. Li, F. M. Peeters, and J. Wu, Monolayer behaviour in bulk ReS_2 due to electronic and vibrational decoupling, Nature Communions. 5 (2014) 3252. https://doi.org/10.1038/ncomms4252.
129. S. Hadke, M. Huang, C. Chen, Y. F. Tay, S. Chen, J. Tang, and L. Wong, Emerging Chalcogenide Thin Films for Solar Energy Harvesting Devices, Chemical Review. 122 (2022) 10170-10265. https://doi.org/10.1021/acs.chemrev.1c00301.
130. H. J. Kim, K. J. Yoon, T. H. Park, H. J. Kim, Y. J. Kwon, X. L. Shao, D. E. Kwon, Y. M. Kim, and C. S. Hwang, Filament Shape Dependent Reset Behavior Governed by the Interplay between the Electric Field and Thermal Effects in the Pt/TiO2/Cu Electrochemical Metallization Device, Advanced Electronics Materials. 3 (2017) 1600404. https://doi.org/10.1002/aelm.201600404
131. Y. Yang, P. Gao, L. Li, X. Pan, S. Tappertzhofen, S. H. Choi, R. Waser, I. Valov, and W. D. Lu, Electrochemical dynamics of nanoscale metallic inclusions in dielectrics, Nature Communications. 5 (2014) 4232. https://doi.org/10.1038/ncomms5232.
132. D. Kumar, R. Aluguri, U. Chand, T. Y. Tseng, Enhancement of resistive switching properties in nitride-based CBRAM device by inserting an Al_2O_3 thin layer, Applied Physics Letters. 110 (2017) 203102. https://doi.org/10.1063/1.4983465.
133. S. Lee, F. Yang, J. Suh, S. Yang, Y. Lee, G. Li, H. S. Choe, A. Suslu, Y. Chen, C. Ko, J. Park, K. Liu, J. Li, K. Hippalgaonkar, J. J. Urban, S. Tongay, and J. Wu, Anisotropic in-plane thermal conductivity of black phosphorus nanoribbons at temperatures higher than 100 K, Nature Communications. 6 (2015) 8573. https://doi.org/10.1038/ncomms9573.
134. K. He, Y. Liu, J. Yu, X. Guo, M. Wang, L. Zhang, C. Wan, T. Wang, C. Zhou, and X. Chen, Artificial Neural Pathway Based on a Memristor Synapse for Optically Mediated Motion Learning, ACS Nano. 16 (2022) 9691. https://doi.org/10.1021/acsnano.2c03100.
135. K. Wang, S. Dai, Y. Zhao, Y. Wang, C. Liu, J. Huang, Light-Stimulated Synaptic Transistors Fabricated by a Facile Solution Process Based on Inorganic Perovskite Quantum Dots and Organic Semiconductors, Small. 15 (2019) 1900010. https://doi.org/10.1002/smll.201900010.
136. L. N. Quan, M. Yuan, R. Comin, O. Voznyy, E. M. Beauregard, S. Hoogland, A. Buin, A. R. Kirmani, K. Zhao, A. Amassian, D. H. Kim, and E. H. Sargent, Ligand-Stabilized Reduced-Dimensionality Perovskites, Journal of the American Chemical Society.138 (2016) 2649. https://doi.org/10.1021/jacs.5b11740.
137. S. Bertolazzi, D. Krasnozhon, and A. Kis, Nonvolatile memory cells based on MoS_2/graphene heterostructures, ACS Nano. 7 (2013) 3246–3252. https://doi.org/10.1021/nn3059136.
138. E. Zhang, W. Wang, C. Zhang, Y. Jin, G. Zhu, Q. Sun, D. W. Zhang, P. Zhou, and F. Xiu, Tunable charge-trap memory based on few-layer MoS_2, ACS Nano. 9 (2015) 612–619. https://doi.org/10.1021/nn5059419.
139. Z. Yin, Z. Zeng, J. Liu, Q. He, P. Chen, and H. Zhang, Memory devices using a mixture of MoS_2 and graphene oxide as the active layer, Small. 9 (2013) 727–731. https://doi.org/10.1002/smll.201201940.
140. J. Liu, Z. Zeng, X. Cao, G. Lu, L. H. Wang, Q. L. Fan, W. Huang, and H. Zhang, Preparation of MoS_2-Polyvinylpyrrolidone nanocomposites for flexible nonvolatile rewritable memory devices with reduced graphene oxide electrodes, Small. 8 (2012) 3517–3522. https://doi.org/10.1002/smll.201200999.

141. X. Hong, J. Liu, B. Zheng, X. Huang, X. Zhang, C. Tan, J. Chen, Z. Fan, and H. Zhang, A universal method for preparation of noble metal nanoparticle-decorated transition metal dichalcogenide nanobelts, Advanced Materials. 26 (2014) 6250-6254. https://doi.org/10.1002/adma.201402063.
142. M. Kang, Y.A. Kim, J.M. Yun, D. Khim, J. Kim, Y. Y. Noh, K. J. Baeg, and D. Y. Kim, Stable charge storing in two-dimensional MoS_2 nanoflake floating gates for multilevel organic flash memory, Nanoscale. 6 (2014) 12315-12323. https://doi.org/10.1039/C4NR03448A.
143. A. Krizhevsky, Learning Multiple Layers of Features from Tiny Images (University of Toronto, 2009).
144. J. Shi, J. Zhang, L. Yang, M. Qu, D. Chen, Q. Kelvin, and H. L. Zhang, Wide Bandgap Oxide Semiconductors: from Materials Physics to Optoelectronic Devices, Advanced Materials. 33 (2021) 2006230. https://doi.org/10.1002/adma.202006230.
145. J. Bian, Z. Li, S. Liang, Y. Tao, Z. Wang, Y. Zhu, C. Wang, H. Xu, and Y. Liu, 2D Tellurene-Based Optoelectronic Memristor with Temporal Dynamics for Multimodal Reservoir Computing System. Advanced Science (2025) e13647. https://doi.org/10.1002/advs.202513647.
146. A. Stoddart, Electronic devices: Making multi-terminal memtransistors, Nature Reviews Materials. 3 (2018) 18014. https://doi.org/10.1038/natrevmats.2018.14.
147. R.A. John, N. Tiwari, M.I.B. Patdillah, M. R. Kulkarni, N. Tiwari, J. Basu, S. K. Bose, Ankit, C. J. Yu, A. Nirmal, S. K. Vishwanath, C. Bartolozzi, A. Basu, and N. Mathews, Self-healable neuromorphic memtransistor elements for decentralized sensory signal processing in robotics, Nature Communications. 11 (2020) 4030. https://doi.org/10.1038/s41467-020-17870-6.
148. D. lelemini and S. Ambrogio, Emerging neuromorphic devices, Nanotechnology. 31 (2020) 092001. https://doi.org/10.1088/1361-6528/ab554b
149. L. Wang, W. Liao, S.L. Wong, Z. G. Yu, S. Li, Y. F. Lim, X. Feng, W. C. Tan, X. Huang, L. Chen, L. Liu, J. Chen, X. Gong, C. Zhu, X. Liu, Y. W. Zhang, D. Chi, K. W. Ang, Artificial synapses based on multiterminal memtransistors for neuromorphic application, Advanced Functional Materials. 29 (2019) 1901106. https://doi.org/10.1002/adfm.201901106.
150. Y. Kim, H. Kim, J. Jeon, S. Baik, and M. Kang, Circuit simulation of floating-gate FET (FGFET) for logic application, Memories - Materials, Devices, Circuits and Systems. 6 (2023) 100090. https://doi.org/10.1016/j.memori.2023.100090.
151. V.A. Trukhanov, A.Y. Sosorev, and D.I. Dominskiy, Dual Optoelectronic Organic Field-Effect Device: Combination of Electroluminescence and Photosensitivity. Molecules. 29 (2024) 2533. https://doi.org/10.3390/molecules29112533.
152. H. Jiao, X. Wang, and S. Wu, Ferroelectric field effect transistors for electronics and optoelectronics, Applied Physics Review. 10 (2023) 011310. https://doi.org/10.1063/5.0090120
153. R. Yang, A. Islama, and P. X. L. Feng, Electromechanical coupling and design considerations in single-layer MoS_2 suspended-channel transistors and resonators, Nanoscale. 7 (2015) 19921-19929. https://doi.org/10.1039/C5NR06118K.
154. S.H. Kim, S.G. Yi, M.U. Park, C. Jun, L. M. Kim, and K. H. Yoo, Multilevel MoS_2 optical memory with photoresponsive top floating gates, ACS Applied Materials & Interfaces. 11 (2019) 25306–25312. https://doi.org/10.1021/acsami.9b05491.
155. T. Y. Wang, J. L. Meng, Q. X. Li, Z. Y. He, H. Zhu, L. Ji, Q. Q. Sun, L. Chen, and D. W. Zhang, Reconfigurable optoelectronic memristor for in-sensor computing applications, Nano Energy. 89 (2021) 106291. https://doi.org/10.1016/j.nanoen.2021.106291.
156. F. Gong, W. Luo, J. Wang, P. Wang, H. Fang, D. Zheng, N. Guo, J. Wang, M. Luo, J. C. Ho, X. Chen, W. Lu, L. Liao, W. Hu, High-sensitivity floating-gate phototransistors based on WS_2 and MoS_2. Advanced Functional Materials. 26 (2016) 6084–6090. https://doi.org/10.1002/adfm.201601346.
157. L. Mennel, J. Symonowicz, S. Wachter, D. K. Polyushkin, A. J. Molina-Mendoza, and T. Mueller, Ultrafast machine vision with 2D material neural network image sensors, Nature. 579 (2020) 62. https://doi.org/10.1038/s41586-020-2038-x
158. L. Ju, J. Velasco Jr, E. Huang, S. Kahn, C. Nosiglia, H. Z. Tsai, W. Yang, T. Taniguchi, K. Watanabe, Y. Zhang, G. Zhang, M. Crommie, A. Zettl, and F. Wang, Photoinduced doping in heterostructures of graphene and boron nitride. Nature Nanotechnology. 9 (2014) 348–352. https://doi.org/10.1038/nnano.2014.60.
159. Y. C. Lee, J. L. Shen, K. W. Chen, W. Z. Lee, S. Y. Hu, K. K. Tiong, and Y. S. Huang, Observation of persistent photoconductivity in 2H-$MoSe_2$ layered semiconductors. Journal of Applied Physics. 99 (2006) 063706. https://doi.org/10.1063/1.2180398.
160. K. Kang, S. Xie, L. Huang, Y. Han, P. Y. Huang, K. F. Mak, C. J. Kim, D. Muller, and J. Park, High-mobility three-atom-thick semiconducting films with wafer-scale homogeneity. Nature. 520 (2015) 656–660. https://doi.org/10.1038/nature14417.

161. M. M. Islam, A. Krishnaprasad, D. Dev, R.M. Martinez, V. Okonkwo, B. Wu, S.S.Han, T. S. Bae, H. S. Chung, J. Touma, Y. Jung, and T. Roy, Multiwavelength Optoelectronic Synapse with 2D Materials for Mixed-Color Pattern Recognition, ACS Nano. 16 (2022) 10188-10198. https://doi.org/10.1021/acsnano.2c01035.
162. Y. Lee. S. Bae, H. Jang, S. Jang, S. E. Zhu, S. H. Sim, Y. I. Song, B. H. Hong, and J. H. Ahn, Wafer-scale synthesis and transfer of graphene films. Nano Letters. 10 (2010) 490-493. https://doi.org/10.1021/nl903272n.
163. J. Shim, S.H. Bae, W. Kong, D. Lee, K. Qiao, D. Nezich, Y. J. Park, R. Zhao, S. Sundaram, X. Li, H. Yeon, C. Choi H. Kum R. Yue, G. Zhou, Y. Ou, K. Lee, J. Moodera, X. Zhao, J. H. Ahn, C. Hinkle, A. Ougazzaden, and J. Kim, Controlled crack propagation for atomic precision handling of wafer-scale two-dimensional materials. Science. 362 (2018) 665–670. https://doi.org/10.1126/science.aat8126.
164. J. Li, X. Yang, Y. Liu, B. Huang, R. Wu, Z. Zhang, B. Zhao, H. Ma, W. Dang, Z. Wei, K. Wang, Z. Lin, X. Yan, M. Sun, B. Li, X. Pan, J. Luo, G. Zhang, Y. Liu, Y. Huang, X. Duan, X. Duan, General synthesis of two-dimensional van der Waals heterostructure arrays, Nature. 579 (2020) 368–374. https://doi.org/10.1038/s41586-020-2098-y.
165. R. Wu, Q. Tao, W. Dang, Y. Liu, B. Li, J. Li, B. Zhao, Z. Zhang, H. Ma, G. Sun, X. Duan, and X Duan, Van der Waals epitaxial growth of atomically thin 2D metals on dangling-bond-free WSe_2 and WS_2. Advanced Functional Materials. 29 (2019) 1806611. https://doi.org/10.1002/adfm.201806611.
166. R. Malladi and J. A. Sethian, A unified approach to noise removal, image enhancement, and shape recovery, IEEE Transactions on Image Processing. 5 (1996) 1554-1568. https://doi.org/10.1109/83.541425.
167. N. Aslam, M.K. Ehsan, Z.U. Rehman, M. Hanif, G. Mustafa, A modified form of different applied median filter for removal of salt & pepper noise, Multimedia Tools and Applications. 82 (2022) 7479-7490. https://doi.org/10.1007/s11042-022-13289-x.
168. A.M. Wink, and J.B. Roerdink, Denoising functional MR images: a comparison of wavelet denoising and Gaussian smoothing, IEEE Transactions on Medical Imaging 23 (2004) 374-387. https://doi.org/10.1109/TMI.2004.824234.
169. C. Tian, L. Fei, W. Zheng, Y. Xu, W. Zuo, and C. W. Lin, Deep learning on image denoising: an overview, Neural Network. 131 (2020) 251–275. https://doi.org/10.1016/j.neunet.2020.07.025.
170. S. Ma, T. Wu, X. Chen, Yin Wang, J. Ma, H. Chen, A. Riaud, J. Wan, Z. Xu, L. Chen, J. Ren, D. W. Zhang, P. Zhou, Y. Chai, and W. Bao, A 619-pixel machine vision enhancement chip based on two-dimensional semiconductors, Science Advances. 8 (2022) eabn9328. https://doi.org/10.1126/sciadv.abn9328.
171. C. Jin, W. Liu, Y. Xu, Y. Huang, Y. Nie, X. Shi, G. Zhang, P. He, J. Zhang, H. Cao, J. Sun, J. Yang, Artificial Vision Adaption Mimicked by an Optoelectrical In_2O_3 Transistor Array, Nano Letters. 22 (2022) 3372-3379. https://doi.org/10.1021/acs.nanolett.2c00599
172. Y. Liu, D. Cai, T. Zhao, M. Shen, X. Liu, and D. Gu, Heterogeneous ion-modulated 2D-WS_2 heterosynaptic memtransistor for controllable synaptic modulation and energy-efficient neuromorphic computing, Chemical Engineering Journal. 492, (2024) 152215. https://doi.org/10.1016/j.cej.2024.152215
173. W. Deng, Y. Yu, X. Yan, L. Wang, N. Yu, X. Liao, W. Luo, and J. Wu, Linearly Programmable Oxygen-Doped MoS_2 Memtransistor for Neuromorphic Computing. ACS Nano. 19 (2025) 27526–27537. https://doi.org/10.1021/acsnano.5c06688.